HAL open science

Cosmic rays and pulsars: connections from low to ultrahigh energies

Kumiko Kotera

▶ To cite this version:

Kumiko Kotera. Cosmic rays and pulsars: connections from low to ultrahigh energies. High Energy Astrophysical Phenomena [astro-ph.HE]. UPMC - Paris 6 Sorbonne Universités, 2014. tel-01968764

HAL Id: tel-01968764

https://theses.hal.science/tel-01968764v1

Submitted on 17 Jan 2019

HAL is a multi-disciplinary open access archive for the deposit and dissemination of scientific research documents, whether they are published or not. The documents may come from teaching and research institutions in France or abroad, or from public or private research centers.

L'archive ouverte pluridisciplinaire **HAL**, est destinée au dépôt et à la diffusion de documents scientifiques de niveau recherche, publiés ou non, émanant des établissements d'enseignement et de recherche français ou étrangers, des laboratoires publics ou privés.

Cosmic rays and pulsars:

connections from low to ultrahigh energies

Kumiko Kotera — Institut d'Astrophysique de Paris, UMR 7095 - CNRS, Université Pierre & Marie Curie, 98 bis boulevard Arago, 75014, Paris, France ; email: kotera@iap.fr

Since their discovery more than a hundred years ago, cosmic rays have provided a well of excitement and enigma for particle physicists and astrophysicists, with their colossal energies, and their mysterious extra-solar origins. A connection between cosmic rays and pulsars was suggested in the decades following the discovery of the first pulsar, but was never deeply investigated, in particular at the highest energies. The recent multi-messenger data related to cosmic-rays and the boom in pulsar observations make it timely to dig into this matter now. We explore in this thesis the links between cosmic rays and pulsars from low to ultrahigh energies. At low energies, below the knee, we show how pulsars could help solve some of the main current observational puzzles. At energies above the knee, we discuss the potential of pulsar populations to accelerate particles and to reproduce the measured cosmic-ray data. More specifically, we find that the production of ultrahigh energy cosmic rays in these objects could give a picture that is surprisingly consistent with the latest data from the Auger Observatory. We discuss the signatures associated to such a source model in terms of other messengers (neutrinos and photons at different wavelengths). Using some of these signatures, we elaborate on how cosmic rays and their interactions with the surrounding medium can be used as tools to diagnose the nature of pulsars and their winds.

Mémoire d'habilitation à diriger des recherches
Présentée à l'Université Pierre & Marie Curie
Soutenue le 5 novembre 2014
Devant le jury composé de

Catherine Césarsky	Présidente
Elena Amato	Rapportrice
Guillaume Dubus	Rapporteur
Eric Gourgoulhon	Rapporteur
Frédéric Daigne	Examinateur
Ralph Engel	Examinateur

Acknowledgements

All the amazing things that have happened in my career until now, I owe them to Martin Lemoine and Angela Olinto, and I will never thank them enough. Many thanks also to Joe Silk for trusting my competence, and for getting me into lower-energy cosmic rays and exotic ideas. Many thanks as well to Sterl Phinney for enhancing my interest in pulsars.

I was lucky to be accompanied by wonderful people through these years; I would like to thank all my collaborators, and in particular Kohta Murase, Vasiliki Pavlidou and Tanguy Pierog.

Special thanks to Ke Fang and Foteini Oikonomou, whom I had the immense pleasure to co-advise, for their brilliant work, their delightful company and their confidence.

I am extremely grateful to Elena Amato, Catherine Césarsky, Frédéric Daigne, Guillaume Dubus, Ralph Engel and Eric Gourgoulhon who have accepted to be part of this Habilitation Committee. It is a real honor for me, as each of them has been a source of inspiration, and I appreciate their constant trust and support.

I would like to thank Laurent Vigroux for his warm support and guidance as Director of the Institut d'Astrophysique de Paris over the last eight years, and the staff of my home institute for being so incredibly helpful. My deepest thanks to the University of Chicago and KICP for their regular support and hospitality. I am also very grateful to Ofer Lahav and the University College London for supporting and hosting me.

The work presented here was made possible thanks to the financial support from the Programme National des Hautes Energies, the Institut Lagrange de Paris, Sorbonne Universités and the CNRS.

Finally, I would like to thank all my friends and colleagues in institutes worldwide. A million thanks to all those I have shared coffees/lunches/dinners/evenings with, chatting about life and research, the difficulties and thrill of being in translation, two-body problems and impostor syndromes, the intimate pain and grace of working in this field.

To my most important ones: my family.
To my most important one: Aurélien.

Chicago, July 24, 2014

About this work

This Habilitation thesis summarizes the bulk of my research in the last six years, connected to pulsars and cosmic rays. It was done in collaboration with various researchers worldwide, in particular, with senior collaborators at the Institut d'Astrophysique de Paris (Martin Lemoine and Joseph Silk), at the University of Chicago (Angela Olinto) and at the California Institute of Technology (Sterl Phinney). Other collaborators include Kohta Murase (Institute for Advanced Studies), Timur Delahaye (University of Stockholm), Angeles Perez-Garcia (University of Salamanca) and Jérôme Pétri (Observatoire de Strasbourg).

A large fraction of Chapters 3, 4 and 5 are part of the Ph.D. thesis of Ke Fang, whom I have been supervising at 80% level since 2010. Ke's official advisor is Angela Olinto and she is expected to graduate in the Fall of 2015.

The work done with Foteini Oikonomou, the other Ph.D. student whom I advised at 80% level in 2012-2014 at the University College London (official advisor: Ofer Lahav), is sketched in Chapter 4. It concerns ultrahigh energy cosmic ray arrival direction anisotropies and gamma-ray signatures from blazars, and are thus not directly related to the subject of this Habilitation thesis. Foteini graduated in April 2014 and is now a postdoctoral scholar at Penn State University.

Note that most of my on-going preliminary work is not presented here. My previous research on cosmic-ray propagation, magnetic fields and secondary messengers, done principally during my Ph.D. and first years of postdoc, are only briefly mentioned in Chapters 3 and 5.

This work was supported by the Institut d'Astrophysique de Paris and the CNRS, the KICP and the University of Chicago, the California Institute of Technology and the Fairchild Fellowship, the University College London, the Programme National des Hautes Energies, the Institut Lagrange de Paris and Sorbonne Universités.

Contents

1. Introduction and History 7

2. Pulsars as cosmic-ray producers below the knee 13
- 2.1. What could we learn from a sharply falling positron fraction? 14
  - 2.1.1. Method 15
  - 2.1.2. Results 16
  - 2.1.3. Discussion 18
- 2.2. Strangelets and the TeV-PeV cosmic-ray anisotropies 20
  - 2.2.1. Strangelet properties and sources 21
  - 2.2.2. Interaction with molecular clouds and Hotspots characteristics 21
  - 2.2.3. Comparison with data and signatures 23

3. Pulsars and ultrahigh energy cosmic rays 25
- 3.1. A quest for sources of ultrahigh energy cosmic rays 25
  - 3.1.1. Clues from the energy spectrum 25
  - 3.1.2. Clues from the chemical composition 26
  - 3.1.3. Clues from the arrival directions in the sky 27
  - 3.1.4. A promising candidate source: newly-born pulsars 28
- 3.2. Injection and acceleration of high energy cosmic rays in pulsar winds 29
  - 3.2.1. Heavy nuclei injection 29
  - 3.2.2. Maximum acceleration energy 30
  - 3.2.3. Injected spectrum 32
- 3.3. UHECR escape from supernova envelopes 32
  - 3.3.1. Supernova envelopes 32
  - 3.3.2. Escaped fluxes 33
- 3.4. Comparison to the observed data 34
  - 3.4.1. Distribution of parameters in the extragalactic pulsar population 34
  - 3.4.2. Propagation in the intergalactic medium 35
  - 3.4.3. Overall spectrum and composition 35
  - 3.4.4. Required source density 36
  - 3.4.5. Distribution of events in the sky 37
- 3.5. Conclusions 38

4. Galactic pulsars and the ankle region 39
- 4.1. Propagation from Galactic sources 40
- 4.2. Very High Energy cosmic-ray flux from pulsars 41

5. Multi-messenger signatures of the pulsar scenario 45
- 5.1. Cosmogenic messengers 46
  - 5.1.1. Diffuse cosmogenic neutrinos fluxes 46
  - 5.1.2. Diffuse cosmogenic fluxes for the pulsar scenario 47
  - 5.1.3. Cosmogenic fluxes from single sources 48
- 5.2. Diffuse neutrino fluxes associated with the pulsar scenario 49
  - 5.2.1. Neutrinos from a single pulsar 49

5.2.2. Diffuse neutrino intensity . . . 50
5.2.3. Neutrinos produced during acceleration in the PWN . . . 52
5.3. Gravitational-wave signatures for magnetars . . . 54

6. Diagnosing pulsar winds with cosmic-ray signatures 57
6.1. Signatures of pulsars in the light curves of early supernova ejecta . . . 57
6.1.1. Bolometric radiation . . . 58
6.1.2. Thermal/non-thermal emissions . . . 58
6.1.3. Thermalization in the ejecta . . . 60
6.1.4. Discussion, conclusion . . . 61
6.2. Effects of millisecond pulsar winds on binary companions . . . 63
6.2.1. Irradiation of companions: analytical estimates . . . 64
6.2.2. Shower development in companion atmospheres . . . 65
6.2.3. Effects on white dwarf atmospheres . . . 67
6.2.4. Comparisons with observations . . . 67

7. Perspectives 71

A. Characteristics of millisecond pulsar wind nebulae 73
A.1. Pulsar wind energetics and timescales . . . 73
A.2. Pulsar wind nebula radius and magnetic field . . . 74
A.3. Energy distribution in the pulsar wind nebula . . . 76
A.4. Electron synchrotron SED of the pulsar wind nebula . . . 76

B. The unipolar induction toy model 79
B.1. Voltage drop across pulsar magnetospheres . . . 79
B.2. Maximum acceleration energy . . . 79
B.3. Injected flux . . . 79

C. Early supernova ejecta lightcurves 81
C.1. Bolometric luminosity lightcurve . . . 82
C.2. Photo-disintegration in supernova ejectas . . . 82

D. Radiative transfer basics in stellar atmospheres 85
D.1. Atmospheric column densities . . . 85
D.2. Rosseland Approximation . . . 85
D.3. The photosphere . . . 85

1. Introduction and History

Cosmic rays are high energy particles, mostly charged atomic nuclei, that constantly bombard the Earth. Since their discovery more than a hundred years ago, they have provided a well of excitement and enigma for particle physicists and astrophysicists, with their colossal energies, and their mysterious extra-solar origins. The former physicists considered cosmic rays as a means to probe hadronic interactions, and the latter, as a new messenger to understand the Universe.[1]

The cosmic-ray spectrum measured on Earth (Fig. 1.1) traces a surprisingly regular declining power law over more than 10 orders of magnitude in energy ($\sim 10^{10} - 10^{21}$ eV) and 30 orders in flux. We will focus in this thesis on particles within this energy range —these originate outside our solar system. With a closer look, one notices the presence of breaks in the power law (in particular the so-called *knee* at 10^{15} eV and the *ankle* at 10^{18} eV) that reveal the various energy regimes and likely the different sources of these particles. Each of these regimes raise important astrophysical questions that are still unanswered. In particular, at the highest energies, the sheer question of the origin of these particles remains a mystery. The recent measurement of a flux suppression at the highest energies (Abraham et al. 2010), reminiscent of the "GZK cut-off" (Greisen 1966; Zatsepin & Kuzmin 1966) produced by the interaction of particles with the cosmic microwave background photons for propagations over intergalactic scales, has appeased the debate concerning the extragalactic provenance of ultrahigh energy cosmic rays. But the exact source is still to be found, and how these particles can be accelerated to such energies is another enigma.

The major difficulties in answering these questions reside in the very nature, energy, and flux of cosmic rays. Most of these particles are charged, and thus deflected by cosmic magnetic fields at all scales – mainly Galactic and extragalactic fields – depending on their energies. Tracing back their trajectories to their sources is a challenge, given our poor knowledge of these magnetic fields. Above $\sim 10^{15}$ eV, particles cannot be detected directly, as the atmosphere acts like a calorimeter: primary cosmic rays interact with the molecules of the air, and induce showers of secondary particles. To reconstruct the characteristics of the primary particles by measuring these air-showers, one has to rely on hadronic interaction models, extrapolated at energies too high to be tested experimentally. Some of the particles are indeed detected with energies 40 million times larger than that reached with the Large Hadronic Collider[2]. Note that this constitutes a unique research ground for particle physicists. Finally, at the extreme high-energy end of the spectrum, the flux of particles is very low and one runs into a statistical limitation.

Cosmic rays are also at the origin of most of the high-energy neutrinos and of the non-thermal radiation, in particular of gamma rays. Hence one natural strategy is to conduct multi-messengers studies that cross-correlate cosmic-ray, neutrino, and gamma-ray information, to ultimately understand the mechanisms at play in the most powerful sources of our Universe. With the first detection of cosmic neutrinos with the IceCube experiment in 2012 and the consequent birth of high-energy neutrino astronomy, we stand today at the threshold of an exciting multi-messenger era. The ongoing theoretical endeavor and the numerous instruments planned and in operation ensure that important progress will be made in astroparticle physics in the next decades.

The possible candidate sources for high-energy cosmic rays are the most powerful astrophysical objects. They range from the tiniest compact stars like pulsars to explosions related to supernovae and long-duration gamma-ray bursts, to accretion shocks in the intergalactic medium, or to events in active galactic nuclei. The maximum accessible energy in these objects depends on their ability i) to accelerate particles and ii) to let them escape from the acceleration site without important energy losses. The success of a cosmic-ray source scenario further lies in its capacity to reproduce the observations, namely the shape and normalization of the energy spectrum, the composition, and the distribution of arrival directions of particles in the sky.

[1] For a general overview and a list of references for high-energy cosmic-ray astrophysics and its history, see Kotera & Olinto (2014).

[2] 14 TeV is the maximum energy reached by particles in the LHC, in the central momentum frame. In the proton rest frame though, energies of order 10^{17} eV can be probed.

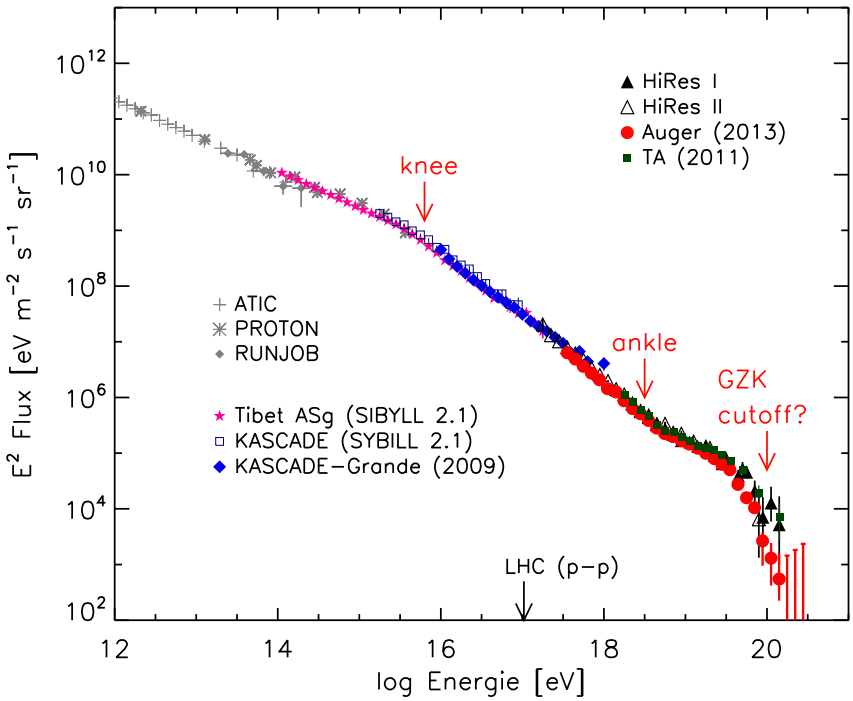

Figure 1.1.: *All particle cosmic ray flux multiplied by E^2 observed by ATIC (Ahn et al. 2008), PROTON (Grigorov et al. 1971), RUNJOB (Apanasenko et al. 2001), Tibet AS-γ (Chen 2008), KASCADE (Kampert et al. 2004), KASCADE-Grande (Apel et al. 2009), HiRes-I (Abbasi et al. 2009), HiRes-II (Abbasi et al. 2008), and Auger (The Pierre Auger Collaboration et al. 2013). LHC energy reach of $p-p$ collisions (in the frame of a proton) is indicated for comparison. Data collected by R. Engel. Adapted from Kotera & Olinto (2011).*

The high-energy astrophysics community is massively focussed on working out the connections between cosmic rays and supernovae for particle energies up to $\sim 10^{15-17}$ eV, and with gamma-ray bursts or active galactic nuclei at ultrahigh energies. Yet pulsars constitute an equally promising – and complex – candidate.

Pulsars are highly magnetized neutron stars rotating rapidly, that result from the collapse of the core of massive stars and its associated supernova explosion. Thousands of them are known today and have been observed at various wavelengths, notably in radio, X-rays and gamma-rays. The neutron stars themselves are considered as precious laboratories to explore extreme-state physics. The surrounding environment of pulsars is also the subject of intense studies. Pulsars lose their energy via electromagnetic cooling principally, under the form of an outflow (the *wind*). The wind is believed to be composed of some mixture of relativistic particles and Poynting flux. There are however ongoing debates about the energy, the nature, the structure, formation and evolution of this outflow.

In the most standard models, the acceleration of leptonic e^+e^- pairs in electric fields generated nearby the star is responsible for the primary radiation of pulsars. Below the *knee* energy, much effort has thus been put into connecting pulsars with the detected leptonic cosmic rays. Hadronic cosmic rays could also be accelerated via the same mechanisms and/or further in the wind. In principle, for fast-rotating pulsars that have a huge rotational energy reservoir, acceleration could even happen up to very high energies. The large uncertainties on the possible acceleration mechanisms in pulsar environments and our poor knowledge of pulsar winds have long discouraged studies of hadronic cosmic-ray production in pulsars. In practice, such studies are scarce in the literature, and one objective of this thesis is to try to make up for this knowledge gap. We aim at building a comprehensive scenario for the production of high and ultrahigh energy cosmic rays in pulsar winds, taking into account detailed acceleration mechanisms, particle escape from surrounding regions, and global source population studies. Observable predictions will also be made for multi-messenger instruments.

With the numerous X-ray and gamma-ray pulsar

observations collected with the latest detectors, we could acquire a better insight of the workings of pulsars, their winds, and their interactions with the surrounding environment. In particular, one novel approach proposed in this thesis is to apply our study on the interaction of cosmic rays carried by the wind on the ambient medium, and compare the results with the well of information provided by observations of supernovae and binary systems. The point is to reverse-engineer the properties of the wind, instead of building up from first principles of a complete theoretical picture for wind composition.

We explore in this thesis the connections between cosmic rays and pulsars from low to ultrahigh energies. At low energies, below the knee (10^{12-15} eV), we show how pulsars could help solve some of the main current observational puzzles. At energies above the knee, we discuss the potential of pulsar populations to accelerate particles and to reproduce the measured cosmic-ray data. More specifically, we find that the production of ultrahigh energy cosmic rays in these objects could give a picture that is surprisingly consistent with the latest data from the Auger Observatory. We discuss the signatures associated to such a source model in terms of other messengers. Using some of these signatures, we elaborate on how cosmic rays and their interactions with the surrounding medium can be used as tools to diagnose the nature of pulsars and their winds.

History: cosmic rays and pulsars over time

The astrophysics of cosmic rays and of pulsars have followed different story lines. The former was built on unexpected experimental measurements at the beginning of the 20th century, revealing the existence of these high energy particles, and various theoretical works have been put forward to try to explain these observations. On the other hand, the idea of neutron stars was first sketched in 1932 but remained for a long time a theoretical fantasy, before being detected serendipitously in 1967. By that time, cosmic rays had been detected from low to ultrahigh energies, but theorists were struggling to understand their origins. Pulsar astrophysics thus started in practice half a century later, but has progressed more quickly, as increasingly powerful instruments were built and numerous data was taken on these objects, in various wavelengths. The link between cosmic rays and pulsars was established soon after the discovery of the latter, and pulsars have long been suggested as candidate sources for cosmic rays at energies below the knee. At ultrahigh energies however, only few studies can be found on this connection.

The discovery of cosmic rays dates back to the early 1900s, when physicists were trying to understand why their electrometers, designed to measure radioactivity, would spontaneously discharge. In order to assess whether this ionizing radiation was coming from the ground or the sky, Victor Hess carried electrometers in balloons, and conducted in 1912 what one might call the first physics experiments in space. His conclusion was clear: the radiation increased with height, and was thus coming from outer space. The name *cosmic rays* was coined by Robert Millikan, who believed until his death, despite strong scientific evidence to the contrary, that these particles were photons, and not matter. The debate on the nature of this ionizing flux lasted a couple of decades, culminating notably in 1932 with a fight between Arthur Compton and Millikan that made the front page of *The New York Times* on December 31st. Various measurements in the 1930s showing the anisotropic flux of cosmic rays deflected by the Earth magnetic field convinced the community that these particles are in the majority positively charged. In 1939, building on a note of Bruno Rossi that Geiger counters placed at a distance of a few meters would receive cosmic-ray signals simultaneously, Pierre Auger placed instruments on distant mountain peaks, and measured coincident signals that proved the existence of atmospheric air-showers. The detected particles were indeed the secondaries of a primary cosmic ray interacting with the molecules of the atmosphere.

Meanwhile, in 1932, two years only after the discovery of neutrons by cosmic-ray physicists, Baade and Zwicky came up with the idea that neutron stars, composed almost essentially of neutrons, could be born at the core of supernovae, which are explosions of massive stars at the end of their lives. Interestingly, immediately after, the same authors proposed that these supernovae could accelerate cosmic rays. A few years later, in 1939, Oppenheimer and Volkoff sketched the first models of neutron star structures (Oppenheimer & Volkoff 1939). The astronomical community showed little enthusiasm in searching for these objects (it was then technically impossible...), and it is only 25 years later that neutron stars were discovered by chance.

Between 1920 and 1950, cosmic rays were principally a tool for particle physics. Their interactions in instruments such as the Wilson cloud chamber enabled the discovery of many elementary particles (positron, muon, kaon, pion), leading to a series of Nobel Prizes. In 1953, the famous conference of Bagnère de Bigorre in the French Pyrénées (Cronin 2011) gathered an impressive number of eminent particle physicists. The conference laid the main foundations of subatomic physics and marked an important transition in the field: the study of particles via cosmic rays was abandoned progressively, as large accelerators were being built worldwide.

Around the same time, astrophysicists finally started to show interest in cosmic rays as messengers from the Universe. More generally, the field of high-energy astrophysics started to bloom. In the 1950s, radio telescopes revealed that the prominent source of radio emission was synchrotron radiation, implying that our Galaxy was filled with relativistic electrons. The distribution of electrons started to be mapped, and their transport in the Galactic magnetic field was studied. Electrons constitute however only a tiny fraction of cosmic rays. In 1948, balloons were sent to measure the composition of these particles, and it was found that all elements ranging from protons to iron are present in the cosmic radiation in the high atmosphere.

The sources and the acceleration mechanisms of particles of 10^{15} eV intrigued astronomers. As mentioned above, supernovae were proposed early back in 1934. In 1949, Fermi laid the ground for the modern cosmic-ray acceleration theory, modeling cosmic rays as a gas of charged relativistic particles in motion in the interstellar medium. The acceleration processes he proposed are called today Fermi processes.

In 1967, Jocelyn Bell and Anthony Hewish were examining the scintillation of radio signals in order to detect quasars. They detected periodical packs of radio waves from a particular point of the sky. The signal was confirmed the next days and they upgraded their instrument in order to be able to resolve the signal temporally. It was then revealed that the signal presented a pulsation of about 1.337 s. They named the source of this pulsed signal *pulsar* and it has since been labeled B1919+21.

The link between pulsars and neutron stars was established soon after this discovery. Pacini postulated that the energy reservoir of the Crab nebula was a strongly magnetized and rapidly rotating neutron star. Independently, Gold had introduced the concept of rotationally-powered pulsars, modeling neutron stars as rotating magnetic dipoles, losing energy by electromagnetic radiation and emission of relativistic particles, which led to their spin-down (Gold 1968). The neutron-star theory to explain pulsars (as opposed to the white dwarf scenario that was also debated, Meltzer & Thorne 1966), was definitely confirmed by the observation in 1968 of a 89-ms period pulsar in the Vela supernova remnant (Large et al. 1968) and of a 33-ms pulsar in the Crab nebula (Staelin & Reifenstein 1968). Immediately after their discovery, pulsars were suggested as possible accelerators of cosmic-rays (Gunn & Ostriker 1969), due to these important rotational and magnetic energy reservoirs.

A year after the discovery of B1919+21, astronomers started an extensive search for pulsar signals in other wavelengths. Cocke et al. (1969) reported a discovery of optical pulsations from the Crab pulsar, and Fritz et al. (1969) and Bradt et al. (1969) announced its detection in X-rays, using a rocket placed in the upper atmosphere. Gamma-ray astronomy started in 1972 with the Small Astronomy Satellite (SAS-2) which observed three point-like sources along the Galactic plane. Two of them were identified via their spatial coincidence and their pulsation as the Crab and Vela radio pulsars (Kniffen et al. 1974; Thompson 1975). The third source, Geminga, was only identified as a pulsar in 1992, via the measurement of its 237-ms pulsation in X-rays (Halpern & Holt 1992) and in gamma-rays (Bignami et al. 1992).

Gamma-ray observatories were built massively starting from the 70s, and mostly from the 90s, to collect more point-like sources in the Galactic plane, but also to study the diffuse Galactic gamma-ray flux, which was believed to be related to cosmic rays. In order to identify the sources of these particles, gamma rays, that are produced by interactions of the former with the radiative and baryonic ambient backgrounds, happen to be a key-messenger, as they are not charged and point back to their origin. The atmosphere screening out these photons in the energy range of interest (10^{8-10} eV), satellites such as PROTON, OSO-3, SAS-2, Cos B, Compton were sent out in space to measure their fluxes. Today, the Fermi satellite has taken up the measurements and has detected about 150 gamma-ray pulsars. At higher energies, ground-based observatories like HESS, MAGIC, VERITAS and HAWC are measuring the air showers induced by gamma rays penetrating the atmosphere. For a few specific

objects, the pulsar immediate environments, in particular their nebula, are being mapped in X-rays and gamma-rays in increasing detail. This has introduced many unexpected puzzles, but is also opening the possibility of a thorough investigation of the emission mechanisms.

Recently, gamma-ray observations of supernova remnants W44 and IC443 by the AGILE and Fermi telescopes (Tavani et al. 2010; Giuliani et al. 2011; Ackermann et al. 2013) have confirmed that relativistic protons are present in these two supernovae. These observations are in line with the standard theory that supposes that cosmic rays at $\sim 10^{15}$ eV originate in supernovae in our Galaxy. Meanwhile, Galactic cosmic rays, and leptons in particular, have also been directly collected by several experiments such as PAMELA, CREAM, AMS-02, and theoretically unexpected measurements have been reported, adding new enigmas to the picture. In this energy range (below the knee), most astrophysical explanations to the leptonic cosmic-ray component involve pulsar contributions.

Since the 1960s (before the discovery of pulsars), cosmic rays of higher energies have also been detected, pushing the mystery to extreme frontiers. While measuring cosmic rays with a grid of detectors in New Mexico, John Linsley and his collaborators detected the so-called *ultrahigh energy cosmic rays* (UHECRs), with energy exceeding 10^{20} eV. The flux of cosmic rays at this energy is of order 1 particle per square kilometer per century, and their origin and acceleration mechanism was even more enigmatic. It was only during the 1990s that an international effort began to address these questions with the necessary large-scale observatories. The largest detectors operating during the 1990s were the Akeno Giant Air Shower Array (AGASA), a 100 km^2 ground array of scintillators in Japan, and the High Resolution Fly's Eye (HiRes) a pair of fluorescence telescopes that operated in Utah until 2006. At slightly lower, but equally mysterious energies (around 10^{15-18} eV), the KASCADE and KASCADE-Grande have performed detailed measurements of the flux and composition of charged nuclei.

Completed in 2008, the Pierre Auger Observatory is the largest observatory at present. Constructed in the province of Mendoza, Argentina, by a collaboration of 18 countries, it consists of a 3,000 km^2 array of water Cherenkov stations with 1.5 km spacing in a triangular grid overlooked by four fluorescence telescopes. The combination of the two techniques into a hybrid observatory maximizes the precision in the reconstruction of air showers, allowing for large statistics with good control of systematics. The largest observatory in the northern hemisphere, the Telescope Array (TA), is also hybrid. Situated in Utah, it covers 762 km^2 and is overlooked by three fluorescence telescopes.

The connection between high energy cosmic rays (around the knee region up to the ankle) and Galactic pulsars was suggested by a few authors in the decades following the discovery of the first pulsar (Karakula et al. 1974; Bednarek & Protheroe 1997, 2002; Giller & Lipski 2002; Bednarek & Bartosik 2004). Blasi et al. (2000) proposed that iron nuclei accelerated in the fastest spinning young neutron stars could explain the observed cosmic rays above the ankle in a Galactic source scenario, building up on previous constraints by Venkatesan et al. (1997). They assumed that the stripping of heavy nuclei from the surface of the star is a plausible seeding and derived a spectrum based on the spin down of young pulsars. Arons (2003) studied the birth of extragalactic magnetars (highly magnetized neutron stars) as the source of ultrahigh energy protons, developing the acceleration mechanism in detail and assuming that the magnetar wind disrupts the supernova envelope to allow the escape of accelerated particles.

Most of the works conducted on this subject were made before the construction of the Auger Observatory. The Blasi et al. (2000) and Arons (2003) proposals for the origin of UHECRs were elaborated to explain the absence of the GZK cutoff in the observed spectrum reported by AGASA (Takeda et al. 1998) without invoking the so-called top-down models (see, e.g., Bhattacharjee 2000). An increase in the exposure at the ultrahigh energies by the HiRes and Auger Observatories have shown that the UHECR spectrum is consistent with a GZK cutoff (Abbasi et al. 2008; Abraham et al. 2010b). Over the years, the pulsar model seemed to have been abandoned, likely because of one main feature: the unipolar induction process invoked by all these authors to accelerate particles in pulsars generates a hard spectrum that does not fit the observed UHECR spectrum. A detailed study of particle escape from the dense and radiative supernova ejecta surrounding the pulsar was also needed. The works cited above are essentially toy-models, that do not address detailed acceleration and escape issues. A decade ago, the chemical composition was also barely detectable at the highest energies while recent results suggest a puzzling trend toward heavier nuclei.

Today, we stand at the threshold of a multimessen-

ger era, where cosmic rays, as progenitors of gamma rays and neutrinos, play a central role. The construction of gamma-ray telescopes such as MAGIC, VERITAS, HESS and HAWC on the ground, as well as the launch of the AGILE and Fermi satellites have enabled us to explore a vast panel of astrophysical objects over a new range of wavelengths. The breach opened by gamma-ray astronomy has led to exponential progress in other fields of high energy astrophysics. The cosmic-ray experiments mentioned above are collecting particles over more than ten orders of magnitude in energies, up to 10^{20} eV, from the most powerful (unidentified) astrophysical objects. The IceCube experiment is finally detecting astrophysical neutrinos, which will place stringent constraints on the physical properties of their sources. These experiments are now reaching the sensitivities required to measure the secondary particles produced via the interactions of cosmic rays, and could help distinguish the pulsar scenario among others.

A new investigation of the connection between cosmic rays and pulsars is timely, in the light of the data that has been recently acquired, and given the potential detections that lie ahead.

2. Pulsars as cosmic-ray producers below the knee

One striking feature in the cosmic-ray spectrum appears as a steepening of the power law around PeV ($= 10^{15}$ eV) energies. This break is commonly referred to as the *knee*. There is a wide consensus that the knee is the signature of the maximum acceleration energy of protons in Galactic sources. Galactic accelerators are likely responsible for the dominant component of cosmic rays observed on Earth, given the containment of lower energy cosmic rays by the Galactic magnetic field (e.g., Cesarsky 1980; Hillas 1984; Strong et al. 2007). The recent increase of gamma-ray observations have opened the possibility that the origin of these Galactic cosmic rays will be soon identified (Tavani et al. 2010; Giuliani et al. 2011; Ackermann et al. 2013). Gamma-ray observations from GeVs ($= 10^9$ eV) to 100s of TeV ($= 10^{12}$ eV) show at least several populations of gamma-ray generating astrophysical accelerators in the Universe. The main challenge now is to identify the hadronic accelerators among this list of sources where the leading candidate continues to be shock acceleration in supernova remnants (see, e.g., Hillas 2005; Blasi 2011, 2013 for reviews on this so-called "supernova remnant paradigm"). Supernova remnants were already suggested as potential sources by Ginzburg & Syrovatskii (1964). Supernovae are stellar explosions that eject matter and radiation into the interstellar medium. The interface between the ejected material and the interstellar medium creates a shock region. A modest efficiency of $\sim 10\%$ in converting the kinetic energy of supernova shocks into particle acceleration and the frequency of supernova remnants in our Galaxy can explain the observed flux of cosmic rays (for works on shock acceleration see, e.g., Fermi 1949; Bell 1978; Lagage & Cesarsky 1983; Blandford & Eichler 1987; Jones & Ellison 1991; Malkov & O'C Drury 2001; Erlykin & Wolfendale 2002; Schure et al. 2012). Pulsars, which are common remnant objects of such explosions, with their magnetospheres, winds, and their nebular regions are also good candidates, and are commonly assumed to be able to accelerate leptons at least up to energies around 10 GeV. Gamma-ray and neutrino telescopes together with intermediate-energy cosmic-ray observatories are likely to determine the origin of Galactic comic rays in the near future.

Recently, some unexpected measurements have also raised interest below the PeV energy range. Indeed, over the last few years a large amount of new high-precision experimental data related to primary electrons and positrons in cosmic rays was obtained with several experiments at these energies: PPB-BETS, ATIC, PAMELA, Fermi-LAT, H.E.S.S., MAGIC, AMS-02 (Yoshida et al. 2008; Chang et al. 2008; Panov et al. 2011; Adriani et al. 2009, 2011; Abdo et al. 2009a; Ackermann et al. 2010, 2012; Aharonian et al. 2009; Blum et al. 2013; Borla Tridon 2011). These measurements have led to one major puzzle: the fraction of positrons compared to electrons increases with energy above 10 GeV, instead of decreasing as predicted by standard cosmic ray source and propagation models. The cause of this deviation of the data from the model is not understood yet, though many astrophysical (often involving pulsars) and more exotic models (many involving Dark Matter) have been proposed.

Another intriguing fact in the TeV to PeV energy range is that several experiments have reported strong anisotropy measurements in the arrival direction distributions of Galactic cosmic rays (Super-Kamiokande, Tibet III, Milagro, ARGO-YBJ, and IceCube (Amenomori et al. 2006; Guillian et al. 2007; Abdo et al. 2008, 2009b; Abbasi et al. 2011a). The data reveal the presence of small-scale (of order some tens of degrees in the sky) and large-scale anisotropies with high detection significance. The large scale anisotropy could be naturally explained by the diffusive transport of cosmic rays within the Galactic magnetic fields (Erlykin & Wolfendale 2006; Salvati & Sacco 2008; Blasi & Amato 2012b). On the other hand, the intermediate and small-scale anisotropies are more difficult to explain. The main difficulty is that the Larmor radius of particles in the TeV-PeV range is shorter than 1 pc for standard magnetic-field strengths and coherence lengths, and the propagation will be totally diffusive over the distance to a typical close-by source capable of accelerating particles to PeV energies (located farther than 1 pc). Various phenomena, such as heliospheric modulation, neutron sources, nearby pulsars, peculiar structures of the local Galactic magnetic fields have been invoked (O'C. Drury & Aharonian 2008; Abdo et al. 2008,

2009b; Vernetto et al. 2009; Abbasi et al. 2011a; Pohl & Eichler 2012; O'C. Drury 2013; Giacinti & Sigl 2012).

In this chapter, we will examine these two enigmas with different approaches: one is a cautious demonstration of a proof of principle, and the other a proposal for an exotic scenario. Both approaches assume that pulsars could be subdominant (as compared to supernova remnants) contributors to the observed cosmic-ray flux. First, we address the question of whether a putative steep fall in the anomalously high positron fraction observed by AMS-02 (and previously by PAMELA), occurring at energies higher than currently measured, could distinguish between the pulsar and dark matter interpretations of the signal. We argue that a scenario where the high-energy positron excess arises from a single bright nearby pulsar is generically capable of explaining a steep cutoff in the spectrum, and so the observation of such a cutoff would not rule out a pulsar interpretation. This is a topical question as the community seems to believe that the presence or absence of a high-energy cutoff would test the origin of the signal.

In a second section, we study the possibility that the Milagro and IceCube hotspots are a manifestation of the peculiar nature of these cosmic rays, and of the presence of molecular clouds near the sources. We propose that stable quark matter lumps or so-called *strangelets* can be emitted in the course of the transition of a neutron star to a more compact astrophysical object. A fraction of these massive particles would lose their charge by spallation or electron capture in molecular clouds located in the immediate neighborhood of their source, and propagate rectilinearly without decaying further, hence inducing anisotropies of the order of the cloud size. With reasonable astrophysical assumptions regarding the neutron star transition rate, strangelet injection and neutralization rates, we can reproduce successfully the observed hotspot characteristics and their distribution in the sky.

2.1. What could we learn from a sharply falling positron fraction?

Delahaye, T., Kotera, K., & Silk, J. 2014, submitted to ApJ, ArXiv e-prints: 1404.7546

The positron fraction, that is, the flux of cosmic-ray positrons divided by the flux of electrons and positrons, has attracted much interest since the publication of the results of the PAMELA satellite (Adriani et al. 2009, 2013). PAMELA has indeed reported an anomalous rise in the positron fraction with energy, between 10 and 200 GeV. These measurements have been confirmed recently by AMS-02 (Aguilar et al. 2013). The intriguing question is what may happen next? The positron fraction must either saturate or decline. In the latter case, how abrupt a decline might we expect?

Antiparticles are rare among cosmic rays, and can be produced as *secondary* particles by cosmic ray nuclei while they propagate and interact in the interstellar medium. The sharp increase observed in the positron fraction is however barely compatible with the most simple models of secondary production. Various alternatives have been proposed, such as a modification of the propagation model (Katz et al. 2009; Blum et al. 2013), or primary positron production scenarios, with pulsars (e.g., Grasso et al. 2009; Hooper et al. 2009; Delahaye et al. 2010; Blasi 2011; Linden & Profumo 2013) or dark matter annihilation (e.g., Delahaye et al. 2008; Arkani-Hamed et al. 2009; Cholis et al. 2009; Cirelli & Panci 2009) as sources. The current data and the uncertainties inherent in the source models do not yet enable us to rule out these scenarios. It is however likely that improved sensitivities at higher energies and a thorough measurement of the shape of the spectrum above $\sim 200\,\mathrm{GeV}$ will be able to constrain the models.

The AMS-02 data presents a hint of flattening in the positron fraction above 250 GeV. Such a feature is expected, as the positron fraction should not exceed 0.5, and hence it should either converge towards 0.5 or start decreasing. We investigate in this section the following question: what constraints could we put on dark matter annihilation and primary pulsar scenarios if the next AMS-02 data release were to show a sharply dropping positron fraction? The community puts forward that the presence or absence of a high-energy cutoff would test the origin of the positron excess signal. A sharp drop could be deemed natural if the positron excess originates from the annihilation of dark matter particles with a mass of several hundred GeV. However, we show in this work that such a feature would be highly constraining in terms of dark matter scenarios. More unexpectedly, we demonstrate that pulsar models could also lead to similar results for a narrow parameter space. Interestingly, we discuss that pulsars lying in this parameter space happen to be the only ones that would be astrophysically capable of contributing to the pair flux at this level.

2.1.1. Method

In order to mimic a sharp drop in the positron fraction measurements, we generate two sets of mock data by extrapolating the AMS-02 data points at higher energies. We assume that the flux keeps rising up to 350 GeV and 600 GeV, and then drops to the level expected for a flux produced purely by secondary cosmic rays (see Fig. 2.1 and Delahaye et al. 2014 for the 600 GeV cut-off case). The relative error bars are assumed to increase by 50% at each energy bin.

To fit this mock data, three components can be considered: i) a standard underlying secondary flux (produced by interactions of primary cosmic rays in the interstellar medium, and inferred from observed cosmic-ray fluxes), ii) far away pulsars likely to contribute to the electron and positron fluxes between a couple of GeV and ∼150 GeV (Delahaye et al. 2010) iii) on top of these, one can add the contribution of another primary electron and positron flux, coming either from a single nearby pulsar or from the Galactic dark matter halo.

We compute the flux and distribution of primary and secondary cosmic rays in the Galaxy following the commonly used two-zone diffusion model, where the stars and Interstellar Medium (ISM) lie in an infinitely thin disk embedded in a large diffusion halo of chaotic magnetic field. Once in the diffusion zone, cosmic rays suffer diffusion, energy losses (mainly inverse Compton and synchrotron; note that Klein-Nishina effects are taken into account here), spallation on the ISM, convection and reacceleration. The latter two effects have not been taken into account here, as they impact only low energy electrons and we are interested here in energies above ∼200 GeV. The various parameters that quantify these phenomena are not known from first principles and must be constrained by data, such as the boron to carbon ratio, that is not sensitive to source modeling. As Maurin et al. (2001) has shown, the parameter space compatible with the data is very large and translates into an equally large uncertainty on the expected positron and electron fluxes that should be sized correctly (Delahaye et al. 2008, 2009). In order to account for this spread, we will discuss our scenarios within three sets of representative parameters labelled *min*, *med* and *max* in Donato et al. (2004) (Table 2.1).

For each of the three propagation parameter sets, we have calculated the underlying secondary positron flux (channel i) as in Delahaye et al. (2009). In this study, we have chosen to use the primary proton

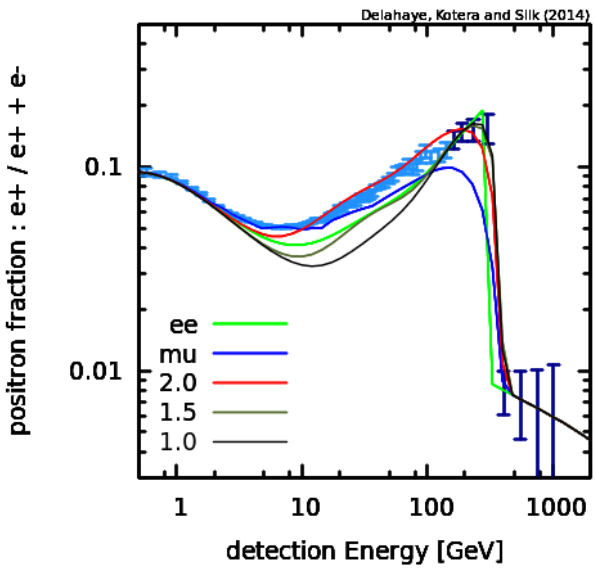

Figure 2.1.: *Best fit fluxes for the max parameter set for a positron drop at 350 GeV. Data up to 350 GeV is from AMS-02 (Aguilar et al. 2013), above this energy, the bins are mock data. Note that for the pulsar cases, a smooth distribution of far away pulsars, with the same injection spectrum (but a lower cut-off) has been added to reproduce the data at intermediate energies (10 to 150 GeV).*

and α fluxes given by Donato et al. (2009) and the production cross-sections of Kamae et al. (2006); Kamae et al. (2007); other choices are possible but such a parameter scan is not within the scope of this work. The electron injection flux is set to follow a power-law that gives a good overall fit to the PAMELA electron data, as well as to the AMS-02 positron fraction data below 5 GeV. Note that electrons are mainly primary cosmic-rays and are hence less straightforward to model than positrons.

For illustrative purposes, in the pulsar case, we have overlaid a second component of distant pulsars (channel ii), following the spatial distribution of Lorimer (2004). We use the the same injection power-law as in channel i, but with a lower cut-off energy, set to minimize the χ^2 between 10 and 150 GeV. This has no impact on the results as this quantity is added after the parameters of the local pulsars are set. A similar exercise could be done for the dark matter scenario by adding flatter annihilation channels like W^+W^-.

At the highest energies, we overlay the contribution of an additional primary flux (channel iii) due to either a dark matter halo, or a single nearby pulsar. For the Dark Matter halo scenario, we have restricted

Table 2.1.: *Propagation parameter sets*

	min	med	max
L [kpc]	1	4	15
D_0 [kpc^2/Myr]	0.0016	0.0112	0.0765
δ	0.85	0.70	0.46

Propagation parameter sets for the three representative cases discussed in Donato et al. (2001). L is the diffusion halo size, D_0 the diffusion coefficient at 1 GeV, and δ the diffusion coefficient power law index: $D(E) = D_0(E/1\,\mathrm{GeV})^\delta$.

our discussion to the two cases where dark matter fully annihilates into electron and muon pairs. Indeed the other annihilation channels do not lead to a sharp electron spectrum. The annihilation cross-section and the mass of the dark matter particle are left free. We assumed a NFW profile for the halo, but the choice of the profile does not affect much the result. As shown by Delahaye et al. (2008), positrons suffer energy losses in the Galaxy and the flux measured at the Earth cannot be affected by the exact dark matter distribution at the Galactic Centre.

In the pulsar scenario, we assume an injection at the single nearby source of the form $Q(E) = Q_0\,E^{-\sigma}\exp(-E/E_\mathrm{c})$ with E_c the cut-off energy and Q_0 defined via the total energy $\mathcal{E}_\mathrm{tot} = \int EQ(E)\,\mathrm{d}E$ integrated between $E_\mathrm{min} = 0.1\,\mathrm{GeV}$ and $E_\mathrm{max} = 10\,E_\mathrm{c}$. For the spectral index σ, we have considered 3 benchmark values (see section 2.1.3): 1.0, 1.5 and 2.0. The maximum energy E_c, the total injected energy $\mathcal{E}_\mathrm{tot}$, as well as the time of injection (pulsar age) and the distance between the source and the Earth are left as free parameters.

Considering that between a couple of GeV and ~150 GeV, far away pulsars could contribute (channel ii), we have required our additional primary source to give a good fit above 150 GeV only (*i.e.* the four highest energy bins of the AMS-02 data and the four mock data points generated as explained previously). The source parameters are then scanned over until the χ^2 is minimised. For each case, we also have computed the maximal value of the anisotropy in order to check that it always remained lower than the maximal value set by AMS-02: 0.036[1]. The best

[1]One might note that the choice of the AMS-02 collaboration to give the anisotropy of the positron ratio Δ (the flux of positron divided by the flux of negative electrons only) instead of the anisotropy in the positron flux (noted $\mathcal{A}$ in the next section) is surprising, as it is not very constraining, compared to individual anisotropies. Indeed, whatever the source of the positron excess it should produce electrons in the same quantity and hence the anisotropy of the positron ratio is expected to be small, even when the positron flux is very anisotropic.

Table 2.2.: *Best χ^2 for pulsar scenarios, drop energy 350 GeV*

χ^2 [$\Delta/10^{-4}$]	min	med	max
$\sigma = 1.0$	0.6 [1.7]	0.4 [0.3]	0.7 [0.2]
$\sigma = 1.5$	1.6 [3.3]	1.0 [3.3]	1.1 [3.3]
$\sigma = 2.0$	2.6 [4.7]	2.8 [4.4]	6.6 [3.5]
$\mu^+\mu^-$	20.3	27.0	61.5
e^+e^-	5.3	1.6	13.7

Best χ^2 for pulsar scenarios with $\sigma = [1, 1.5, 2]$ (first three lines), and for dark matter scenarios, for the three propagation parameter sets defined in Table 2.1 for a drop energy of 350 GeV and in brackets, the corresponding highest anisotropy signal Δ in units of 10^{-4}.

fit results are shown in Tables 2.2.

2.1.2. Results

Table 2.2 presents the best results of our χ^2 analysis for a sharp drop of the positron fraction at 350 GeV. The table displays the values of the best-fit χ^2 (together with the anisotropy signal Δ) for each benchmark case. The corresponding fluxes for the *max* propagation case are shown in Fig. 2.1.

Dark Matter

Not very surprisingly, in the case of a dark matter annihilating solely into $e^+ + e^-$ it is possible to obtain a sharp drop of the positron fraction for most propagation parameters. Note however that in all cases, the annihilation cross-sections (or boost factors) required to fit the data are very high. This is already known for quite some time and raises a large number of issues concerning consistency of such a results with other observations such as anti-protons (Donato et al. 2009), γ-rays (Cirelli et al. 2010), synchrotron emission (Linden et al. 2011) etc.

Pulsars

Our best χ^2 values indicate that some scenarios exist, where single pulsars can lead to a good fit to the data. In order to better assess the allowed parameter space, we perform a broader parameter scan on the pulsar distance, age, and cut-off energy. Our results are

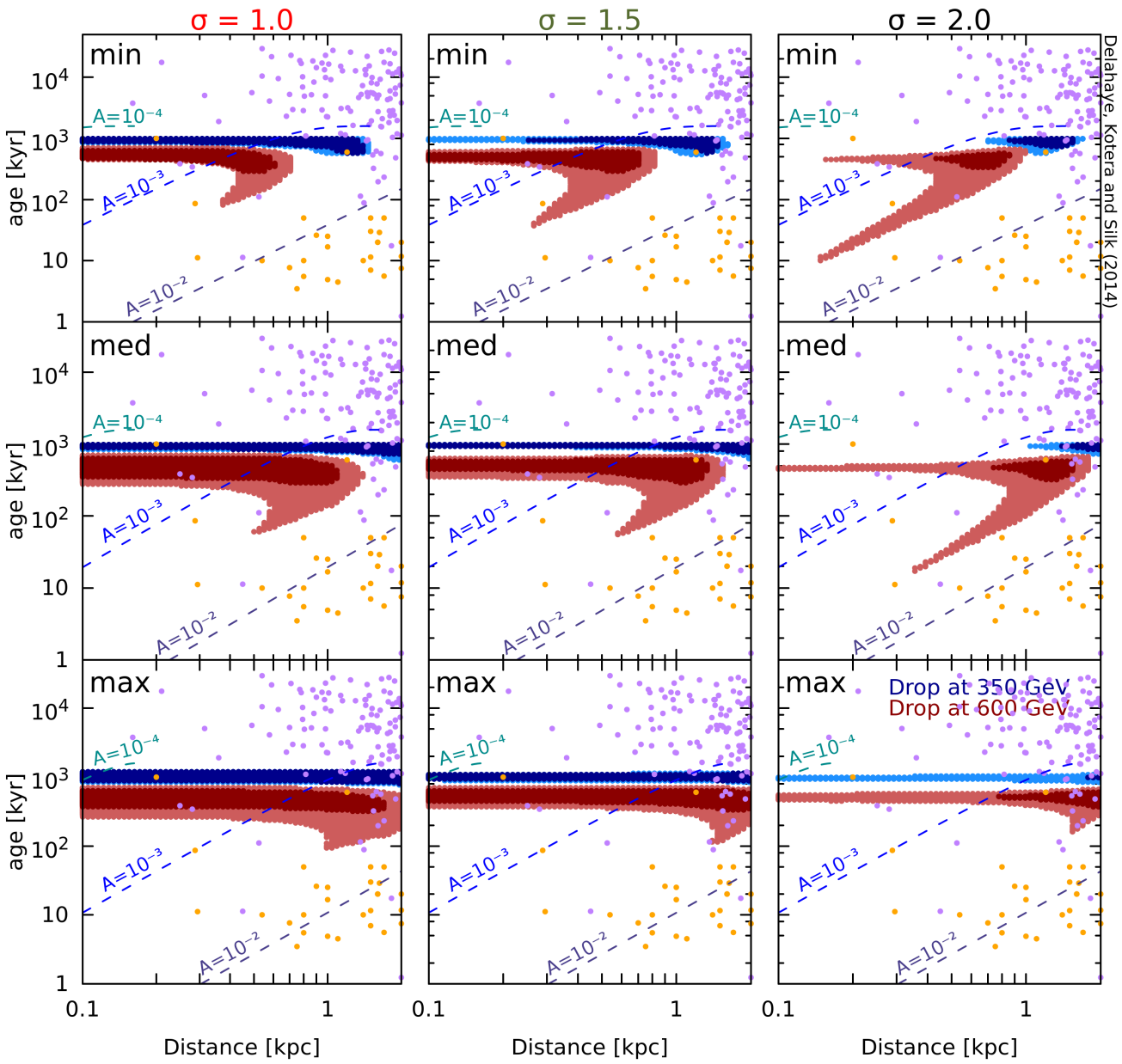

Figure 2.2.: *min med max* (top to bottom), *injection spectral index* $\sigma = 1.0, 1.5$ *and* 2.0 *(left to right) for a sharp drop at 350 GeV (in blue) or at 600 GeV (in red). Dark areas correspond to pulsars leading to* $\chi^2 < 8$ *(the number of degrees of freedom) whereas the shaded area represent the* $2-\sigma$ *contours around the best fits given in Table 2.2 and Table 3 of Delahaye et al. (2014). The blue dashed lines give an estimate of the anisotropies in the positron flux* $\mathcal{A}$ *(not in the positron fraction) induced by a unique pulsar sitting at a given distance and time. This is not a full calculation but an analytical estimate where the secondary background is neglected and the pulsar sits in the direction of the Galactic Center. The purple and orange dots correspond to the existing cosmic ray sources one can find in the ATNF (Manchester et al. 2005) and Green (2009) catalogues.*

presented in Figs. 2.2 and 2.3, where the contours represent the regions where the χ^2 is lesser than the number of degrees of freedom of the fit (dark colors) and 2-σ away from the best fit value (light shades). The bottom plots in Fig. 2.3 display the corresponding energy injected into cosmic rays $\mathcal{E}_{\rm tot}$, as a fraction of a typical supernova explosion energy (10^{51} erg). The relevance of this energy budget is discussed in section 2.1.3.

The shape of the spectra produced by single pulsars is an intricate combination of injection parameters and propagation effects. The influence of the

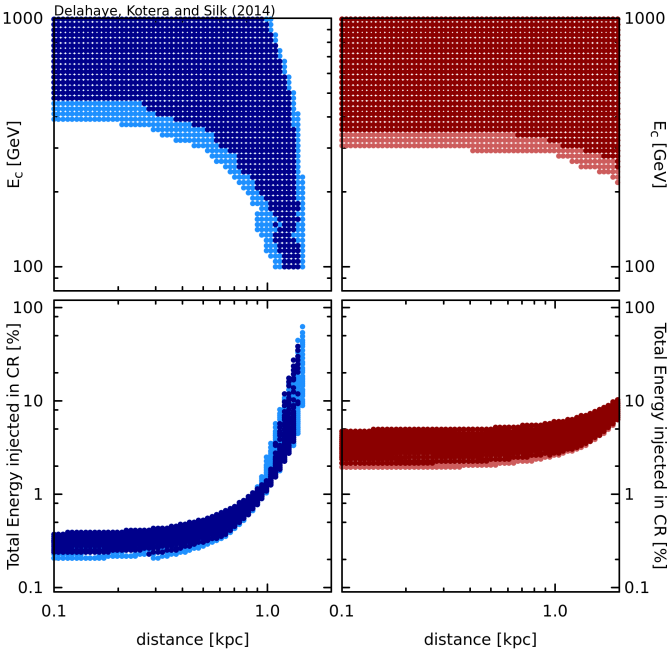

Figure 2.3.: *Energy cut-off at injection (top) and total energy going to cosmic-ray (bottom) for an injection spectrum $\sigma = 1$. The left-hand panels correspond to the min case and a drop at 350 GeV, whereas the right-hand panels are for a drop at 600 GeV and the max propagation parameters.*

various quantities are discussed in detail in Delahaye et al. (2010). Figure 2.4 recalls the effects of the pulsar distance and age on the observed spectral slope and high-energy cut-off.

The position of the cut-off in energy is set solely by the age of the pulsar, given an initial maximum energy E_c. The narrow horizontal bands of fixed pulsar age in Fig. 2.2 correspond to this effect. The higher drop-energy (600 GeV) case is naturally better fit by younger pulsars than the 350 GeV case. The diagonal departure from the horizontal line corresponds to cases where the the cut-off energy is set by E_c. One can also note from Fig. 2.4 that older pulsars lead to a sharper cut-off, whatever the distance.

The other parameters (distance and spectral index) govern the spread of the spectrum and its steepness, down to low energies. Shorter distances and harder spectra lead to more peaked spectra, as required for our fits. These two parameters have opposing effects on the normalization: the flux amplitude decreases with the source distance and increases for harder spectral indices. This explains why, for softer spectral indices, nearby pulsars are excluded, as they are not able to provide enough energy to account for the observed flux. For the *min* propagation case, large distances are excluded for this same reason, as indicated in Fig. 2.3, where the fraction of injected energy saturates at 100% for large distances.

The dashed lines in Fig. 2.2 provide an estimate of the anisotropy (in the case where the pulsar would be the only source and would sit in the Galactic plane). This is the positron flux anisotropy, as opposed to the positron ratio reported by AMS-02. It shows that a sharp positron fraction does not necessarily imply a high anisotropy.

The diffuse cosmic-ray flux scales roughly as $\propto L/D(E)$, where L is the halo size and $D(E)$ the diffusion coefficient. The *min* propagation case is thus intrinsically favoured energetics-wise. Additionally, this case can lead to a narrower peaked spectrum. The anisotropy of the positron flux has however an inverse scaling $\mathcal{A} \propto D(E)/L$, which explains why the anisotropy constraint is strongest for the *min* case, where A is largest. Note also that here all the pulsars have been considered to be in the Galactic plane but should a pulsar be above or bellow the plane, the anisotropy would increase, especially in the *min* case.

To summarize, two regimes appear from Fig. 2.2: a good fit to the sharp drop requires either a relatively old pulsar (horizontal branches of the scatter plots) and then the break is set by the age of the pulsar, independently from the injection cut-off and its distance, or one requires a relatively young and nearby pulsar (diagonal branch in the upper right corner). The parameter space that enables a good fit shrinks considerably as the injection index σ increases.

2.1.3. Discussion

In the pulsar framework, our parameter scan favours a relatively old (a few hundred kyr old) close-by source (within $\sim$ 1 kpc), capable of supplying at least $\mathcal{E}_{\rm tot} \sim 10^{47-48}$ erg into electrons and positrons, accelerated with a hard spectrum. This parameter scan was performed taking into account only propagation arguments. We discuss in this section how likely such a single source scenario is from an astrophysical point of view, in terms of energy budget and given the actual pulsar population.

Pair production and acceleration in pulsars happens in several steps: electrons are initially stripped off the surface of the star by strong rotation-induced electric fields and undergo electromagnetic cascading in a yet unidentified region, which could be the polar cap (Ruderman & Sutherland 1975), the outer gap (Cheng et al. 1986a), or the slot gap (Harding & Lai 2006). The produced pairs are then channelled into the pulsar magnetosphere, and can either escape

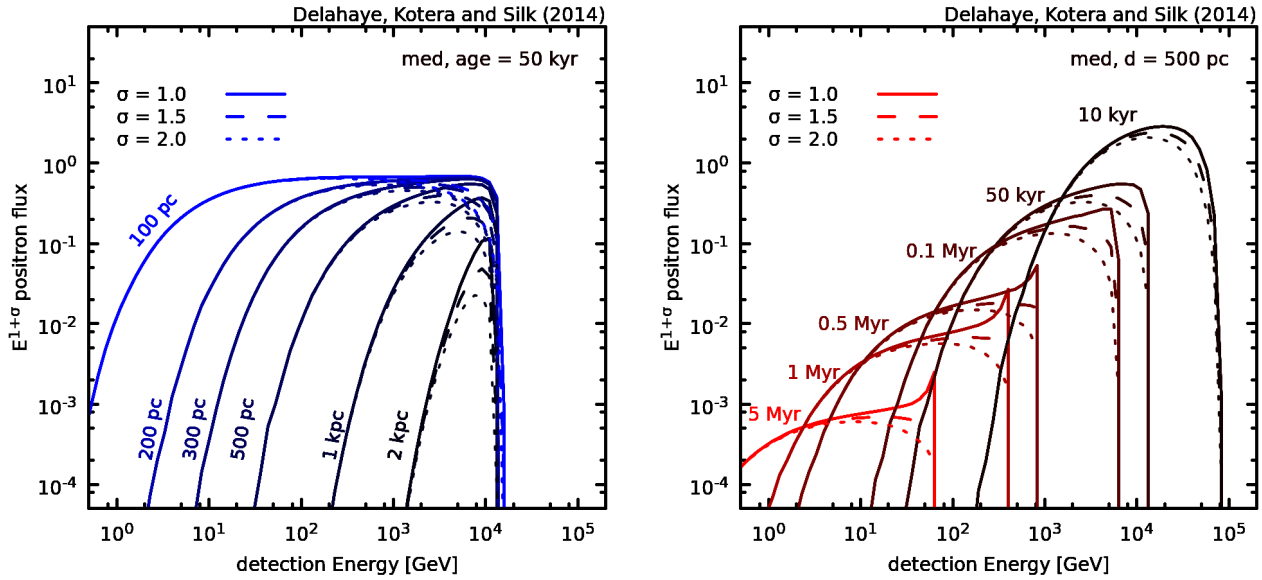

Figure 2.4.: *Impact of the distance (left panel) and of the age (right panel) of a pulsar on the positron flux received at the Earth. Continuous, dashed and dotted lines correspond to an injection respectively of σ =1, 1.5 and 2. The fluxes displayed here are corrected by a factor $E^{1+\sigma}$ to ease the comparison. It clearly appears that distance has little impact on the shape of the flux at high energies. One should also note that the flux coming from old pulsars drops more sharply, whatever the distance.*

following open field lines (Chi et al. 1996), or reach the pulsar wind nebula (PWN), a shocked region at the interface between the wind and the supernova ejecta, where particles can be further accelerated to high energies.

Most pulsars are born with rotation periods $\sim$ 300 ms (Lorimer 2008a), which implies a rotational energy budget of $\sim 10^{46-47}$ erg. Unless a fair fraction of the supernova ejecta energy is injected into particle kinetic energy, it is thus difficult to account for $\mathcal{E}_{\rm tot} \sim 10^{47-48}$ erg required to fit the observed flux for the majority of pulsars. Pulsars that could supply this amount of energy should thus be rare sources, either because they need to spin faster, or because the conversion of the ejecta energy into particle kinetic energy has to be highly efficient.

As long as the pulsar wind is embedded in the supernova remnant, the accelerated pairs lose energy adiabatically via expansion and radiatively via interactions with the magnetic and radiative fields. Blasi (2011) shows however that accelerated pairs can escape in the interstellar medium if they are liberated after the pulsar escapes the parent supernova remnant. This event typically occurs 50 kyr after the initial blast, as can be estimated by assuming an average birth kick velocity of the pulsar. Thus pulsars younger than this age would be naturally ruled out as contributors to the rising positron flux, as they would not have escaped the remnant yet, and accelerated particles would be trapped.

On the other hand, older pulsars cannot contribute to the high-energy end of the spectrum either, because of propagation effects (Fig. 2.4). Positrons produced by these sources would pile-up at intermediate energies (channel ii, mentioned in section 2.1.1).

From Fig. 2.3, one can see that the bulk of the more distant pulsars $\gtrsim$ 1 kpc demand that a (unreasonably) large energy budget be channelled into cosmic rays. A typical pulsar beyond 1 kpc can contribute at a level of $< 1\%$ of the flux of a more nearby pulsar, and hundreds of sources would be needed to reach the same level of flux as one pulsar at a distance closer than 1 kpc.

The anisotropy of the positron flux $\mathcal{A}$ should be stronger than that of the positron ratio Δ on which AMS-02 set an upper limit of 0.036 and hence could be more constraining if detected. However it is not clear that even in the case of a bright source dominating the signal that it would be strong enough to set a strong conclusion. The energy dependence of $\mathcal{A}$ could help as we expect the anisotropy to increase together with the flux in the case of a single pulsar dominating the signal, whereas if the dark matter halo were to dominate, the anisotropy could decrease while the flux increases. This is all the more true if the propagation parameters are close to those of *min*, as this would increase the energy dependence of the anisotropy. The direction of the anisotropy could also be useful if the pulsar or pulsars responsible for the signal are not in the direction of the Galactic

Center. Indeed the pulsar scenario would ultimately be satisfactory only if the brightest pulsar is actually identified and detected.

Finally, the energy spectrum injected by a single pulsar depends on the environmental parameters of the pulsar. The toy model of unipolar induction acceleration in pulsars would lead to a hard spectral slope of index $\sigma \sim 1$ (Shapiro & Teukolsky 1983). More detailed models by Kennel & Coroniti (1984a) suggest that the pair injection spectrum into the pulsar wind nebula should present a power-law (later models and simulation show a maxwellian) distribution due to the transformation of the bulk kinetic energy of the wind into thermal energy, and a non-thermal power-law tail formed by pairs accelerated at the shock. Hybrid and particle-in-cell (PIC) simulations show indeed such a behaviour (e.g., Bennett & Ellison 1995; Dieckmann & Bret 2009; Spitkovsky 2008), and the latest PIC simulations indicate a relatively hard spectral slope $\sigma \sim 1.5$ (Sironi & Spitkovsky 2011) due to acceleration by reconnection in the striped wind.

All these arguments demonstrate that the narrow parameter space pointed out by our scan is astrophysically justified a posteriori. Because such sources should be rare, it is consistent that not more than one of them would be currently operating. The dots in Fig. 2.2 confirm indeed that existing pulsars present in the allowed parameter region are scarce.

In this work, we have considered the possibility that future AMS-02 data may show a positron fraction dropping down abruptly to the level expected with only secondary production, and forecast the implications of such a feature in term of possible injection mechanisms that include both dark matter and pulsars. We have shown that dark matter scenarios would then have to face strong constraints to fit the spectral shape successfully. Pulsar models could also lead to similar results for a narrow parameter space. Interestingly, we have argued that pulsars lying in this parameter space happen to be the only ones that would be astrophysically capable of contributing to the pair flux at this level. Were a sharp steepening to be found, rather surprisingly, we conclude that pulsar models would do at least as well as dark matter scenarios in terms of accounting for any spectral cut-off.

2.2. Strangelets and the TeV-PeV cosmic-ray anisotropies

Kotera, K., Perez-Garcia, M. A., & Silk, J. 2013, Physics Letters B, 725, 196

Several experiments have reported strong anisotropy measurements in the arrival direction distributions of Galactic cosmic rays (CRs) in the TeV to PeV energy range (Super-Kamiokande, Tibet III, Milagro, ARGO-YBJ, and IceCube, Yoshida et al. 2008; Chang et al. 2008; Panov et al. 2011; Adriani et al. 2009, 2011; Abdo et al. 2009a; Ackermann et al. 2010, 2012; Aharonian et al. 2009; Blum et al. 2013; Borla Tridon 2011). The data reveal the presence of large scale anisotropies of amplitude $\sim 0.1\%$. Smaller scale anisotropies of size $\sim 10^\circ - 30^\circ$ are also detected with amplitude a factor of a few lower. Milagro has reported the detection at significance $> 12\sigma$ of two *hotspots* (regions with enhanced CR intensity) with amplitude $\approx 10^{-4}$, at a median energy of 1 TeV. ARGO-YBJ report similar excesses. IceCube observes localized regions of angular scale $\sim 15^\circ$ of excess and deficit in CR flux with significance $\sim 5\sigma$ around a median energy of 20 TeV (Abbasi et al. 2011a).

The large scale anisotropy could be naturally explained by the diffusive transport of CRs within the Galactic magnetic fields (Erlykin & Wolfendale 2006; Salvati & Sacco 2008; Blasi & Amato 2012b). On the other hand, the intermediate and small scale anisotropies are more difficult to explain. The main difficulty resides in the fact that the Larmor radius of particles in the TeV-PeV range is: $r_{\rm L} \approx E/ZeB \sim 1.08\,{\rm pc}\,Z^{-1}(E/1\,{\rm PeV})(B/1\,\mu{\rm G})^{-1}$, where the magnetic field strength of the Galaxy is assumed to be $B = 1\,\mu$G (see Han 2008 for a review). For particles with $r_{\rm L} \ll l_{\rm c}$, where $l_{\rm c} = 10 - 100\,{\rm pc}$ is the coherence length of the Galactic magnetic field (e.g., Han 2008), the propagation will be totally diffusive over a distance $> l_{\rm c}$. Neutrons would propagate rectilinearly, but their decay length around 10 TeV energies is less than 0.1 pc. These scales are far shorter than the distance of any close-by source capable of accelerating particles to PeV energies. Various phenomena, such as heliospheric modulation, neutron sources, nearby pulsars, peculiar structures of the local Galactic magnetic fields have been invoked, but none seem to give an obvious explanation (O'C. Drury & Aharonian 2008; Abdo et al. 2008, 2009b; Vernetto et al. 2009; Abbasi et al. 2011a; Pohl

& Eichler 2012; O'C. Drury 2013; Giacinti & Sigl 2012).

In this section, we propose an exotic scenario for these bizarre and unexplained observations. We study the possibility that the hotspots in the skymap are a manifestation of the peculiar nature of CRs, and of the presence of molecular clouds (MCs) near the sources. Our scenario is built up on one major assumption: that quark matter lumps or so-called *strangelets* could be produced and accelerated while a neutron star (NS) transitions to a quark star (QS). A fraction of these heavy particles would suffer spallation or electron capture in molecular clouds located in the immediate neighborhood of their source, and produce neutral fragments that would propagate rectilinearly without decaying further, hence inducing anisotropies of the order of the cloud size.

2.2.1. Strangelet properties and sources

Strangelets (also referred to as nuclearites) are supposed to be lumps of uds quark matter. According to the Witten hypothesis (Witten 1984), ud matter is metastable and d-quarks decay by weak interaction, $u+d \rightarrow u+s$, to form more stable uds matter. These lumps could be formed in explosive events like a NS undergoing a phase transition to a QS as proposed in dark matter (DM)-driven scenarios (Perez-Garcia et al. 2010; Perez-Garcia & Silk 2011) or in the high-density environments of a compact object merger event (Oechslin et al. 2004). Direct searches are being conducted by, e.g., ground-experiments at the LHC (Alice and CMS experiment with the CASTOR calorimeters) or in space with the AMS-02 spectrometer.

The mass number, A, of a stable strangelet can potentially range from $A \sim 10$ to $A \gg 10^{10}$. When considering a general non-zero strangeness-content, there is a nuclear stability valley for strangelets with baryonic number A and there is a poorly known minimum value of mass number $A_{\rm min} \approx 10 - 600$ (Wilk & Wlodarczyk 1996) below which they are unbound. Typical values of strangelet binding energy are currently uncertain but supposed to be $E/A \sim$ MeV $-$ GeV energies. There is not much information on their possible charge value Z but it should be small and (most likely) positive for finite lumps (Madsen 2000, 2001, 2005b,a, 2006b,a). Several models of strangelets exist that lead to various Z/A dependencies. For example, for ordinary strangelets, $Z = 0.3A^{2/3}$, while for CFL (color-flavour-locked) strangelets $Z \simeq 0.3A^{1/3}$ (Madsen 2005b). Even smaller charge-to-mass ratios are allowed $Z/A \sim -10^{-2} - 10^{-7}$. Experiments such as CREAM and AMS-02 will have the ability to perform a direct measurement of the charge, and infer estimates of Z/A.

If strangelets were responsible for the observed hotspots, they should produce detectable air-showers. This is possible if the kinetic energy per nucleon content, K_N, satisfies $K_N = K_{\rm tot}/A > 1\,$GeV. Measurements indicate a total kinetic energy of particles in hotspots, $K_{\rm tot} \sim E \sim$TeV-PeV, which implies $A \lesssim 10^2 - 10^4$.

Neutron stars have been suggested as possible accelerators of strangelets (Madsen 2005b; Cheng & Usov 2006). Strangelets could be produced for instance in the course of a NS to QS transition (Alcock et al. 1986; Alcock & Olinto 1988). In such events, a fraction $f_{\rm ej}$ of the gravitational energy released can be injected into the expelled outer crust, leading to total kinetic energies $E_{\rm ej} \sim 4 \times 10^{50}(f_{\rm ej}/10^{-3})\,$erg for standard NS mass and radius (Perez-Garcia et al. 2012). The Lorentz factor of the ejected mass can be of order $\Gamma \sim 22\,(f_{\rm ej}/10^{-3})(12\,{\rm km}/R_*)(M_*/1.5M_\odot)^2(10^{-5}M_\odot/M_{\rm ej})$, for NS mass M_*, radius R_*, and ejected mass $M_{\rm ej}$ (Perez-Garcia et al. 2012). Particles of mass number A could then gain energies of order $E_{\rm acc} \sim 21\,(A/10^3)(\Gamma/22)\,$TeV, the typical energy observed in hotspots.

Accelerated stranglets may experience energy losses by interacting with the radiation field close to the NS, and with the baryonic and radiative backgrounds of the supernova (SN) envelope. Recent works (e.g., Bednarek & Protheroe 1997; Blasi et al. 2000; Arons 2003; Kotera 2011; Fang et al. 2012) have concluded that there is room for the escape of accelerated particles. The discussion can be adapted to our case, except that strangelets are likely to have higher binding energies (Madsen 2000), which will further help the escape. Besides, old NS may have a higher chance to undergo a transition (Perez-Garcia et al. 2012), negligible radiative fields and no surrounding SN envelopes.

2.2.2. Interaction with molecular clouds and Hotspots characteristics

Once they have escaped from the source, strangelets diffuse in the magnetized interstellar medium (ISM). The trajectory of strangelets should be totally diffusive, even when assuming a low charge. They can

reach the Earth on a timescale

$$\Delta t = \frac{d_{\rm s}^2}{2D} \sim 6\times 10^5\, Z^{1/3} \times \left(\frac{d_{\rm s}}{1\,{\rm kpc}}\right)^2 \left(\frac{E}{20\,{\rm TeV}}\right)^{-1/3} {\rm yrs}\ , \quad (2.1)$$

where $d_{\rm s}$ is the distance to the source and the diffusion coefficient is set to $D(E) = 1.33 \times 10^{28} H_{\rm kpc}[E/(3Z\,{\rm GeV})]^{1/3}\,{\rm cm}^2\,{\rm s}^{-1}$, with $H_{\rm kpc} \equiv H/(1\,{\rm kpc})$ the height of the Galactic halo (Blasi & Amato 2012a). The ionization and the spallation timescales in the ISM (of average density $n_{\rm ISM} = 0.5\,{\rm cm}^{-3}$) read respectively $\tau_{\rm ion} \sim 7\times 10^{12}\, Z^{-2}(E/20\,{\rm TeV})\,{\rm yrs}$, and $\tau_{\rm spall} \sim 4\times 10^5\,(A/10^3)^{-2/3}\,(n_{\rm ISM}/0.5\,{\rm cm}^{-3})^{-1}\,{\rm yrs}$ (Madsen 2005b), implying that spallation should affect particles only mildly during their flight from sources located within 1 kpc.

Spallation could however play a prominent role if the source is born in or near a molecular cloud. Molecular clouds are the densest regions of the ISM, and consist mainly of molecular hydrogen. Their typical radius in the Galaxy is $R_{\rm MC} \sim 20-50\,{\rm pc}$, and their density $n_{\rm MC} \sim 10^{2-6}\,{\rm cm}^{-3}$. In such regions, the spallation fraction can exceed unity, reaching $r_{\rm spall} = \tau_{\rm esc}/\tau_{\rm spall} \sim 7.5\, Z^{1/3}(R_{\rm MC}/25\,{\rm pc})(n_{\rm MC}/10^3\,{\rm cm}^{-3})(A/10^3)^{2/3}$, with $\tau_{\rm esc}$ the diffusion time of strangelets in the cloud. The electron capture rate for strangelets in clouds with free electron density $\sim \eta_e n_{\rm MC}$ (with $\eta_e \ll 1$) should be a fraction of the ionization rate, of order $r_{\rm ion} \sim 10^{-5} Z^{7/3}\eta_e(n_{\rm MC}/10^3\,{\rm cm}^{-3})$. As strangelets are predicted to be more bound than standard nuclei, these estimates can be viewed as upper limits for spallation. For electron capture, it is possible that the large size of strangelets dominates the effects of the charge, implying a scaling in $\sim A^{2/3}$, and the rates quoted here can be viewed as a lower limit.

A fraction of strangelets undergoing spallation or electron capture (similar to that quoted for regular ions (Padovani et al. 2009)) may generate neutral secondaries. The work of Madsen (2005b) suggests that a tiny parameter space exists where spallation could lead to bound neutral strangelets. Neutral strangelets can then propagate rectilinearly to the Earth and produce a hotspot in the sky of the angular size of the molecular cloud, $\theta_{\rm MC} \sim 14^\circ\,(R_{\rm MC}/25\,{\rm pc})(d_{\rm MC}/200\,{\rm pc})^{-1}$, with $d_{\rm MC}$ the distance of the molecular cloud to the observer. Note that this corresponds roughly to the size of the observed hotspots.

The molecular cloud can radiate a total energy in neutral strangelets of $E_{\rm MC}^{(1)} = \eta E_{\rm ej}\, R_{\rm MC}^2/[l(d_{\rm s-MC})]^2$, with $l(d_{\rm s-MC}) = d_{\rm s-MC}^2 c/(2D)$, the effective distance travelled by a diffusing particle over the rectilinear distance $d_{\rm s-MC}$, separating the center of the source to the center of the molecular cloud. The factor η is a free parameter that accounts for strangelet production rate at the source, and the low strangelet neutralization rate in the molecular cloud. This expression is only valid for $d_{\rm s-MC} > R_{\rm MC}$. If the source is located at the center of a molecular cloud, all the produced particles diffuse in the cloud, and $E_{\rm MC}^{(2)} = \eta E_{\rm ej}$. The total energy of neutral strangelets radiated by the molecular cloud can then be expressed over the whole range of $d_{\rm s-MC}$ as $E_{\rm MC} = [1/E_{\rm MC}^{(1)} + 1/E_{\rm MC}^{(2)}]^{-1}$.

The excess signal in a solid angle $< \Omega$ around one source can be defined as the following signal-to-noise ratio: $\sigma_{<\Omega} = N_{{\rm s},<\Omega}/(N_{{\rm iso},<\Omega})^{1/2}$, where $N_{{\rm s},<\Omega} = L_{\rm MC} A(\alpha,\delta) 4\pi d_{\rm s-MC}^2 \Omega E^{-1}$ indicates the number of events expected in a solid angle $< \Omega$ from a source and $N_{{\rm iso},<\Omega} = E J_{\rm iso,sr} A(\alpha,\delta)$ the corresponding number of events expected for an isotropic background. For a molecular cloud located at coordinates (α,δ), at distance $d_{\rm MC}$, and separated by $d_{\rm s-MC}$ from the source, the signal at energy E can then be estimated as:

$$\sigma(E) = \frac{\eta}{E^{3/2}}\left[1 + \frac{d_{\rm s-MC}^4 c^2}{4D^2 R_{\rm MC}^2}\right]^{-1} \frac{E_{\rm ej}}{\Delta t}\frac{A(\alpha,\delta)^{1/2}}{4\pi d_{\rm MC}^2 \Omega J_{\rm iso,sr}^{1/2}}\ , \quad (2.2)$$

where $A(\alpha,\delta)$ [in ${\rm m}^2$ s sr] is the exposure of an experiment in the direction (α,δ), $J_{\rm iso,sr}(E)$ is the observed cosmic ray flux at energy E, per steradian, and Δt is the diffusion time for particles to travel over a distance $\min(R_{\rm MC}, 2R_{\rm MC} + d_{\rm MC})$. For a source located inside the molecular cloud, the luminosity in neutral strangelets radiated by the molecular cloud at $E = 20\,{\rm TeV}$ is of order $L_{\rm MC} = E_{\rm MC}/\Delta t \sim 3.5\times 10^{40}\,\eta Z^{-1/3}(R_{\rm MC}/25\,{\rm pc})^{-2}\,{\rm erg/s}$.

Figure 2.5 presents contours of the value of σ (Eq. 2.2) for strangelets with $Z = 1$, $A = 10^3$ at $E = 20\,{\rm TeV}$, as a function of $d_{\rm MC}$ and $d_{\rm s-MC}$, for a molecular cloud of radius $R_{\rm MC} = 25\,{\rm pc}$. For each set of distances $(d_{\rm s-MC}, d_{\rm MC})$, the signal σ is calculated for a solid angle Ω corresponding to an angle in the sky of $\min(3^\circ, \theta_{\rm MC})$. This takes into account the minimum smoothing angle of the anisotropy analysis conducted by Milagro and IceCube ($2.1^\circ/\cos(\delta)$ for Milagro, Abdo et al. 2008, and $\sim 3^\circ$ for IceCube, Abbasi et al. 2011a). Cosmic ray measurements indicate $J_{\rm iso,sr}(20\,{\rm TeV}) \sim 5\times 10^{-17}\,{\rm eV}^{-1}\,{\rm s}^{-1}\,{\rm m}^{-2}\,{\rm sr}^{-1}$, and we chose an exposure of $A(\alpha,\delta) = 10^{13}\,{\rm m}^2\,{\rm s\,sr}$,

roughly corresponding to the Milagro exposure at 20 TeV, over 7 years of operation.

In our calculation, we set the efficiency factor to $\eta = 5 \times 10^{-8}$. Efficiencies in the range of $10^{-8} < \eta < 10^{-7}$ lead to reasonable values in terms of σ (as $\sigma \propto \eta$), whatever the relative location of the source and the molecular cloud, and the distance to the molecular cloud. From Eq. 2.2, one can infer the strong dependency of σ on the distance between the source and the molecular cloud: $\sigma \propto d_{\rm s-MC}^{-4}$, when the source is at the border of the molecular cloud. On the other hand, Fig. 2.5 shows that the value of σ is relatively constant as long as the source is at a relatively central position inside the molecular cloud. This range of η thus implies that only molecular cloud within $1-2$ kpc, and only sources *located inside the molecular cloud* can produce a significant hotspot (note also that local molecular clouds are found beyond $d_{\rm MC} \gtrsim 70$ pc).

Such low values of this effective parameter η leave room for combined uncertainties in possibly low strangelet injection at the source, strangelet acceleration, and neutralization efficiencies in the cloud. All these are largely unknown but it is expected that the fraction of strangelet ejected mass at the source should be at most $\sim 1-10\%$ of the mass difference in the transitioning NS and QS configurations (Perez-Garcia et al. 2012). The neutralization rates in the cloud should be a small fraction of $r_{\rm spall}$ and $r_{\rm ion} \propto \eta_e$ for spallation and electron capture respectively.

Magnetic fields in molecular clouds are known to scale approximately with gas density as $n^{1/2}$ relative to the mean Galactic magnetic field. The diffusion coefficient scales in $r_{\rm L}^{1/3} l_{\rm c}^{-2/3} \propto B^{-1/3} l_{\rm c}^{-2/3}$ in the Kolmogorov diffusion regime. Taking into account these stronger fields would thus only result in an order of magnitude difference in σ, and the variations could be absorbed by the uncertainty in the efficiency factor η.

Whether the NS-QS transition actually gives birth to a pulsar is unknown. Hence strangelet sources will not necessarily be found at the position of an active source, and one reasonable assumption would be that they are distributed as old NS. In general these are everywhere, including in molecular cloud. Indeed, the number density of old NS in the Galaxy is of order $\sim 10^{-4}\,{\rm pc}^{-3}$ (Lyne & Graham-Smith 2006), and if 10% of them do not get kicks at birth (i.e., remain in the molecular cloud), their mean separation is 20 pc. Molecular clouds and gamma ray pulsars have a similar distribution on the sky, while radio pulsars cover a much wider age range and have a broader

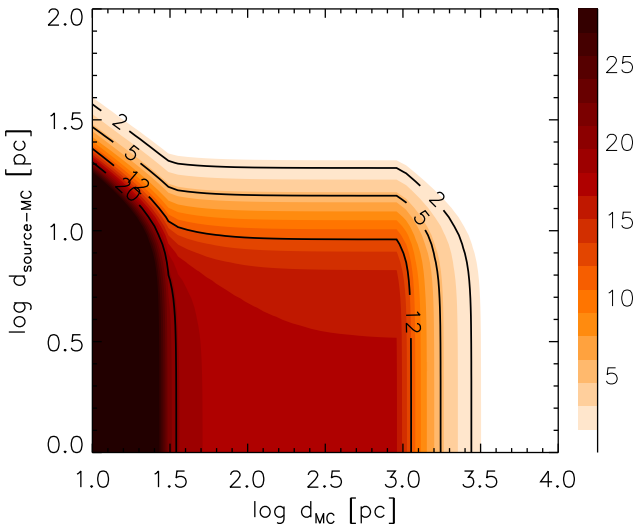

Figure 2.5.: *Particle excess significance σ (Eq. 2.2), as would be observed by Milagro with 7 years of data, at $E = 20$ TeV, as a function of the distance of the molecular cloud to the Earth, $d_{\rm MC}$, and the distance between the source and the molecular cloud, $d_{\rm s-MC}$, for strangelets with $Z = 1$, $A = 10^3$ and a molecular cloud of radius $R_{\rm MC} = 25$ pc, source of luminosity $L_{\rm MC} = \eta 10^{40}$ erg/s, and an efficiency factor $\eta = 5\times10^{-8}$. Color bar: value of σ, black lines: specific numerical values of σ as indicated.*

distribution. The fraction of old neutron stars that are required to undergo NS-QS transition in order to account for the handful of observed hotspots is $\sim 10^{-4}$. The diffusion time of strangelets in molecular clouds, i.e., the time over which each source will be observable, is of order $\Delta t \sim Z^{1/3}\,375$ yrs. This implies a NS-QS transition rate of order $3\times10^{-7}\,{\rm yr}^{-1}$.

2.2.3. Comparison with data and signatures

Most observed hotspots could be produced by molecular clouds in the Gould Belt (a star forming region concentrating many molecular clouds, that forms a ring at a distance from the Sun of $\sim 0.7-2$ kpc), at the location where NS-QS transitions may have occurred. Interestingly, the Milagro hotspot labelled "Region A" (Abdo et al. 2008) lies in the direction of the Taurus Molecular Cloud, the nearest star formation region located at 140 pc, and that covers $\sim 100\,{\rm deg}^2$ in the sky (Murphy & May 1991; Narayanan et al. 2008). "Region 1" of IceCube (Abbasi et al. 2011a) is also in the direction of a remarkable molecular cloud: the Vela Molecular Ridge,

located at $0.7 - 2\,\mathrm{kpc}$ distance, of size $\sim 15°$ in sky (Murphy & May 1991; Narayanan et al. 2008).

It is difficult to predict whether strangelets could produce air-showers conspicuously different from those from ordinary cosmic rays, mainly because their cross-section is not known. Preliminary hadronic simulations with EPOS and CONEX show that the strangelet heavy mass (expected to produce shallow showers with low fluctuations) and its high binding energy (with the oposite effect) could also compensate each other to produce ordinary cosmic ray showers (Schuster & Wiencke 2012). It leaves room for the possibility that the cosmic rays observed by Abbasi et al. (2010, 2011a) actually be strangelets, that were not identified (as long as $A \lesssim 10^2 - 10^4$, see earlier discussion). IceCube also reported composition measurements from 1 to 30 PeV, that are compatible with ordinary cosmic rays (IceCube Collaboration et al. 2013). These estimates combine data of the electromagnetic component of the air-shower at the surface, and the muonic component of the air-shower in the ice. The muon rate for strangelets is expected to increase in $\propto A^{0.1}$, which should not have a noticeable impact for our values of A. This again is consistent with the IceCube reports.

Finally, our model predicts point-like cosmic ray sources farther than a few kpc. In Fig. 2.5, the cut-off of the signal at distances $d_{\mathrm{MC}} \gtrsim 1 - 2\,\mathrm{kpc}$ stems from the limited resolution angle and sensitivity of the instruments, which set the smoothing angle for the anisotropy search. Indeed, as the angular size of the molecular cloud in the sky diminishes, the signal is diluted inside one angular bin, and cannot be distinguished from the noise. With better resolution and sensitivity (with the High Altitude Water Cherenkov Observatory, HAWC, for example), the excess signal could remain high at larger distances, and point-like sources could be spotted.

This scenario could also lead to multi-messenger signatures in secondary neutrinos or gamma-rays. These particles could be produced directly at the source when strangelets are generated, or when particles undergo spallation in the clouds. In the former case, the secondary signal should be point-like. In the latter case, the whole molecular cloud could be illuminated, and the expected gamma-ray flux should be comparable to the product of a multiplicity factor multiplied by the hot spot flux. The multiplicity factor is of the order of the spallation fraction in the molecular cloud or $r_{\mathrm{spall}} \lesssim 10$. The predicted flux over solid angle Ω sr is $N_\gamma(> 1\mathrm{TeV}) \sim 5.10^{-12}(\sigma/10)(r_{\mathrm{spall}}/10)(\Omega/10^{-5})\,\mathrm{s}^{-1}\mathrm{cm}^{-2}$. This should be compared with the expected flux of cosmic ray induced gammas.

We discussed the possibility that strangelets accelerated in nearby NS-QS transitions, and then becoming neutral by spallation or electron capture in molecular clouds, could explain the small-scale anisotropies observed by several experiments at TeV-PeV energies. With reasonable assumptions regarding NS-QS transition rates, particle injection and neutralization rates, we can reproduce successfully the observed hotspot characteristics and their distribution in the sky.

3. Pulsars and ultrahigh energy cosmic rays

The detection, a few decades ago, of cosmic rays with energies that can exceed 10^{20} eV confronted us with some of the most interesting and challenging questions in astrophysics: Where do they come from? How can they be accelerated to such high energies? What do they tell us about these extreme cosmic accelerators? The measurement of a flux suppression at the highest energies (Abraham et al. 2010b), reminiscent of the "GZK cut-off" (Greisen 1966; Zatsepin & Kuzmin 1966) produced by the interaction of particles with the cosmic microwave background photons for propagations over intergalactic scales, has appeased the debate concerning the extragalactic provenance of UHECRs. This feature not only suggests that UHECRs would originate outside of our Galaxy, but also that the sources of the highest energy particles should be located within 100 Mpc distance, in our local Universe. However, the sources remain a mystery and results from the Auger Observatory on the arrival directions and chemical composition of UHECRs make the picture even more puzzling (Kotera & Olinto 2011; Letessier-Selvon & Stanev 2011 for recent reviews).

Young pulsars have been scarcely discussed as sources of high and ultrahigh energy cosmic rays (UHECR) in the literature. However, the production of UHECRs in these objects could give a picture that is surprisingly consistent with the latest data measured with the Auger Observatory. Here we discuss the production of high and UHE cosmic rays in pulsars and compare the propagated UHECR observables from the pulsar population with the available data.

3.1. A quest for sources of ultrahigh energy cosmic rays

Kotera, K. & Olinto, A. V. 2011, ARAA, 49, 119

The quest for sources of UHECRs is first rendered difficult by sheer astrophysical issues. Cosmic rays are charged particles and the Universe is magnetized on various scales. Our poor knowledge of these magnetic fields makes the task of back-tracking particle trajectories to their sources quasi-impossible to date. Besides, the intricate workings of the most powerful astrophysical objects of the Universe, which likely are the sources of UHECRs is not well understood, which complicates further the problem. To these astrophysical issues are added Particle Physics issues: UHECRs arrive on Earth with energies that cannot be reproduced on Earth. The hadronic interactions governing the airshower development of a UHECR entering the Earth atmosphere, is thus unknown. This element is albeit crucial, as this airshower is the information we detect experimentally, from which one has to deduce the properties of the primary particle. Most of all, the difficulty of UHECR science resides in their natural low flux impinging the Earth, that necessitates the construction of larger and larger observatories, in order to be able to collect enough particles and increase statistics.

After many decades of efforts to discover the origin of cosmic rays, current observatories are now reaching the necessary exposure to begin unveiling this longstanding mystery. By mid-2014, the Pierre Auger Observatory and the Telescope Array have collected about 120 and 50 events above 5.7×10^{19} eV respectively.

To answer the question of the origin of UHECRs, the observational information we possess are the following: from the detection of UHECRs themselves, we have measurements of their energetics, their chemical composition, and their arrival directions in the sky. One might also want to cross-correlate this information with observations of secondary messengers that are produced together, or by these ultrahigh energy particles, namely gamma-rays and neutrinos. In what follows, we will examine these pieces of information one by one to try to dig out the most of each observable. The secondary messengers will be discussed separately in Chapter 5.

3.1.1. Clues from the energy spectrum

The observed UHECR energy spectrum is a well of quite solid information. The measurement of the flux first gives us an indication on the energy budget that the population of UHECR sources have to supply. The estimated budget is of order

$\dot{\mathcal{E}}_{\rm UHECR} \sim 0.5 \times 10^{44}\,{\rm erg\,Mpc^{-3}\,yr^{-1}}$ at $E = 10^{19}\,{\rm eV}$ (Katz et al. 2009).

The steep decline in flux above about 30 EeV is reminiscent of GZK cutoff (Greisen 1966; Zatsepin & Kuzmin 1966). A similar cutoff could however be produced by a maximum acceleration energy $E_{\rm max}$ at the source. Another important feature is the hardening of the spectrum at a few EeV (the ankle – see data points in Fig. 3.5), which may be caused by the transition from Galactic to extragalactic cosmic rays or by propagation losses if UHECRs are mostly protons.

The detection of particles at energies above 10^{20} eV implies 1) that sources have to be able to accelerate particles up to these energies, and 2) that the sources of these particles lie within a few hundreds of megaparsecs, as they would have experienced severe energy losses if they had travelled from further away.

Criterion 1) can be further translated into a necessary condition on the source parameters. In order to be able to accelerate particles to $E > 10^{20}$ eV, sources must first confine them, i.e., the Larmor radius of the particles in the acceleration site has to be smaller than the size of the source (Hillas 1984). This statement, called the Hillas criterion, is helpful to make a first selection of sources that could be potential accelerators. The surviving candidates are Active Galactic Nuclei (AGN) with their black holes, their jets and their hot spot regions as possible acceleration sites, shock regions in clusters of galaxies, gamma-ray bursts (GRBs) and magnetized pulsars. A study of the possible acceleration mechanisms also leads to a more precise criterion on the magnetic luminosity of the source (defined as a fraction $\epsilon_{\rm B}$ of the luminosity in the accelerating outflow: $L_{\rm B} = \epsilon_{\rm B} L_{\rm jet}$), necessary to accelerate particles above $E > 10^{20}$ eV. The condition reads: $L_{\rm B} > 10^{45.5}\,{\rm erg\,s^{-1}}\Gamma^2\beta^{-1}$, where Γ and β are the Lorentz factor and the velocity of the flow Lemoine & Waxman (2009). Note that the possible candidate sources can be split into two categories: steady sources emitting particles continuously over the long lifetime of the object, and transient source producing a short burst of cosmic-rays. We will see in the following that these two types of sources can lead to different observable signatures.

3.1.2. Clues from the chemical composition

The latest composition measurements at the highest energies reported by the Auger Observatory (Abraham et al. 2010a; Abreu et al. 2011; The Pierre Auger Collaboration et al. 2013) point towards a chemical composition of UHECRs that evolve from a proton dominated composition at a few EeV toward an iron dominated composition at around 40 EeV (see data points of Fig. 3.6). At the highest energies, the data is not compatible with a light composition (Abreu et al. 2011). The Telescope Array results show the same trend within the systematics (Tameda et al. 2011; Pierog 2013).

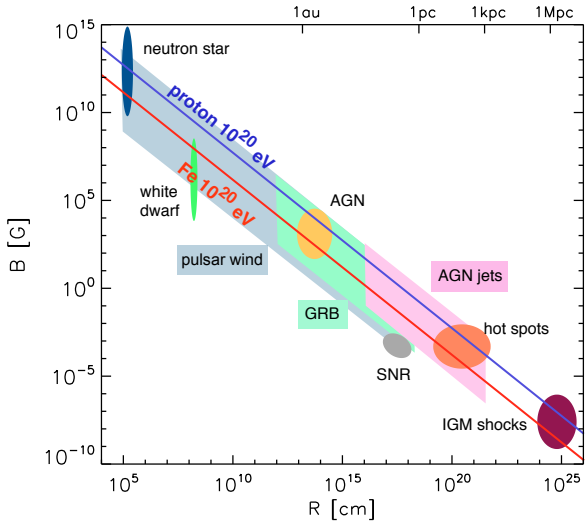

Figure 3.1.: *Updated Hillas (1984) diagram. Above the blue line protons can be confined to a maximum energy of $E_{\rm max} = 10^{20}$ eV. Above the red line, iron nuclei can be confined up to $E_{\rm max} = 10^{20}$ eV. The most powerful candidate sources are shown with the uncertainties in their parameters (B, R) (their magnetic field strength and size). Adapted from Kotera & Olinto (2011).*

From a propagation point of view, heavier nuclei are favored compared to light elements for a given energy as they can travel hundreds of megaparsecs before losing their energy by photo-disintegration processes on the cosmic backgrounds due to their lower energy per baryon (e.g., Stecker & Salamon 1999; Bertone et al. 2002; Allard et al. 2005, 2008; Hooper et al. 2005). Nuclei of charge Z can also be in principle accelerated to an energy typically Z times larger than protons in a given electromagnetic configuration. Propagation models where a heavy composition arises at the highest energies due to a combination of a low proton maximum acceleration energy (around 10 EeV) and Z times higher maximum energies for heavier elements (present in a slightly higher abundance than Galactic) have been shown to reproduce the composition trends observed by Auger (Allard et al. 2008; Aloisio et al. 2009). However, these works focus on the propagation, and

do not provide a plausible source for the injection of these specific compositions. The problem of finding powerful sources that inject mainly these low abundance elements and of their escape from the acceleration site remains open.

Heavy nuclei dominated injection models are quite rare in the astrophysical literature of candidate sources. A direct injection of large proportions of heavy nuclei into an acceleration region requires either an initial metal-rich region, or an efficient nucleosynthesis in the accelerating outflow. Injection is not the only weak point of this scenario: because the acceleration sites are usually dense in radiative and baryonic backgrounds, the escape of nuclei from these regions is not obvious. Many works have shown the difficulty to overcome these problems in AGN, clusters and GRBs (Pruet et al. 2002; Lemoine 2002; Wang et al. 2008; Murase et al. 2008b; Horiuchi et al. 2012). On the other hand, pulsars, due to their metal-rich surfaces are a naturally good candidate for iron injection and acceleration. Blasi et al. (2000); Arons (2003); Fang et al. (2012) further argued that accelerated particles could escape the site and the environment of the source.

3.1.3. Clues from the arrival directions in the sky

Kotera, K. & Lemoine, M. 2008, Phys. Rev. D, 77, 123003

Kalli, S., Lemoine, M., & Kotera, K. 2011, A&A, 528, A109

Oikonomou, F., Kotera, K., & Abdalla, F. B. in prep., J. Cos. and Astro. Phys.

The interpretation of arrival directions of UHECRs in the sky is intricate, and intimately linked to our (yet poor) understanding of the magnetic fields in the Universe. Intergalactic magnetic fields that spread between the sources and us induce deflections on the charged UHECR trajectories, causing spatial and temporal decorrelations. The latter is noticeable if the source is of transient type: deflected cosmic rays arrive on Earth with a time delay compared to the photons and other undeflected particles. This delay is of order 10^4 yrs for one degree deflection over 100 Mpc. This implies that by the time UHECRs reach us, the transient source is already extinguished, erasing any direct event/object correlation.

Though intergalactic magnetic fields are the key to back-track cosmic-ray trajectories to their sources, our knowledge of the subject is limited, due to the lack of observations. The *non*-detection of any signal sets an upper limit to the field strength B and its coherence length λ of $Bl_{\rm coh}^{1/2} < 1-10\,{\rm nG\,Mpc}^{1/2}$ (Ryu et al. 1998; Blasi et al. 1999). The heavy numerical simulations that try to construct a mock magnetic field distribution by injecting MHD equations into cosmological simulations lead to discrepant results (Dolag et al. 2005; Sigl et al. 2004; Das et al. 2008). The study of propagation of UHECRs in such a situation is complicated, but many authors have endeavored to build up predictions and models (Dolag et al. 2005; Sigl et al. 2004; Das et al. 2008; Takami & Sato 2008; Kotera & Lemoine 2008b). The precise role of extragalactic magnetic fields in UHECR propagation may be clarified in the future through extensive Faraday rotation surveys (see, e.g., Beck et al. 2007) and indirect measurements of gamma-ray halos around blazars (e.g., Neronov & Semikoz 2009). Meanwhile, it is interesting to note that for standard types of intergalactic magnetic fields, studies converge on predicting deflection of less than $\sim 3^\circ$ above $E_{\rm GZK} \equiv 6\times10^{19}$ eV for protons. The Galactic magnetic field, comparatively better known, should also be taken into account (see Kotera & Olinto 2011 for references).

The arrival directions of UHECR above $E_{\rm GZK}$ seen by Auger present two main characteristics: Auger reports a hint of correlation with the large scale structures (Abreu et al. 2010; The Pierre Auger Collaboration et al. 2013), but most strikingly, one observes no powerful source in the arrival direction of the highest energy events. Because standard intergalactic magnetic fields should lead to low proton deflection, one expects that steady sources (such as AGN), should be visible behind the arrival directions of UHECRs, unless they are heavy nuclei or if the intergalactic magnetic field is particularly strong, inducing in both cases important deflections.

The observed hints for a departure from isotropy at energies beyond the GZK cutoff, remain insufficient to draw conclusions as to the sources of UHECRs with available data (e.g. Kashti & Waxman 2008; Abreu et al. 2010; Oikonomou et al. 2013). The prospects for source identification with a next-generation detector are debated as a result of the absence of a clear correlation signal with luminous sources so far and of the recent experimental evidence for an increasingly heavy UHECR composition at the highest energies. Studies by Blaksley et al. (2013) and d'Orfeuil et al. (2014) show however that even for the most unfavourable composition scenarios (with, e.g., no protons accelerated to the highest energies), JEM-EUSO should allow the measurement of a significant anisotropy signal, assuming the sources to follow the spatial and luminosity distribution of the 2MRS galaxy catalog.

In Oikonomou et al. (in prep.), instead of focusing on the high energy end where the number of sources is reduced to a few, we concentrated on the lower energy range of the future instruments ($E \gtrsim 50\,\mathrm{EeV}$), where the sources are numerous enough to imprint a clustering pattern in the sky, and thus possibly in the particle arrival directions. Under these limits, the anisotropy signal should be dominated by the clustering of astrophysical sources *per se* in the large-scale structures, and not the clustering of events around individual sources. We demonstrated that an order-of-magnitude increase in statistics compared to the current data would allow to discriminate a large variety of astrophysical models, provided that a subsample of light elements can be extracted, and that it represents a fraction of $\gtrsim 30\%$ of the overall flux, sensitive to the UHECR source number density. Discrimination is also possible with the entire dataset as long as the composition is proton-dominated.

For transient sources (such as gamma-ray bursts or newly born pulsars), due to the time delay between rectilinearly propagating photons and the deflected cosmic rays, one does not expect to observe correlating counterparts. The distribution of events in the sky should however follow closely the large scale structure with a possible bias (Kalli et al. 2011a). The measurement of such a bias could be an evidence to help distinguish between transient and steady sources. It requires however more than 10^3 events, which can be collected by the next generation of UHECR detectors.

Another information given by the distribution of the arrival directions is the absence of multiplets, namely cosmic ray events arriving with little angular separation in the sky. This lack can be used to constrain the apparent number density of sources to $n_0 > 10^{-5}\,\mathrm{Mpc}^{-3}$, if cosmic rays are protons (Kashti & Waxman 2008; Takami et al. 2009), a simple evaluation leading to $n_0 \sim 10^{-4}\,\mathrm{Mpc}^{-3}$ (Takami et al. 2009), and models with $\bar{n} < 10^{-5}\ \mathrm{Mpc}^{-3}$ are strongly disfavoured (Abreu et al. 2013). The low density of steady candidates: clusters of galaxies ($10^{-6}\,\mathrm{Mpc}^{-3}$), FRI-type ($10^{-5}\,\mathrm{Mpc}^{-3}$), and FRII-type radio-galaxies ($10^{-8}\,\mathrm{Mpc}^{-3}$) might not be compatible with the lack of multiplets in the case of proton composition. For transient sources, the apparent n_0 and real ρ_0 number densities of proton UHECR sources are related via the cosmic ray arrival time spread δt due to magnetic fields: $\rho_0 \sim n_0/\delta t$ (Murase & Takami 2009). The time spread δt is bounded on its lower end by the lower limit of the Galactic magnetic field, and on its upper end by the upper limit on the intergalactic magnetic field. By intersecting the information on the required density with the required energy budget estimated earlier, one finds that most transient sources (AGN flares, High and Low luminosity GRBs) only tightly meat the requirements for UHECR production (Murase & Takami 2009). On the other hand, pulsars seem to easily fulfill both criteria.

To be able to dig more information out of the available UHECR observables, it appears necessary to increase drastically the statistics and to turn to the next generation of cosmic ray experiments, such as JEM-EUSO. JEM-EUSO is proposed to be mounted on the International Space Station in $\sim$ 2020. If launched it will survey the night sky for the ultra-violet fluorescence and Cherenkov radiation produced when a UHECR hits the Earth's atmosphere (Adams et al. 2012) with a near uniform exposure over the full sky. Depending on the operation mode JEM-EUSO is expected to reach $9-20$ times the annual Auger exposure at 100 EeV. In *nadir* mode it will start to be sensitive to UHECRs at energy $E \geq 40$ EeV and will be fully efficient beyond $60-70$ EeV. Meanwhile, one might perform a case by case study of candidate sources, and examine their acceleration potential using, for example, multi-wavelength observations of these objects. In the next section, we will concentrate on the case of newly-born rotation-powered pulsars, which, from the criteria covered above, seem to be a promising candidate.

3.1.4. A promising candidate source: newly-born pulsars

The possible candidate sources of ultrahigh energy cosmic rays (UHECRs) have been progressively narrowed down to a handful of objects over the last decades, but the major culprit has not been yet identified. Among the most promising sources, active galactic nuclei (AGN) with their black holes, jets, hotspots, and flares, as well as gamma-ray bursts (GRBs), including low-luminosity GRBs associated with trans-relativistic supernovae, are heavily plebiscited (see review Kotera & Olinto 2011 and references therein). A contender that was introduced early on by Venkatesan et al. (1997); Blasi et al. (2000); Arons (2003) and has been resuscitated more recently by Refs. Murase et al. (2009); Kotera (2011); Fang et al. (2012, 2013b) are magnetized and fast-spinning neutron stars. These objects combine many advantages: their rotation speed endows them with a large energy reservoir ($E_{\mathrm{rot}} \sim 2 \times 10^{52}\,\mathrm{erg}\, I_{45} P_{-3}$,

with I the star inertial momentum and P its spin period, for an isolated new-born pulsar spinning close to the disruption limit)[1], and their population density ($\dot{n}_{\rm s} \sim 3 \times 10^{-4}\,{\rm Mpc}^{-3}\,{\rm yr}^{-1}$ Lorimer 2008b) is high enough to allow a comfortable total energy budget. The energy injected into UHECRs is of order $\mathcal{E}_{\rm UHECR} \sim 0.5 \times 10^{45}\,{\rm erg\,s}^{-1}$ (Katz et al. 2009), which implies that a fraction of order 10^{-4} of the neutron star population is required to achieve the UHECR flux level. In addition, the latest results reported by the Auger Observatory point towards a chemical composition of UHECRs that is not compatible with a light composition at the highest energies (Abreu et al. 2011). Unlike for AGN and GRBs for which heavy nuclei production is rather challenged (Lemoine 2002; Pruet et al. 2002; Horiuchi et al. 2012), neutron stars, with their metal-rich surfaces, are a natural spot to produce heavy nuclei.

In what follows, we review and update the discussions related to the production of UHE heavy nuclei in newly-born pulsars. In Section 3.2 we study the possibility of injecting and accelerating cosmic rays at ultrahigh energies in pulsar winds. In Section 3.3, we examine the escape of UHECRs from the surrounding supernova ejecta. In Section 3.4 we discuss the implications of the newly-born pulsar model in view of the available UHECR observations.

3.2. Injection and acceleration of high energy cosmic rays in pulsar winds

Lemoine, M., Kotera, K., & Petri, J. in prep.
Fang, K., Kotera, K., & Olinto, A. V. 2012, ApJ, 750, 118

The reader may refer to Appendix A for the derivation of general properties of pulsar wind nebulae. The notations used in this chapter follow those of the Appendix.

3.2.1. Heavy nuclei injection

Although the surface of the rotating neutron star is thought to be a natural source of Iron, X-ray spectra of pulsars have shown evidence for Helium (Sanwal et al. 2002), and Carbon, Oxygen, and Neon (Heinke & Ho 2010; Mori & Hailey 2003). In addition, the material leftover from the progenitor star is likely to be in the Carbon group (mostly Oxygen, see e.g., Woosley & Weaver 1995; Arnett 1996; Woosley et al. 2002; Dessart et al. 2012).

One can mention three channels via which intermediate and heavy ions could be seeded in the neutron star wind. Note that scenarios of pulsar winds loaded with heavy nuclei give a satisfactory explanation to some observations. For instance, the morphological features of the Crab Nebula could be the signature of resonant scattering of pairs of electrons and positrons by heavy nuclei (Hoshino et al. 1992; Gallant & Arons 1994).

The classical argument that applies best in our scenario is that iron nuclei can be stripped off the neutron star surface, as has been suggested by Ruderman & Sutherland (1975) and Arons & Scharlemann (1979). Strong electric fields combined with bombardment by particles can extract ions from the polar cap regions, where the co-rotation charge is positive provided that $\mathbf{\Omega} \cdot \mathbf{B} < 0$. The surface of a neutron star being composed mainly of iron-peaked elements, it is possible that heavy nuclei get injected in the wind by these means.

Heavy nuclei loading of the pulsar wind by mixing of the stellar material via Kelvin-Helmholtz instabilities or oblique shocks was also proposed (Zhang et al. 2003; Wang et al. 2008). This mechanism requires however that a jet goes through the stellar core, a case that is not considered in the present study. Kelvin-Helmholtz instabilities might also occur at the interface between the wind nebula and the supernova remnant (Jun 1998; van der Swaluw et al. 2004), but it is unlikely that the envelope in that region has a metallicity high enough to mix large amounts of heavy nuclei in the wind.

The nucleosynthesis of heavy elements by r-process in the neutrino-driven wind at the very early phase of the proto-magnetar formation has also been discussed by Metzger et al. (2011a,b). These authors find that the production rate of nuclei with $A \gtrsim 56$ can be important during the first 1 to $\sim$a few 100 s, when the electron fraction Y_e could be fairly low, the wind expansion time $\tau_{\rm exp} \lesssim 10^3$ s, and the entropy $S \lesssim 100\,k_{\rm b}\,{\rm nucleon}^{-1}$, as is required for a successful r-process (see, e.g., Hoffman et al. 1997). Though these results are obtained for the case of a highly magnetized proto-magnetar driving a jet (as in Bucciantini et al. 2007), they can be applied in a non-collimated mildly magnetized wind case, as the evolution of S and $\tau_{\rm exp}$ is mostly ruled by thermal ingredients (and the rotation speed) in the times considered. However, we will see in the next section that the supernova envelope at $t \sim 10 - 100$ s is too dense to allow the escape of particles, whatever their

[1] Here and in what follows, quantities are labelled $Q_x \equiv Q/10^x$ in cgs units unless specified otherwise.

mass number. At later times, as the wind cools and becomes relativistic, the neutrino heating efficiency drops, shutting off the r-process. It is thus unlikely that this channel can seed heavy nuclei in the wind in our framework.

3.2.2. Maximum acceleration energy

The acceleration mechanism of cosmic rays up to ultrahigh energies in neutron stars or their environments is the main weakness of this source scenario. A toy model presented in Appendix B can help to get some hints on the problems.

Our poor knowledge of the neutron star magnetospheres, winds, nebulae and termination shocks (at the interface between the wind and the surrounding supernova ejecta) is central to the difficulties encountered in building a detailed acceleration model, consistent with the observations and the leptonic emission counterparts. The radiation due to pairs itself is challenging to explain, and despite an increasing experimental and theoretical effort been put to understand the working of neutron star outflows and nebular emissions, the community is still struggling to solve fundamental problems (see e.g., reviews by Arons 2002; Kirk et al. 2009), such as how and where pairs are been accelerated, or the related so-called σ-problem (how to reconcile the very high level of magnetization σ of the wind close to the light cylinder, with the low level inferred from leptonic emission observations downstream of the termination shock). How exactly pairs are being accelerated remains also an unknown. One theory is that Fermi-type processes takes place at the termination shock and boosts to higher energies the particles already accelerated to a high Lorentz factor in the wind, via reconnection for example (Sironi & Spitkovsky 2011).

One certainty however is that neutron stars spin down, and subsequently, their rotational energy is channelled via their winds towards the outer medium. We assume that, as the observations suggest for the Crab pulsar, that the electromagnetic luminosity, $L_{\rm w}$, is efficiently converted into kinetic luminosity, $\dot{N}mc^2 \equiv \dot{N}_{\rm GJ}\left(m_{\rm i}c^2 + 2\kappa m_e c^2\right)$ (with $\dot{N}_{\rm GJ}$ the Goldreich-Julian charge density, Eq. B.6, Goldreich & Julian 1969, $m_{\rm i} = Am_p$ the ion mass and κ the pair multiplicity), e.g., at the termination shock (Lyubarsky 2003). Particles can then reach a Lorentz factor of

$$\gamma_{\rm diss.} \simeq \frac{1}{1+\sigma_{\rm PWN}}\frac{L_{\rm w}}{\dot{N}mc^2} \simeq \frac{1.8\times 10^9}{(1+\sigma_{\rm PWN})\,(1+x_{\rm i})}\,\kappa_4^{-1}P_{-3}^{-2}B_{13}R_{\star,6}^3\ . \quad (3.1)$$

where B is the dipole magnetic field strength of the star, $R_\star$ its radius and $x_{\rm i} \equiv m_{\rm i}/\left(2\kappa m_e\right)$ the ratio between the energy carried by the ions to that carried by pairs (Lemoine et al. in prep.). If ions of charge $Z_{\rm i}$ are injected at a rate $\dot{N}_{\rm GJ}/Z_{\rm i}$, $x_{\rm i} \equiv m_{\rm i}/\left(2Z_{\rm i}\kappa m_e\right)$, so that $x_{\rm i} \lesssim 1$ for $\kappa \gtrsim 10^3$.

The magnetization parameter $\sigma_{\rm PWN}$ relates the Poynting flux to the matter energy flux downstream of the termination shock; in the comoving wind frame, it is defined as $\sigma_{\rm PWN} \equiv B_{\rm PWN}^2/\left(4\pi nmc^2\right)$, with $nmc^2 \equiv n_{\rm i}m_{\rm i}c^2 + 2\kappa n_e m_e c^2$ the rest mass energy density, $B_{\rm PWN}^2/4\pi$ the electromagnetic energy density downstream of the shock, κ defining the multiplicity factor for pairs achieved through pair cascade in the magnetosphere[2].

According to the value of κ, that can range between $10 - 10^8$ in theory (a highly debated quantity, see e.g., Kirk et al. 2009), the energy conversion can be efficient enough to enable protons to reach energies at neutron-star birth

$$E_0 \sim 1.5\times 10^{20}\,{\rm eV}\,A_{56}\,\eta\,\kappa_4^{-1}P_{\rm i,-3}^{-2}B_{13}R_{\star,6}^3\ , \quad (3.2)$$

assuming $x_{\rm i} \ll 1$ and where we have noted $\eta \leq 1$ the luminosity conversion efficiency. In the case when the conversion is not fully efficient, stochastic types of acceleration could take place at the shock to further push the maximum acceleration energy to the confinement limit $\gamma_{\rm conf} = ZeB_{\rm PWN}R_{\rm PWN}/(Am_pc^2)$ (where $B_{\rm PWN}$ and $R_{\rm PWN}$ represent respectively the pulsar wind nebula magnetic field and radius), which can reach values $> 10^{11}$ over the spin-down timescale for neutron stars with parameters $B \gtrsim 10^{12}$ G and initial rotation period $P_{\rm i} \sim 1$ ms (Lemoine et al. in prep.).

Note that the maximum acceleration energy in Eq. (3.2) scales as the mass number A, while for a unipolar induction toy-model described in Appendix B (Eq. B.4), the scaling goes as Z. The calculations performed in Section 3.3 and Chapter 4 were done prior to the acceleration study described in this section, and therefore are based on the energies given by the toy model (Eq. B.4). For a standard multiplicity κ_4, one notices however that the two energies differ only of a factor of $A/Z \sim 2$. The difference also stems from the acceleration efficiency being taken as $\eta = 0.1$ in Section 3.3, while a full efficiency is assumed here.

[2] We have implicitly assumed a cold MHD wind, composed of $e^+ - e^-$ pairs of proper density κn_e with a small admixture of ions, of proper density $n_{\rm i}$.

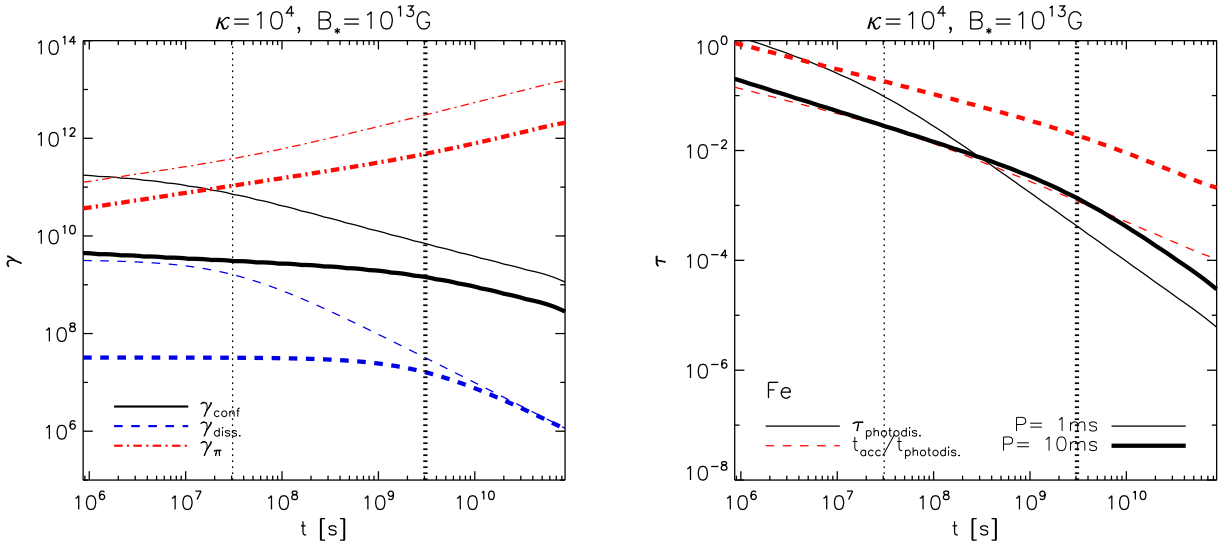

Figure 3.2.: Left: *Comparison of maximum Lorentz factors for iron nuclei confinement ($\gamma_{\rm conf}$, solid lines), acceleration ($\gamma_{\rm diss.}$, dashed lines) and energy loss by photo-disintegration (γ_π, red dot-dashed lines), for pulsar initial rotation period $P_{-3} = 1, 10$ (increasing thickness), dipole magnetic field $B_{13} = 1$, leptonic multiplicity $\kappa_4 = 1$, $\eta_{\rm rad} = 0$ and $\eta_{\rm B} = 0.1$. The vertical dotted line indicates the spin-down timescale $t_{\rm p}$ corresponding to each rotation period (increasing thickness).* Right: *Corresponding photo-disintegration optical depth (black solid) and ratio of the acceleration timescale, $t_{\rm acc}$, to the photo-disintegration timescale, $t_{\rm photodis.}$, (red dashed) for am iron nucleus at Lorentz factor $\gamma_{\rm p,11}$. From Lemoine et al. (in prep.).*

Acceleration sites and curvature radiation

Various authors have discussed particle acceleration inside the light cylinder of pulsars and magnetars (see, e.g., Harding & Lai 2006 for a review). Possible sites include the polar cap region, just above the magnetic pole of the star (e.g., Sturrock 1971; Harding & Muslimov 2001, 2002), the "slot gap" region along the last open field line between the polar cap and the light cylinder (Arons 1983), and in the outer gap region close to the light cylinder (e.g., Cheng et al. 1986a,b; Bednarek & Protheroe 1997, 2002). Energy losses by curvature radiation are however likely to prevent the acceleration of particles to the highest energies both in the polar cap and the outer gap. One can calculate that, inside the light cylinder (see Eq. B.1), the Lorentz factor is limited by curvature radiation over a gap length $\xi R_{\rm L}$ to

$$\gamma_{\rm max} = \left(\frac{3\pi B R_\star^3 \xi^{-3}}{2ZecP}\right)^{1/4} \sim 1.1\times 10^8 Z_{26}^{-1/4}\xi^{-3/4}B_{13}^{1/4}P_{\rm i,-3}^{-1/4}R_{\star,6}^{3/4} \ . \quad (3.3)$$

Venkatesan et al. (1997) and Arons (2003) discussed that particles accelerated in the wind region with $r \gg R_{\rm L}$ with $R_{\rm L}$ the radius of the light cylinder, do not suffer curvature radiative losses. Indeed, outside the light cylinder, the dipole field structure cannot be causally maintained and the field becomes mostly azimuthal, with field lines spiraling outwards (Michel 1991).

Other energy losses during acceleration

Assuming that the injected ions are protons, the impact of photopion interactions can be evaluated in the standard $\Delta-$approximation, according to which interactions take place with photons of energy $\epsilon_{\gamma\pi} \sim 0.3\,{\rm GeV}/\gamma_{\rm p}$, with $\gamma_{\rm p}$ the proton Lorentz factor and cross-section $\sigma_{\gamma\pi} \sim 0.5\,{\rm mb}$. Particles will interact with the low-frequency photons produced by synchrotron cooling of the accelerated electrons (see Appendix A.4 for an estimate of the spectral energy distribution and density $\epsilon_\gamma {\rm d}n_\gamma/{\rm d}\epsilon_\gamma$ of these photons). The pion production optical depth, $\tau_{\gamma\pi} = R_{\rm PWN}\sigma_{\gamma\pi}\epsilon_\gamma {\rm d}n_\gamma/{\rm d}\epsilon_\gamma$ hence reads:

$$\tau_{\gamma\pi} \simeq 1.9\times 10^{-4}\,\gamma_{\rm p,11}^{1/2}\eta_B^{-1/4}P_{-3}^{-3/2} \times R_{\rm PWN,16.5}^{-1/4}B_{13}R_{\star,6}^3 I_{45}^{-1/4}\hat{t}^{-7/16} \ , \quad (3.4)$$

with $\hat{t} \equiv t/t_{\rm p}$, where $t_{\rm p}$ is the pulsar spin-down time defined in Eq. (A.3). Alternatively, one can compute the ratio of the acceleration timescale to pion production timescale:

$$\frac{t_{\rm acc}}{t_{\gamma\pi}} \simeq \frac{\gamma_p}{\gamma_{\rm conf}}\tau_{\gamma\pi} \ , \quad (3.5)$$

indicating that confinement, and not pion production, is a limiting factor for acceleration to the highest energies.

The same type of calculations can be performed for heavier nuclei, considering the Giant Dipole Resonance (GDR) as the main channel for energy losses on the background photons. The parameters for such interactions read: $\sigma_{A\gamma} \sim 8 \times 10^{-26}\, A_{56}\, \mathrm{cm}^{-2}$ for the cross-section, and $\epsilon_{\mathrm{GDR}} \sim 18\, A_{56}^{-0.21}\, \mathrm{MeV}/\gamma_{\mathrm{i}}$ (Stecker & Salamon 1999).

The left panel of figure 3.2 presents the time evolution of the iron nucleus confinement Lorentz factor γ_{conf}, dissipation Lorentz factors $\gamma_{\mathrm{diss.}}$, and limiting Lorentz factor from photo-disintegration interactions, for initial periods $P = 1 - 10\,\mathrm{ms}$.

The evolution over time of the photo-disintegration optical depth and the ratio of the acceleration to photodisintegration timescales, calculated at the at energy $\gamma_{\mathrm{p},11}$ are shown in the right panel of Fig. 3.2.

These figures demonstrate that ultra-high energy proton and iron acceleration close to the confinement limit is possible in PWNe with the parameters close to $B_{13} \sim 1$, $P_{-3} \sim 1 - 5\,\mathrm{ms}$, magnetization fraction $\eta_B \gtrsim 10^{-2}$.

3.2.3. Injected spectrum

Acceleration to high energies can only happen in the first stages of the life of the neutron star, typically within the spin-down timescale $t_{\mathrm{p}} \sim 3.1 \times 10^7\,\mathrm{s}\, I_{45} B_{13}^{-2} R_{\star,6}^{-6} P_{\mathrm{i},-3}^{2}$ (Eq. A.3).

In the following, we will place ourselves in a regime where the conversion efficiency of the wind electromagnetic into kinetic luminosity is high enough to achieve ultrahigh energies. Our results remain valid if we relax this assumption, at the cost of a softer injection spectrum that would be produced by the stochastic acceleration to reach the highest energies.

Taking into account the neutron-star spin down, one can apply Eq. (B.5) and write the cosmic rays energy at a given time t

$$E_{\mathrm{CR}}(t) \sim 7.3 \times 10^{19}\,\mathrm{eV}\, A_{56}\, \eta\, \kappa_4 I_{45} B_{13}^{-1} R_{\star,6}^{-3}\, {t_{7.5}}^{-1} \tag{3.6}$$

Channelling the Goldreich-Julian charge density into particles and taking into account the neutron-star spin down rate, we use Eq. (B.8) with $E = E_{\mathrm{CR}}(t)$, and write the cosmic-ray injection flux for each ion with mass and charge number (A, Z)

$$\frac{\mathrm{d}N_{\mathrm{CR}}}{\mathrm{d}E}(t) = \frac{9}{4} \frac{c^2 I \mathrm{f}_Z}{ZeBR_\star^3} E_{\mathrm{CR}}(t)^{-1} \left[1 + \frac{E_{\mathrm{CR}}(t)}{E_{\mathrm{g}}}\right]^{-1}, \tag{3.7}$$

where E_{g} is the critical gravitational energy defined in Eq. (B.9). We have noted f_Z the fraction of the Goldreich-Julian charge density in particles with charge Z injected into the pulsar wind. f_Z satisfies $\sum_Z \mathrm{f}_Z = 1$ and $\dot{N}_{\mathrm{GJ}} = \sum_Z \mathrm{f}_Z\, \dot{N}_{\mathrm{GJ}}(Z)$.

With the fiducial parameters of Eq. (3.2), this flux can be estimated as

$$\frac{\mathrm{d}N_{\mathrm{CR}}}{\mathrm{d}E} \sim 2.5 \times 10^{23}\, \mathrm{f}_Z\, I_{45} (A_{56}\, B_{13}\, E_{20})^{-1}\, \mathrm{eV}^{-1}\,. \tag{3.8}$$

This spectrum will be used in the following sections.

3.3. UHECR escape from supernova envelopes

Fang, K., Kotera, K., & Olinto, A. V. 2012, ApJ, 750, 118

Particles accelerated in the pulsar wind further need to escape from the pulsar wind nebula itself, and then from the surrounding young supernova envelope. We assume in this study that the supernova envelope is not totally disrupted by the wind, and that particles do not escape through a region punctured by a jet, like in a strongly magnetized proto-magnetar scenario discussed by Metzger et al. (2011a).

In supernova envelopes, magnetic fields are of order a few mG at most (see, e.g., Reynolds et al. 2012 for a review). The Larmor radius of the ions is thus much larger than the size of the envelope and their trajectories can be treated rectilinearly.

3.3.1. Supernova envelopes

As discussed for instance by Chevalier (2005), rotation-powered pulsars can originate in various types of core-collapse supernovæ: in Type II supernovæ resulting from red supergiant stars with most of their hydrogen envelope intact (SNIIP), or with most of their hydrogen lost (SNIIL and IIb), or in Type Ib or Type Ic supernovæ (SNIb/c) that stem from stars with all their hydrogen lost. Chevalier (2005) finds that, of the remnants with central rotation-powered pulsars, the pulsar properties do not appear to be related to the supernova category.

Within a few days after the explosion, the supernova enters a free expansion phase with velocity distribution $v = r/t$, that lasts several hundreds of years. A straightforward way to model the evolution of the density of the ejecta is to assume that the ejected mass M_{ej} will expand spherically in time with a mean velocity v_{ej} (see Eq. A.7) over a shell

of radius $R_{\rm SN} = v_{\rm ej} t$. The mean density over $R_{\rm SN}(t)$ can then be written:

$$\rho_{\rm SN}(t) = \frac{M_{\rm ej}}{(4/3)\pi v_{\rm ej}^3 t^3} \sim 2\times 10^{-16} M_{\rm ej,1}^{5/2} E_{\rm ej,52}^{-3/2} t_{7.5}^{-3}\ {\rm g\,cm^{-3}}\ . \quad (3.9)$$

The chemical composition of the ejecta after steady and explosive burning of supernova II-P, Ib, and Ic has been studied by a number of authors, e.g., Woosley & Weaver (1995); Arnett (1996); Woosley et al. (2002); Dessart et al. (2012). Core-collapse supernova progenitors have large abundances of Oxygen produced by Helium burning during the life of the massive star, and part of this Oxygen is burnt during the explosion, which produces Si, So, Mg, Ca and Ni. Note that in most cases, Hydrogen is the dominant component in the envelope to consider for the escape of cosmic rays, as studied in Fang et al. (2012). The effect of escape from SN envelopes which are not proton dominated is small once the summing over all pulsars is considered (Fang et al. 2013b).

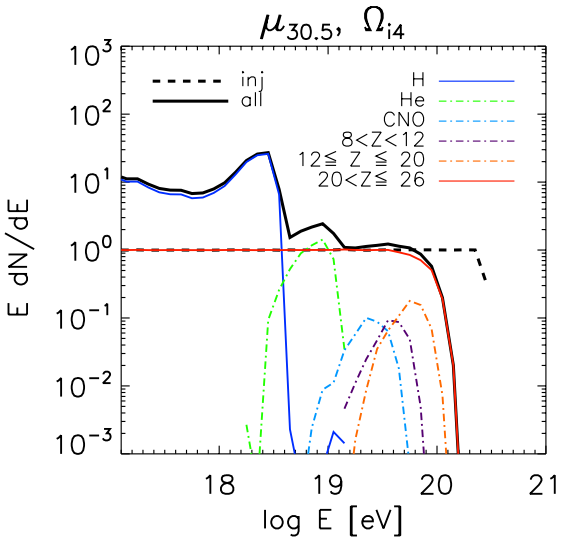

Figure 3.3.: *UHECR spectrum before (dash) and after (solid and dash dotted) escape from hydrogen supernova envelope with $M_{\rm ej,1}$ and $E_{\rm ej,52}$, with pure iron injection. The pulsar parameters are I_{45}, η_{-1}, $\Omega_{\rm i,4}$, and $\mu_{30.5}$. Different species as in the legend.*

3.3.2. Escaped fluxes

Successful escape of UHECRs from the envelope will occur if the supernova envelope crossing time $t_{\rm dyn} = [ct_{\rm spin}(E)]/v_{\rm ej}$ (see Eq. B.11 for the expression of the time $t_{\rm spin}(E)$ when particles of energy E are being accelerated) is shorter than the cooling time by hadronic

$$t_{Ap} = m_p (c\,\rho_{\rm SN}\sigma_{Np})^{-1} \sim 7.5\times 10^6\,{\rm s}\, A^{2/3}\, M_{\rm ej,1}^{-5/2} I_{45}^{3/2} P_{\rm i,-3}^{-3} t_{7.5}^3\ , \quad (3.10)$$

and photo-hadronic, $t_{A\gamma}$, interactions. Photo-hadronic interactions in the ejecta are not treated in this work. A discussion on the subject can be found in Appendix C.2, where we demonstrate that this process can be under-dominant for nuclei if the thermalization of the pulsar rotational energy in the ejecta is low.

Numerical Monte-Carlo results of the escaped spectrum, using the hadronic interaction code EPOS (Werner et al. 2006) are presented in Figure 3.3 for Hydrogen and Iron. The crossing of the supernova ejecta cuts exponentially the injection spectrum at:

$$E_{{\rm cut},p} \simeq 7\times 10^{19}\, Z_1 \eta I_{45} \mu_{30.5}^{-1} M_{\rm ej,1}^{-1} E_{\rm ej,52}^{1/2}\,{\rm eV} \quad (3.11)$$

$$E_{\rm cut,Fe} \simeq 1.2\times 10^{20} Z_{26} \eta I_{45} \mu_{30.5}^{-1} M_{\rm ej,1}^{-1} E_{\rm ej,52}^{1/2}{\rm eV}\ , \quad (3.12)$$

where we have assumed that hadronic interactions dominate with cross-sections $\sigma_p \approx 130\,{\rm mb}$ for pp interactions and $\sigma_{\rm Fe} \approx 1.25\,{\rm b}$ for $p-$Fe interactions (note that we used cross sections with full energy and composition dependence in the simulations).

In Figure 3.4, the contours represent $E_{\rm cut}$ reached after escaping hydrogen supernova envelopes with $M_{\rm ej,1}$ and $E_{\rm ej,52}$ for pulsars with dipole moment μ and initial angular velocity $\Omega_{\rm i}$. These calculations show that, at early times, when protons can be accelerated to energies $E > 10^{20}\,{\rm eV}$, the thickness of the supernova shell makes their escape difficult. In contrast, because of their higher charge, iron-peaked nuclei are accelerated to the highest energies at later times, when the envelope has become thin enough to allow their escape. Our successful producer of UHECRs is thus a pulsar born with millisecond periods with standard magnetic fields of $B \sim 10^{12-13}\,{\rm G}$. For higher fields, the spin-down of pulsars is too fast to enable the production of UHE particles before the SN ejecta has become optically thin.

Figure 3.3 shows that due to the production of secondary nucleons, the envelope crossing leads to a transition of composition from light to heavy elements at a few EeV, as observed by the Auger Observatory. The escape also results in a softer spectral slope than that initially injected, which allows a good fit to the observed UHECR spectrum.

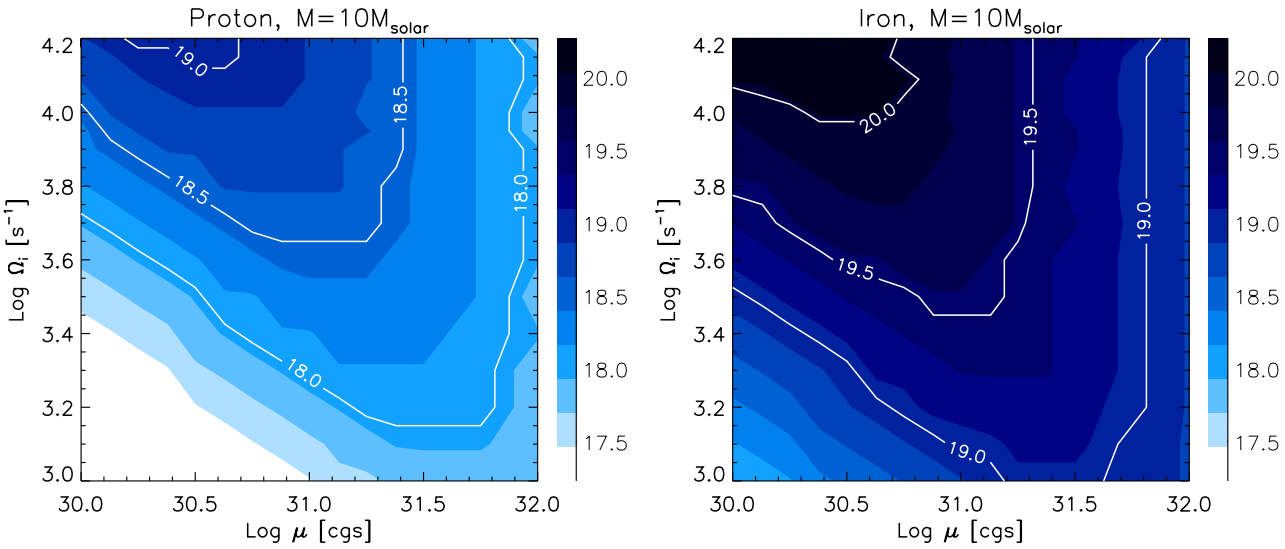

Figure 3.4.: *Cut-off energy ($E_{\rm cut,Z}$) contours in the parameter space ($\Omega_{\rm i}, \mu$) (pulsar initial rotation velocity, magnetic moment – see App. B.1) for a hydrogen supernova envelope with $M_{\rm ej,1}$ and $E_{\rm ej,52}$, and pulsar parameters I_{45} and η_{-1}. The solid lines refer to cut-off particle energies after the escape. Left: proton injection, right: iron injection. Notice that current neutron star models suggest an upper limit of rotational speed at $\Omega_{\rm i} \leq 10^{4.2}\,{\rm s}^{-1}$. Note also that $E_{\rm cut,Z}$ scales with $M_{\rm ej,1}^{-1} E_{\rm ej,52}^{1/2}$. From Fang et al. (2012).*

3.4. Comparison to the observed data

Fang, K., Kotera, K., & Olinto, A. V. 2013, J. Cos. and Astro. Phys., 3, 10

We have shown in the previous sections that fast spinning newborn pulsars could accelerate nuclei to the highest energies, and that their escape through the young supernova remnant softens their spectrum, decreases slightly their maximum energy, and generates secondary nuclei. Here we calculate the modifications due to the distribution of pulsar birth periods and the effect of propagation in the interstellar and intergalactic media on the combined spectrum of all pulsars. We show that the extragalactic pulsar population can explain the observed spectrum of ultrahigh energy cosmic rays and the trend towards heavier nuclei for energies above 10^{19} eV as reported by the Auger Observatory.

To fit these two observables (spectrum and composition) we allow the freedom to vary the fraction f_Z (see Eq. 3.7) of different elements that are accelerated in the pulsar wind divided into 3 groups: Hydrogen, Carbon group (CNO), and Iron.[3]

Pulsars contributing at ultrahigh energies cannot be Galactic, because of their expected anisotropy signature. A single source should lead to a noticeable spot of events in the sky at the highest energies, even for iron nuclei, unless the turbulent Galactic magnetic field is unreasonably strong. If many sources were contributing, they are also expected to trace the Galactic disk, but no such anisotropy has been observed in the UHECR data. The low birth rate of the pulsars born with millisecond periods (see Section 3.4.4), responsible in our model of UHECR production, can naturally account for the fact that no such pulsar is currently active in our Local Group.

[3]Because protons dominate the flux at ankle energies, and Helium nuclei are mostly dissociated into protons during the propagation, the injected protons can be mostly interchanged to Helium without affecting the spectrum significantly (Fang et al. 2013b).

3.4.1. Distribution of parameters in the extragalactic pulsar population

The source of UHECRs in our model are the rare, extremely fast spinning, young pulsars. The majority of pulsars were born spinning slower and therefore contribute to the flux of lower energy cosmic rays. According to Faucher-Giguère & Kaspi (2006), the distribution of pulsar birth spin periods, $f(P = 2\pi/\Omega)$, is normal, centered at 300 ms, with standard deviation of 150 ms. We assume that proto-pulsars cannot spin below the minimum spin period of a neutron star $P_{\rm min} \simeq 0.6\,{\rm ms}$ Haensel et al. (1999). The initial magnetic field follows a log-normal distribution $f(\mu)$ with $\langle \log(B/{\rm G}) \rangle \sim 12.65$ and $\sigma_{\log B} \sim 0.55$ (Faucher-Giguère & Kaspi 2006).

The total cosmic ray spectrum contributed by the

entire pulsar population is then

$$\frac{\mathrm{d}N}{\mathrm{d}E}(Z) = \int \frac{\mathrm{d}N_{\mathrm{esc}}}{\mathrm{d}E}(B,P,Z)\, f(B)\, f(P)\, dP\, dB\ , \tag{3.13}$$

where $\mathrm{d}N_{\mathrm{esc}}/\mathrm{d}E$ is the spectrum of cosmic rays after traversing the supernova envelope, assuming a particle injection in the wind following Eq. (3.7).

3.4.2. Propagation in the intergalactic medium

Cosmic rays injected by extragalactic pulsars travel through the Intergalactic Medium (IGM) on their way to Earth. The corresponding propagation effects also affect the observed spectrum and composition.

On average, the pulsar birth rate in the Galaxy is $\nu_{\mathrm{s}} \simeq 1/60\,\mathrm{yr}$ (Lorimer 2008b). For a galaxy density of $n_{\mathrm{gal}} \simeq 0.02\,\mathrm{Mpc}^{-3}$ and an energy loss time for cosmic rays with energy above $10^{19}\,\mathrm{eV}$ of $c\,T_{\mathrm{loss}} \sim 792\,\mathrm{Mpc}$ (Kotera & Olinto 2011), the average flux of cosmic rays from extragalactic sources can be estimated as:

$$\begin{aligned}\frac{\mathrm{d}N_{\mathrm{EG}}}{\mathrm{d}E\,\mathrm{d}t\,\mathrm{d}A\,\mathrm{d}\Omega} &= \frac{\mathrm{d}N}{\mathrm{d}E}\frac{1}{4\pi}\,c\,T_{\mathrm{loss}}\,n_{\mathrm{gal}}\,\nu_{\mathrm{s}}\,f_{\mathrm{s}} \qquad (3.14)\\ &\sim 7\times10^{-55}\,\frac{\mathrm{d}N}{\mathrm{d}E}\,f_{\mathrm{s}}\,\mathrm{eV}^{-1}\,\mathrm{m}^{-2}\,\mathrm{s}^{-1}\,\mathrm{sr}^{-1}\end{aligned}$$

where f_{s} is an overall factor used to fit the model prediction to the measured UHECR flux. In our scenario, it can be interpreted as the fraction of total flux of pulsar births required to account for the observed flux of UHECRs out of the total pulsar birth rate. $f_{\mathrm{s}} < 1$ can be due to efficiency factors such as variations in the core-collapse geometry, poorer injection efficiency, or a lower hadronic density in the pulsar wind than the Goldreich-Julian density.

In order to estimate the observed spectrum of UHECRs, after their propagation through the extragalactic medium, we rescaled the simulation output of Kotera et al. (2010b) from 10^{16} eV up to the maximum acceleration energy, E_{max} by the injected spectrum of pulsars. The effect of the GZK interactions of UHECRs with the cosmic microwave background as well as other cosmic photon backgrounds is included in these calculations. Note however that in the pulsar scenario, the GZK effect is secondary to the effect of E_{max} which is set by the fastest spin rate that neutron stars can reach.

The UHECR spectrum and composition ratios for a given pulsar, after escape through the surrounding supernova ejecta, were calculated in Fang et al. (2012). At the highest energies, the spectrum is mostly determined by the superposition of exponential cutoffs up to E_{cut}, coming from the effect of escaping through the supernova ejecta. In order to account for the whole range of pulsar spins and magnetic fields, we ran 19×19 simulations of sets of $(P, \log B)$, and integrated the obtained spectra over the overall pulsar population following Eq. (3.13).

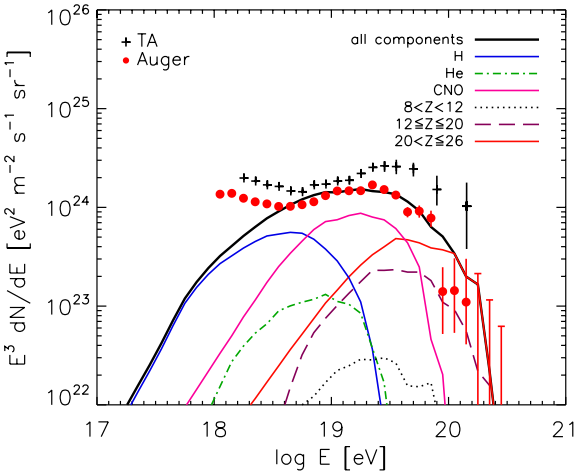

Figure 3.5.: *Propagated energy spectrum of UHECRs from newly born pulsar population with* $\log B$ *and* P *normally distributed, and wind acceleration efficiency* $\eta = 0.3$. *Simulation results were normalized to the Auger data at* 10^{19} eV *with* $f_{\mathrm{s}} \simeq 0.05$. *The spectrum of each group of propagated nuclei are shown as in the legend box. A mixed composition of* $\mathrm{f_H} = 0.5$, $\mathrm{f_{CNO}} = 0.3$ *and* $\mathrm{f_{Fe}} = 0.2$ *was injected. The source emissivity is assumed to be constant over time.*

3.4.3. Overall spectrum and composition

Figure 3.5 shows the propagated energy spectrum of cosmic rays from EG pulsars. We assume the sources to be uniformly distributed in space, normally distributed in $\log \mu$ and P as in Equation 3.13, with pulsar wind acceleration efficiency $\eta = 0.3$, and the source emissivity to be constant over time. (For a discussion on the influence of the source evolution model on the UHECR spectrum, see Kotera et al. 2010b; Fang et al. 2013b.) The overall normalization factor is set to $f_{\mathrm{s}} \sim 0.05$, and the injected composition $\mathrm{f_H} = 0.5$, $\mathrm{f_{CNO}} = 0.3$ and $\mathrm{f_{Fe}} = 0.2$. These composition ratios were chosen to fit the Auger spectrum (Abreu et al. 2011) and composition (Abraham et al. 2010a; Abreu et al. 2011).

The mean atmospheric depth $\langle X_{\mathrm{max}}\rangle$ and its fluctuations, $\mathrm{RMS}(\langle X_{\mathrm{max}}\rangle)$ of our model compared with Auger measurements (Abraham et al. 2010a) are presented in Fig. 3.6. Four hadronic interaction mod-

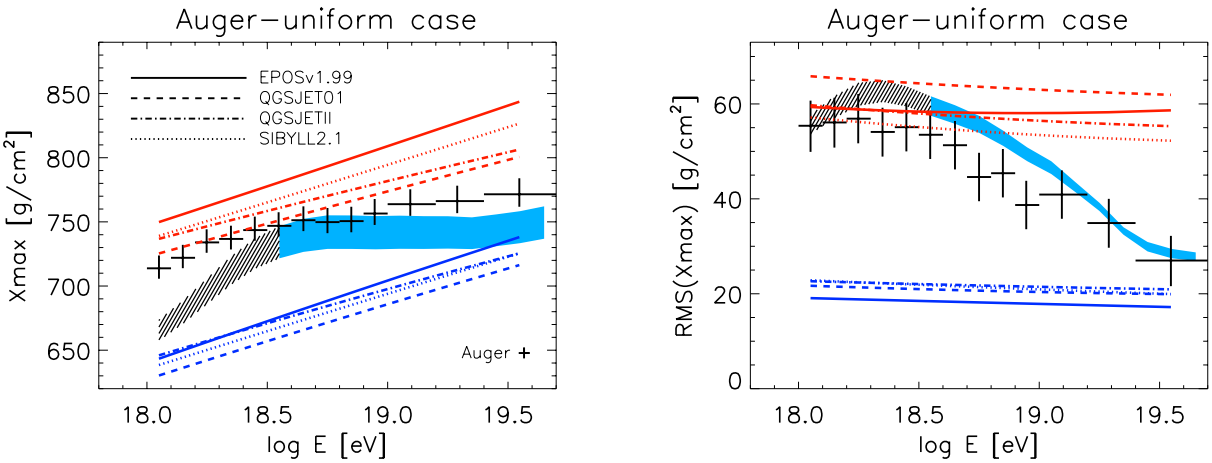

Figure 3.6.: *Composition estimators $\langle X_{\max}\rangle$ (left) and RMS($X_{\max}$) (right) of the Auger data (Abraham et al. 2010a; Abreu et al. 2011) (black crosses) and simulation results of the Auger-uniform case as in Fig 3.5 (blue shaded region is for where pulsars contribute more than 80% to the total flux, hashed region when they contribute less). Flux from both Galactic and extragalactic pulsars are taken into account. Four interaction models, EPOSv1.99 (Pierog & Werner 2008), QGSJET01 (Kalmykov et al. 1997), QGSJETII (Ostapchenko 2008) and SIBYLL2.1 (Ahn et al. 2009) were used to estimate the range of $\langle X_{\max}\rangle$ and RMS($X_{\max}$) as listed in the legend box. The red and dark blue lines correspond to 100% P and 100% Fe.*

els EPOSv1.99 (Pierog & Werner 2008), QGSJET01 (Kalmykov et al. 1997), QGSJETII (Ostapchenko 2008) and SIBYLL2.1 (Ahn et al. 2009) were used in this calculation, which gives the range of the blue shaded region. Our estimates include the contribution of Galactic pulsars, as calculated in the following section.

Our results follow well the spectrum and the trend of a transition from light to heavy elements as measured by the Auger Observatory. In the uniform source evolution case presented in this figure, pulsars become an underdominant source below $E \sim 10^{18.5}$ eV, as the extragalactic contribution cuts off at the ankle, and the Galactic pulsar population provides only a fraction of the total flux below. As a result, the composition below the ankle appears heavier than measured, and another light component is needed (which raises some questions about the origin of this other component as discussed in Fang et al. 2013b). We present in Fang et al. (2013b) other possible source evolution cases, and fits to the TA data. Under our chosen assumptions, it is difficult to fit a constant light composition as claimed to be measured by TA, and our predictions are a bit heavier than the Auger composition. The spectral fit becomes also less good for a source evolution following the star formation rate (SFR). The magnetic horizon effect (Aloisio & Berezinsky 2005; Lemoine 2005; Kotera & Lemoine 2008a; Globus et al. 2008) would harden the extragalactic spectrum around the ankle region, and may enable a better spectral fit with the star formation rate scenario. It is also possible that the extragalactic pulsar population that produces UHECRs has a biased evolution (see Fang et al. 2012) that can be weaker compared to the classical star formation rate. One would then obtain a better fit to the spectrum, as in the uniform source evolution case, but, to the expense of a good fit to the composition around the ankle region.

One probe of this scenario would be a sharp cut-off of the energy spectrum at energies above $E_{\rm cut}$. A mild recovery is indeed expected if the maximum acceleration energy were $E > 10^{20.5}$ eV, as the observed cut-off in the spectrum would then be due to the GZK effect.

3.4.4. Required source density

Using the pulsar parameter distribution by Faucher-Giguère & Kaspi (2006) and our numerically computed fluxes, we have estimated that the normalization factor $f_{\rm s} \sim 0.05$, which leaves reasonable room for poorer injection efficiencies, and invalid geometries of pulsars to accelerate particles. Assuming the gaussian distribution of pulsar parameters proposed by Faucher-Giguère & Kaspi (2006), less than 0.3% of the total population are pulsars born with periods less than 6 ms, i.e., can accelerate particles to above 10^{19} eV (these estimates can be modulated by the injection efficiencies).

More generally, one can also estimate this efficiency rate as follows (Lemoine et al. in prep.). The energy output into cosmic rays above 10^{19} eV must match $\dot{\epsilon} \simeq 0.5 \times 10^{44}\,\mathrm{ergs/Mpc^3/yr}$ once it is folded over the population of sources Katz et al. (2009).

Over t_p, the pulsar injects into ions

$$\mathcal{E}_\mathrm{i} = \eta_\mathrm{i}\, L_\mathrm{w}\, t_\mathrm{p} = \frac{(1-\eta_B)x_\mathrm{i}}{(1+x_\mathrm{i})} L_\mathrm{p} t_\mathrm{p}\ . \tag{3.15}$$

Assuming that these millisecond pulsar wind nebulae constitute a fraction η_ms of the total isolated pulsar birth rate $\nu_\mathrm{s} n_\mathrm{gal} \simeq 1.2 \times 10^{-4}\,\mathrm{Mpc^{-3}yr^{-1}}$ (van den Bergh & Tammann 1991), the normalization to the flux of UHECRs implies

$$\eta_\mathrm{ms} \sim 6 \times 10^{-4} q_\mathrm{i}\, x_\mathrm{i}^{-1}\, L_{\mathrm{p},45}^{-1} t_{\mathrm{p},7.5}^{-1}\ , \tag{3.16}$$

assuming here $x_\mathrm{i} \lesssim 1$, i.e. $\kappa \gtrsim 10^3$, and $1-\eta_\mathrm{B} \sim 1$. Recall that $x_\mathrm{i} \simeq 0.09(A_\mathrm{i}/Z_\mathrm{i})\kappa_4^{-1}$. We omit the prefactor which relates the energy output above 10^{19} eV to the total ion energy; this prefactor is of order unity, because ions are injected with a very large minimum Lorentz factor $\sim \gamma_\mathrm{diss.}$ in this case, and Fermi acceleration provides near equal power per decade. This energy budget thus seems modest. The prefactor $q_\mathrm{i} \equiv (s-2)/\left\{1-[\gamma_\mathrm{max}(t_\mathrm{p})/\gamma_\mathrm{diss.}(t_\mathrm{p})]^{2-s}\right\}$ for an injection spectral index s, accounts for the difference in normalization induced by the lower cosmic-ray injection energy limit. Note that a normalization at 10^{18} eV with $s \sim 2$ would require $\sim 1\%$ of the total supernova rate.

The difference between the factors η_ms and f_s is that the former includes consistently the information on the injection efficiency, whereas the latter contains the information on the source population parameters, following studies such as Faucher-Giguère & Kaspi (2006).

3.4.5. Distribution of events in the sky

The radio, X-ray and gamma-ray signals of rotation-powered pulsars and magnetars are too weak to allow their detection beyond our Local Group. For this reason, a direct spatial coincidence between a neutron star and UHECR arrival directions is not expected to be observed, if the source is not born inside our Local Group.

Nevertheless, the distribution of UHECR events could follow the large scale structures, where neutron stars should be concentrated. In particular, these objects should be frequently found in star forming galaxies. Such distributions would be apparent only if the deflections experienced by particles in the Galactic and intergalactic magnetic fields are small. Oikonomou et al. (in prep.) investigates under which circumstances the astrophysical distribution of sources can be distinguished from one another. A sizable fraction of light elements $\gtrsim 30\%$ among the total composition is usually required. Overall anisotropy signals could be detected even in the case of purely heavy compositions at the highest energies (d'Orfeuil et al. 2014).

Neutron stars can be considered as transient UHECR sources. Cosmic rays with energy above $E_\mathrm{GZK} \sim 6 \times 10^{19}$ eV can indeed only be produced during the first $\Delta t_\mathrm{s} \sim 4\, Z_{26}\eta_1 I_{45}\mu_{30.5}^{-1}$ yr after the birth of the neutron star.

This implies that if secondary messengers such as neutrinos, gamma-rays, or gravitational waves were produced at the same time as UHECRs, they would not be observed in temporal coincidence with the latter. The time delay experienced by UHECRs in the intergalactic magnetic field is indeed of order $\sim 10^4$ yrs for one degree deflection over 100 Mpc, which is much longer than the duration of the UHECR production.

Transient sources could lead to bursts of events in the sky if the number of event per source is important, and the arrival times of particles is not diluted by the dispersion induced by magnetic deflections (Kalli et al. 2011b; Fang et al. 2012). A direct identification of the source could be possible if a pulsar was born inside our Galaxy, or close enough to allow X-ray or gamma-ray observations. The dispersion of arrival times inside our Galaxy σ_Gal reads:

$$\sigma_\mathrm{Gal} \sim 2.5\, Z^2 \left(\frac{l}{10\,\mathrm{kpc}}\right)^2 \left(\frac{B_\mathrm{turb}}{4\,\mu\mathrm{G}}\right)^2 \times \left(\frac{\lambda_\mathrm{turb}}{50\,\mathrm{pc}}\right)\left(\frac{E}{E_\mathrm{GZK}}\right)^{-2} \mathrm{yr}. \tag{3.17}$$

Here we noted B_turb and λ_turb the turbulent magnetic field intensity and coherence length respectively, and l the distance of the source. The time delay δt_Gal experienced by particles due to the turbulent Galactic magnetic field is typically much larger than σ_Gal, due to the additional deflection due to the regular magnetic field component.

For proton injection and a weak regular magnetic field component, this implies that if such an event were to occur, a burst in UHECRs with a typical rise and decay timescale of a fraction of year would be observed in the sky, from a time δt_Gal after the onset of the explosion that triggered the birth of the fast-spinning neutron star. In this case, secondary messengers propagating rectilinearly would also ar-

rive at a time $\delta t_{\rm Gal}$ before UHECRs.

For iron nuclei injection, the highest energy elements come out of the envelope as heavy nuclei. These should reach the Earth after a time delay of $\delta t_{\rm Gal} \gtrsim 1750\,{\rm yrs}\,/l^2_{10\,{\rm kpc}}$. For very close-by sources (e.g., at 2 kpc), $\delta t_{\rm Gal}$ could be of order the experimental timescale $T_{\rm exp}$, leading to a sudden increase in the detection of ultrahigh energy events (about $N_{\rm ev} \sim 4 \times 10^{12}$ over $\delta t_{\rm Gal} \gtrsim 70\,{\rm yrs}$, for a source at 2 kpc).

Particles at energies $E < E_{\rm GZK}$ should arrive with more consequent time delays, so potentially from young rotation-powered pulsars that are detected nowadays. The dispersion in time should however be as consequent, and such events should not be detected as bursts, but only as continuously arriving particles. No spatial clustering from such sources is expected either, as the deflections experienced by particles at these low energies should be large.

If EeV or higher energy neutrons were produced by these objects, by interactions of accelerated nuclei in the envelope for example, they would propagate rectilinearly and would appear as point sources. However, nearly no time delay between the detection of the birth of the neutron star and the arrival of the particles is expected. Spatial correlations between pulsar positions and neutron events are thus expected only if a new birth actually occurs in the Galaxy.

3.5. Conclusions

We have studied the injection, acceleration and escape of UHECRs from newly-born pulsars. Our results show that protons and light elements at the highest energies can only traverse very dilute the envelopes. For pulsars born with millisecond periods and mild magnetic fields $B \sim 10^{12-13}$ G, embedded in standard supernovæ, iron nuclei are able to escape from the envelope with energy above 10^{20} eV. The propagated spectrum integrated over the whole extragalactic pulsar population fits the observed UHECR flux and displays a transition from light to heavy composition at a few EeV, matching the recent Auger data. We have shown that the required source birth rate and injection efficiencies are low enough to allow a comfortable margin to the model.

We will discuss the contribution of the Galactic pulsar population on the whole cosmic-ray spectrum in the next chapter, and will demonstrate that this counterpart could successfully bridge the gap around the ankle region between a supernova remnant component and the extragalactic component at UHE. Such a feature is also appealing in view of the challenge that the community is facing to find natural accelerators that can produce cosmic-rays with the adequate properties in that energy range.

Source models that enable such a good and consistent fit to the overall measured data are rare in the literature. We have discussed that the two most popular candidate sources, GRBs and AGN, both encounter major energetics issues: GRBs might be too rare to supply the necessary amount of total energy to UHECRs, and only the most powerful, hence rare, AGN are capable of accelerating particles to the highest energies (see, e.g., Lemoine & Waxman 2009). However, these rare AGN should lead to anisotropy signatures that are not compatible with the observed low signal level. Besides, both sources are believed to be hardly able to produce ultrahigh energy heavy nuclei. On the other hand, though their scenario is scarcely discussed in the literature, young pulsars born with millisecond periods are a promising candidate.

In the iron injection case, the birth of such an object within our Galaxy would be noticeable in the number of detected events, only for very close-by sources (at $\sim 2\,$kpc). Such a source could lead to a distinct increase of the observed UHECR events starting $\delta t_{\rm Gal} \gtrsim 70\,{\rm yrs} \times (l/2\,{\rm kpc})$ after the birth (for a source located at l, with parameters chosen in Eq. 3.17), and that would last for $\delta t_{\rm Gal}$. The birth rate of neutron stars satisfying our criteria inside our Galaxy would however be as low as $\sim 5 \times 10^{-7}\,{\rm yr}^{-1}$. No such pulsar should be operating now, as a strong anisotropy signal would be observed otherwise.

The non-recovery of the energy spectrum above $E_{\rm cut,Fe} \sim 10^{20.5}\,$eV, or the precise measurement of the cosmic ray composition at high energies would also be smoking-guns for this model. Large exposure instruments such as JEM-EUSO would allow to make such measurements and probe this scenario. Other multi-messenger signatures are expected, in particular in neutrinos, as discussed in Chapter 5.

Note that various points still need to be carefully addressed in this scenario, in particular about the acceleration mechanism. A detailed study of acceleration in the wind would require a precise modeling of its composition and structure. Our knowledge on these matters is currently limited and subject to controversies (Kirk et al. 2009). We discuss some possibilities to examine these issues using cosmic-ray signatures in Chapter 6.

4. Galactic pulsars and the ankle region

Fang, K., Kotera, K., & Olinto, A. V. 2013,
J. Cos. and Astro. Phys., 3, 10

The highest energy cosmic rays are likely to originate in extragalactic sources, given the strength of Galactic magnetic fields and the lack of correlations with the Galactic plane. Low energy cosmic rays are easily created and contained in the Galaxy, so a transition region should occur at some intermediate energy. "A hypothesis blessed by long tradition is that" Galactic cosmic rays end below 10 EeV "and above that a different source is active (most plausibly in the nearby supercluster of galaxies)" quoting Hillas (1984). Modern measurements of the spectrum place a plausible transition region around the ankle at a few EeV. However, the ankle can also be interpreted as the product of propagation losses due to pair production (Berezinsky & Grigorieva 1988; Berezinsky et al. 2006) in proton dominated scenarios allowing for a transition at lower energies.

The presence of a source in the Galaxy contributing at the ankle energy would induce a signature in the large-scale anisotropy of the arrival directions of cosmic rays. Measurements with Auger and TA are already constraining the Galactic-extragalactic transition energy and models of the Galactic magnetic field (Giacinti et al. 2011; Pierre Auger Collaboration et al. 2012; Telescope Array et al. 2013).

The knee in the cosmic ray spectrum is likely to signal the maximum acceleration energy $E_{\max}$ for light nuclei of dominant Galactic sources and/or the maximum containment energy for light nuclei in the Galactic magnetic field. The same effect for heavier nuclei may cause the softer spectrum above the knee (see, e.g., Lemoine 2005; Hillas 2006). Extragalactic sources producing spectra harder than $s = 3$ can overtake the decaying Galactic flux around the ankle. Recent studies of a transition at the ankle which fit the observed spectrum and the composition trends in this energy region are discussed in Allard et al. (2005) where different models are contrasted. Models based on proton primaries with a hard spectrum (Wibig & Wolfendale 2004), on a mixed composition with proportions similar to the Galactic mix, or even on a composition dominated by heavy nuclei (Allard et al. 2007) fit well the UHECR spectrum and composition

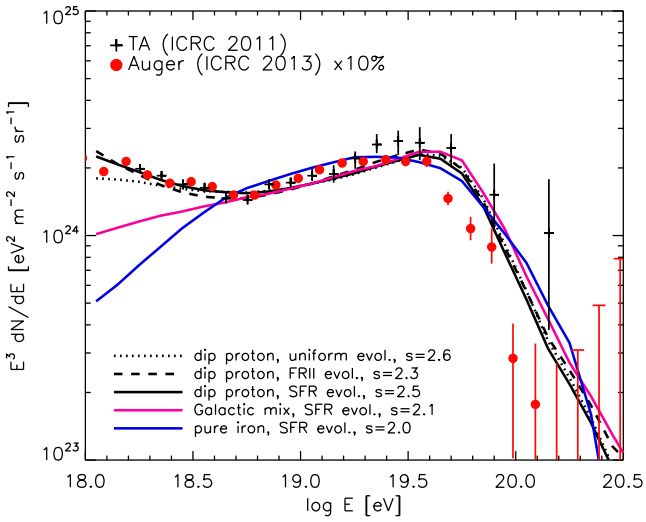

Figure 4.1.: *Spectrum of UHECRs multiplied by E^3 observed by TA (Jui 2011) and Auger (The Pierre Auger Collaboration et al. 2013). Overlaid are simulated spectra obtained for different models of the Galactic to extragalactic transition and different injected chemical compositions and spectral indices, s. The Auger spectrum has been re-scaled of 10% to account for the energy calibration changes that were reported recently by the collaboration.*

data around the ankle. In Figure 4.1, we show two examples of the so-called "ankle transition models": one with source injection $s = 2.1$, source composition similar to the Galactic mixture, and source evolution that follows the SFR; and a second model with similar source evolution and $s = 2$, but a pure iron composition injected. Both models fit well the UHECR spectrum but predict different compositions throughout this energy range.

Ankle transition models work well for UHECR scenarios, but they were thought to challenge models for the origin of Galactic cosmic rays. The requirement that Galactic sources reach energies close to the ankle strained traditional models where acceleration in supernova remnants (SNRs) was expected to fade around 1 PeV (Lagage & Cesarsky 1983). A modification to the traditional SNR scenario, such

as magnetic field amplification in SN shocks (Bell & Lucek 2001), or a different progenitors such as Wolf-Rayet star winds (Biermann & Cassinelli 1993), and trans-relativistic supernovae (Budnik et al. 2008) may explain the energy gap from PeV to EeV. Taking into account magnetic field amplification and Alfvenic drift in shocks of Type IIb SNRs, Ptuskin et al. (2010) find that Galactic cosmic ray iron can reach $E_{\max} \sim 5$ EeV, allowing extragalactic cosmic rays to begin to dominate above the ankle.

The possibility that the ankle is due to pair-production losses during the propagation of extragalactic protons (Berezinsky & Grigorieva 1988) has motivated an alternative model for the Galactic to extragalactic transition, called "dip models" (Berezinsky et al. 2006). The energy of the predicted dip is close to the observed ankle and a good fit to the spectrum over a large energy range is reached with a softer injection index as the dip proton models shown in Figure 4.1. This option relaxes the need for Galactic cosmic rays to reach close to EeV energies, however it needs to be tuned to avoid strong (unobserved) spectral features between the knee and the ankle. Detailed models where the lower energy behavior of the extragalactic component blends smoothly with the Galactic cosmic rays have been developed using minimum energy and magnetic effects (Lemoine 2005; Aloisio & Berezinsky 2005; Hillas 2006; Kotera & Lemoine 2008a; Globus et al. 2008). In some of these models a feature is produced around the "second knee" which may be observed around 0.5 EeV. The dip model can fit the observed spectrum if the injection is proton dominated (Berezinsky et al. 2005; Allard et al. 2007) or with at most a primordial proton to helium mix (Hillas 2006), which gives a clear path for distinguishing it from mixed composition models. A proton dominated flux below the ankle region is a necessary condition for this model to be verified.

Clarifying the structure of the transition region is crucial for reaching a coherent picture of the origin of Galactic and extragalactic cosmic rays. This will require accurate spectrum and composition measurements from the knee to the ankle and beyond. KASCADE-Grande (Apel et al. 2013) has made great progress above the knee, as well as IceTop most recently (Abbasi et al. 2013), while UHECR projects have started to lower their energy threshold such as the Auger Observatory enhancements (The Pierre Auger Collaboration: J. Abraham et al. 2009; Klages & Pierre Auger Collaboration 2012): HEAT (High Elevation Auger Telescopes) and AMIGA (Auger Muons and Infill for the Ground Array); and the Telescope Array Low Energy Extension (TALE) proposal. Having the same system covering a large range in energy will help control systematic offsets that degrade the accuracy of the needed precision. In addition, a strong multi-wavelength program has shown that magnetic field amplification occur in SNRs and Galactic sources can reach higher energies than previously believed. Finally, models of hadronic interactions will benefit by the energy reach of the LHC which can probe hadronic interactions at energies higher than the knee and help constrain composition indicators between the knee and the ankle.

In what follows, we demonstrate that the contribution of extragalactic pulsar births to the ultrahigh energy cosmic ray spectrum as modeled in Chapter 3 naturally gives rise to a contribution to very high energy cosmic rays (VHECRs) between 10^{16} and 10^{18} eV by Galactic pulsar births. The required injected composition to fit the observed spectrum depends on the absolute energy scale, which is uncertain, differing between Auger Observatory and Telescope Array. The contribution of Galactic pulsar births can bridge the gap between predictions for cosmic ray acceleration in supernova remnants and the observed spectrum just below the ankle, depending on the composition of the cosmic rays that escape the supernova remnant and the diffusion behavior of VHECRs in the Galaxy.

4.1. Propagation from Galactic sources

The contribution of young pulsars to the Galactic cosmic ray flux is related to the extragalactic contribution through the distribution of birth parameters. Assuming that cosmic rays injected in the interstellar medium (ISM) by Galactic pulsars have the same composition as those from extragalactic pulsars, we can calculate the contribution of both Galactic and extragalactic pulsars. The end of the Galactic spectrum is highly dependent on Galactic diffusion parameters and the history of the most recent pulsar births in the Galaxy (such that the flux in the VHE region varies over long time scales). However, we will see that the differences in the UHECR data, such as the different absolute energy scales of the Auger and TA observatories, give rise to significant changes in the predictions for the Galactic component. The Auger fit implies Galactic pulsars as the main con-

tributors to VHECRs from 10^{18} eV, while with the TA fit, they start dominating from $10^{17.5}$ eV (see Fig. 4.2).

Cosmic rays injected by Galactic pulsars travel through the ISM on their way to Earth. The corresponding propagation effects affect the observed spectrum and composition. For the propagation of cosmic rays accelerated by Galactic pulsars, we model the turbulent Galactic magnetic field as a cylindrical halo of radius $R_{\rm Gal} = 15\,$kpc, of height above (or below) the Galactic plane typically $H \sim 2-8\,$kpc Mao et al. (2012), of coherence length $l_{\rm c} = 10-100\,$pc and strength $B = 3\,\mu$G (see Han (2008) and references therein). The Larmor radius of a particle reads $r_{\rm L} = 13.8\,E_{18}\,Z_{26}^{-1}\,(B/3\,\mu{\rm G})^{-1}\,$pc.

The flux of cosmic rays accelerated by Galactic pulsars can then be calculated as

$$\frac{{\rm d}N_{\rm Gal}}{{\rm d}E\,{\rm d}t\,{\rm d}A\,{\rm d}\Omega} = \frac{{\rm d}N_{\rm esc}}{{\rm d}E}\,\frac{1}{4\pi}\,\frac{c\,\delta t_{\rm obs}}{V_{\rm Gal}}\,\nu_{\rm s}\,f_{\rm s} \times \left(1 - e^{-\delta t_{\rm obs}/\delta t_{\rm birth}}\right), \quad (4.1)$$

where $f_{\rm s}$ is the same scale factor introduced for the extragalactic component (Eq. 3.14), $\nu_{\rm s}$ is the average birth rate of pulsars in our Galaxy, and $V_{\rm Gal} = 2\pi\,H R_{\rm Gal}^2$ is the volume of the Milky Way. The average number of sources in the Galaxy that contributes to the observed spectrum at a given energy E is $N_{\rm s}(E) = \delta t_{\rm obs}(E)/\delta t_{\rm birth}(E)$, where $\delta t_{\rm obs}(E)$ is the timescale over which a source can can contribute to the observable cosmic rays of energy E, and $\delta t_{\rm birth}(E)^{-1}$ is the birth rate of Galactic sources that can produce particles of energy E. Following a Poisson distribution, the probability that currently at least one source is contributing in the Galaxy is $(1 - e^{-\delta t_{\rm obs}/\delta t_{\rm birth}})$.

If the scattering length of the particle (distance over which its deflection angle becomes $\delta\theta \sim 1$) is shorter than the height of the Galaxy, the propagation will be mostly diffusive, and the source observation time is equivalent to the particle escape time from the Galaxy: $\delta t_{\rm obs} = \tau_{\rm esc}$. At energies above the knee ($\sim 10^{15}$ eV), which is the main concern of this paper, nuclei spallation is negligible (Blasi & Amato 2012a) and the nuclei escape time can simply be estimated with the Leaky box model

$$\tau_{\rm esc}(E, Z, l_{\rm c}) = \frac{H^2}{2D}\,, \quad (4.2)$$

where D is the diffusion coefficient in the Galactic magnetic field, that can be estimated empirically as in Equation (A2) of Kotera & Lemoine (2008a)

$$D(E, Z, l_{\rm c}) \sim D_0\,r_{\rm L}\,c\left[\frac{r_{\rm L}}{l_{\rm c}} + \alpha\left(\frac{r_{\rm L}}{l_{\rm c}}\right)^{-2/3}\right]. \quad (4.3)$$

The coefficient α depends on the turbulence and structure of the Galactic magnetic field. The normalization D_0 is set at energies where particles are in the Kolmogorov regime ($r_{\rm L} \ll l_{\rm c}$), using measurements of the boron to carbon ratio in our Galaxy. We follow the estimates of Blasi & Amato (2012a):

$$D(R) = 1.33\times 10^{28}\,D_0\,H_{\rm kpc}\left(\frac{R}{3\,{\rm GV}}\right)^{1/3}\,{\rm cm^2 s^{-1}}\,, \quad (4.4)$$

where $H_{\rm kpc} = H/1\,$kpc, and the particle rigidity $R \equiv E/Z$. Notice that in the diffusive regime, the diffusion coefficient scales as $E^{-\delta}$, with $\delta = 1/3$, a value which seems to be favored by observations, e.g., Blasi & Amato (2012a) (see also Table 2.1 for values inferred for cosmic rays below the knee). A larger value of δ would imply a faster escape out of the Galaxy of particles at very high energies. For example, $\delta = 0.6$ would imply that all particles above 4×10^{15} GV travel rectilinearly, which is inconsistent with anisotropy measurements (Kifune et al. 1986; Aglietta et al. 2003; Amenomori et al. 2005).

For scattering lengths larger than H, the propagation is quasi-rectilinear. In principle, the observation time $\delta t_{\rm obs}$ is then equivalent to the dispersion of particle arrival times $\sigma_t = D_{\rm s}\,\delta\theta^2/(4c)$, where $D_{\rm s}$ is a typical source distance (Alcock & Hatchett 1978; Harari et al. 2002; Kotera & Lemoine 2008b). The transition from a totally diffusive regime to a quasi-rectilinear regime can be modeled using Eq. 4.3 with $\alpha = 1$. For reasonable assumptions on the structure of the magnetic field, one can then assume $\delta t_{\rm obs} = \sigma_{\rm t} \sim \tau_{\rm esc}$ at high rigidities.

At large E (thus large $r_{\rm L}$), $\delta t_{\rm birth}$ is very large because of the rarity of the corresponding sources, which have to be highly magnetized fast rotating pulsars. This effect combined with the fast escape time produce a cut-off in the cosmic-ray flux above $\sim 10^{17}$ eV.

4.2. Very High Energy cosmic-ray flux from pulsars

Figure 4.2 show the results for a fit to the Auger data with a uniform source evolution with (top) the total energy spectrum and the spectrum decomposed into three components (Hydrogen, intermediate, and Iron) as reported by KASCADE (Antoni et al. 2003),

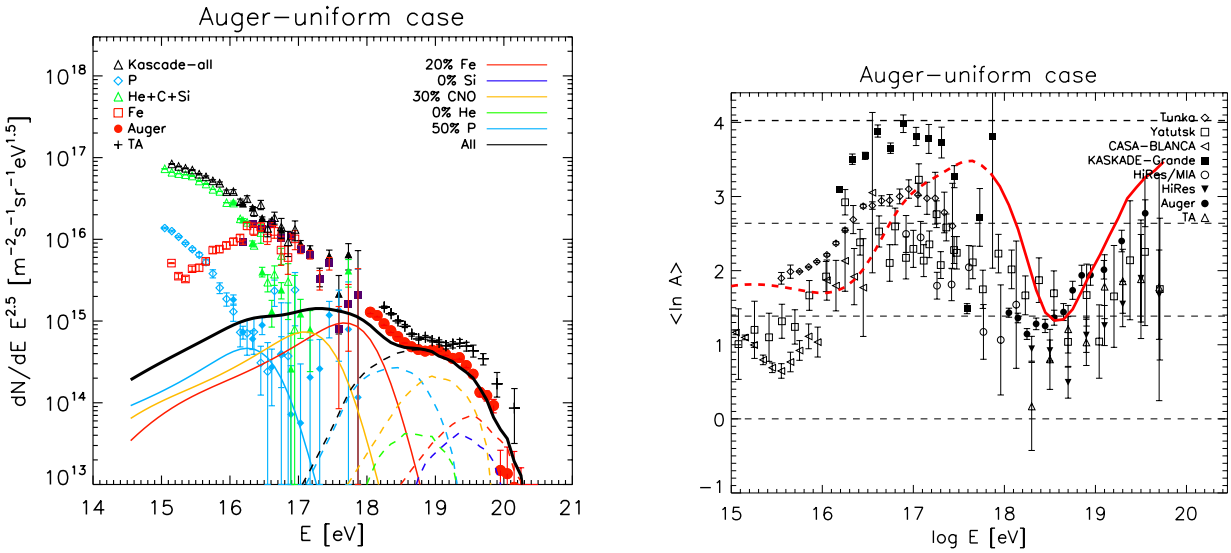

Figure 4.2.: (Left) *Cosmic ray flux measurements by KASCADE-Grande (Apel et al. 2011), Auger (Abreu et al. 2011) and TA (Jui 2011) compared with pulsar model predictions. The total spectrum in solid black sums up extragalactic (dash) and Galactic (solid) components. For a uniform source emissivity evolution as in Fig 3.5. Pulsar and propagation parameters: wind acceleration coefficient* $\eta = 0.3$*, Galactic magnetic field coherence length* $l_c = 20\,\mathrm{pc}$*, magnetic halo height* $H = 2\,\mathrm{kpc}$*.* (Right) *Average logarithmic mass of cosmic ray derived from* $X_{\max}$ *measurements from (Kampert & Unger 2012) with data from Tunka (Budnev et al. 2009), Yakutsk (Knurenko & Sabourov 2010, 2011), CASA-BLANCA Fowler et al. (2001), HiRes/MIA (Abu-Zayyad et al. 2001), HiRes (Abbasi et al. 2010), KASCADE-Grande (Apel et al. 2011), Auger (Abreu et al. 2011) and TA (Jui 2011) for hadronic interaction model EPOS v1.99 (Pierog & Werner 2008) compare with simulation predictions (red lines). Dashed lines indicate the energy range where pulsars contribute less than* 80% *to the total flux (see left panel) and other sources also contribute.*

KASCADE-Grande (Apel et al. 2011) and the Auger spectrum. The extragalactic spectra (in dash lines) in Fig. 4.2 are the same as those in Fig. 3.5.

The Galactic spectrum of each element group (in solid lines) has three regimes. For example, if we consider the Iron branch, it shows a totally diffusive behavior between $E = 10^{14.5}\,\mathrm{eV}$ and $10^{17.5}\,\mathrm{eV}$ (where $r_\mathrm{L} = l_\mathrm{c}$). In this range the Galactic propagation softens the intrinsic spectrum by $1/D(E) \sim E^{-0.3}\,Z^{0.3}$. The second regime lies roughly between $10^{17.5}\,\mathrm{eV}$ and $10^{19}\,\mathrm{eV}$, where $r_\mathrm{L} > l_\mathrm{c}$ and particles random walk with small deflections leaving the Galaxy a bit faster, so $D(E) \sim E^2\,Z^{-2}$ (see Equation 4.3). However the second regime is overwhelmed by the last component, which comes in above $10^{18}\,\mathrm{eV}$ when particles escape faster than the rate they are born, resulting in an event probability of $(1 - e^{-\delta t_\mathrm{obs}/\delta t_\mathrm{birth}})$ and a time dependent flux. The three branches with $Z = 1, 7, 26$ for Hydrogen, CNO, and Iron have similar behaviors along the energy axis scaled by Z, i.e., same behavior for the same rigidity. The relationship between the amplitudes of the flux for each component combines the injection and propagation. The injected spectrum is inversely proportional to the charge $dN_\mathrm{esc}/dE \propto Z^{-1}$. If each of the three elements are injected with fractions $F(Z)$, then $dN/dE \propto Z^{-0.7}\,F(Z)$ in the totally diffusive regime and $dN/dE \propto Z^1\,F(Z)$ in the small deflection regime.

The right panel of Figure 4.2 contrasts the composition predictions of our models with the measurements of $\ln A$ from Tunka (Budnev et al. 2009, filled square), Yakutsk (Knurenko & Sabourov 2010, 2011, open square), CASA-BLANCA (Fowler et al. 2001, open left triangle)), HiRes/MIA (Abu-Zayyad et al. 2001, open circle), HiRes (Abbasi et al. 2010, filled downward triangle), KASKADE-Grande (Apel et al. 2011, filled diamond), Auger (Abreu et al. 2011, filled circle) and TA (Jui 2011, open upward triangle) based on hadronic interaction model EPOSv1.99 (Pierog & Werner 2008). The composition trends of our model reproduces some of the Galactic-Extragalactic transition features at the ankle as shown by the Auger and the KASKADE measurements. The contribution below the ankle depends on the dominant component in this energy range (defined here as more than 80% flux contribution) which may or may not be the pulsars. If the additional flux comes form acceleration

in supernova remnants the composition is likely to be mostly Iron below the ankle (e.g., Ptuskin et al. 2010).

The expected anisotropy signal at the highest energies (above $E_{\rm GZK} \equiv 6 \times 10^{19}\,{\rm eV}$) was already discussed in Fang et al. (2012) and in Section 3.4.5. Because extragalactic pulsars are difficult to detect beyond our Local Group, and because of their transient nature, no direct correlation should be found between the arrival directions of the most powerful events and active sources. The distribution of arrival directions in the sky should trace the large scale galaxy distribution with a possible bias (Kashti & Waxman 2008; Kotera & Lemoine 2008b; Oikonomou et al. in prep.), if the deflections experienced by the particles are small. At energies well below $E_{\rm GZK}$, the arrival directions of particles emitted in extragalactic sources should be isotropic whatever their composition, as the deflections experienced by protons are already large enough to prevent any clustering.

Nevertheless, Galactic sources producing protons above energies $\sim 10^{17}\,{\rm eV}$ could produce substantial anisotropies. In the regime of diffusive propagation, the anisotropy signal in a given direction can be defined as $\mathcal{A}_{\vec{x}} = (\nabla_{\vec{x}} n_{\rm CR}/n_{\rm CR})\,(3\,D/c)$, where $n_{\rm CR}$ is the cosmic ray number density in the Galaxy as measured at the position of the Earth. Blasi & Amato (2012b) showed that by assuming a homogeneous distribution of sources in the Galactic disc, the small-scale anisotropy signal can be simplified to (see also Ptuskin et al. 2006)

$$\mathcal{A} = \frac{3}{2^{3/2}\,\pi^{1/2}}\,\frac{D(E)}{Hc}\ . \tag{4.5}$$

Assuming diffusion parameters $H = 2\,{\rm kpc}$ and $l_{\rm c} = 20\,{\rm pc}$, a strong anisotropy above rigidity $R \sim 4 \times 10^{17}\,{\rm V}$ would be expected from the non-diffusive regime when particles travel semi-rectilinearly. Measurements around $10^{18}\,{\rm eV}$ indicate that cosmic rays at these energies are mostly light (see, e.g., KASCADE-Grande data), and are distributed isotropically in the sky (Kifune et al. 1986; Aglietta et al. 2003; Amenomori et al. 2005). The combination of these measurements require that particles around $10^{18}\,{\rm eV}$ (below the ankle) be protons accelerated in extragalactic sources. Galactic sources injecting protons at these energies would indeed induce strong anisotropies. This is a difficulty for most "ankle"-transition models, for which the extragalactic component becomes quickly underdominant below $E_{\rm ankle} \equiv 10^{18.5}\,{\rm eV}$. This is the case in particular for the Auger-uniform model, in which the transition at $E_{\rm ankle}$ implies that another light extragalactic component is needed to bridge the gap between a Galactic (e.g., SNR) component and the extragalactic pulsar contribution.

For fits to the Auger and TA data, assuming a SFR source emissivity evolution, for energies roughly below $10^{16}\,{\rm eV}$, Galactic pulsars have a negligible contribution to the anisotropy signal, as other Galactic sources (e.g. SNR) dominate (Fang et al. 2013b). For energies above $10^{18}\,{\rm eV}$, extragalactic sources dominate, which should produce a globally isotropic signal. For the energy range in between, Fig. 4.2 shows that the cosmic ray flux is mostly composed of CNO and Iron nuclei, that produce less anisotropy as they have smaller rigidity than protons at the same energy. In addition, Giacinti et al. (2011); Blasi & Amato (2012b) show that effects of stochasticity in the spatial and temporal distribution of sources and turbulent magnetic field could cause significant fluctuation to the intrinsic anisotropy. In general our results are consistent with the anisotropy measurements (Kifune et al. 1986; Aglietta et al. 2003; Amenomori et al. 2005).

Looking into more details, this study reveals the tension between the spectrum, the composition, the anisotropy signal of cosmic rays above $10^{16}\,{\rm eV}$ and the need to have more precise measurements of these observables. The model fitting the Auger data with uniform source evolution (Fig. 4.2), though it can fit successfully the observed spectrum and the composition, requires a second extragalactic component of light elements around $10^{18}\,{\rm eV}$. The SFR source evolution case fits successfully the composition and alleviates the anisotropy issue at $10^{18}\,{\rm eV}$, but one has to invoke a strong magnetic horizon effect to harden the spectrum at $E_{\rm ankle}$ (see Fig. 4 of Fang et al. 2013b). Finally, the fit to TA data is satisfactory for the spectrum and the anisotropy, but does not seem to account well for the observed composition (see Fig. 4 of Fang et al. 2013b).

The results that we provided here for the Galactic component, depend on our choice of parameters. Our fits to the observables of low energy cosmic rays were performed by adjusting key parameters of the Galactic magnetic fields: the coherence length of its turbulent component, $l_{\rm c}$, and the height of its halo, H. Our knowledge on these parameters remain poor (Beck 2008 for a review), and leaves room to other shapes and normalizations for the Galactic component calculated here. For example, for H higher (lower) than 2 kpc, the field would confine $H/2\,{\rm kpc}$ times more (less) nuclei, as $dN_{\rm Gal}/dE \propto H^2/D(E) \propto H$.

The Galactic flux would hence move up (down) by $H/2$ kpc. A larger (smaller) coherence length of the field would enable particles with higher (lower) energy to be confined, and would shift the Galactic component to higher (lower) energies. Note that this effect is non linear, according to Equation 4.3. Further uncertainties in the modeling of particle diffusion, as discussed extensively in Blasi & Amato (2012a), could also noticeably modify the shape of the Galactic spectrum. We also assumed a uniform density of sources in our Galaxy to estimate the average properties, but at the very high energies, cosmic ray observables depend on the particular history of pulsar births in the Galaxy.

On the other hand, our results on the UHE component due to the extragalactic pulsar population can be regarded as fairly robust. For UHECRs indeed, the shape of the propagated spectrum depends mostly on the injected spectrum and composition, the source emissivity evolution (see e.g., Kotera et al. 2010b; Kotera & Olinto 2011), and possibly on the presence of nearby sources at the highest energy end.

The present results also depend on the distribution function of pulsar parameters. We normalized here the overall Galactic and extragalactic spectra based on the data at the highest energies, i.e., with the fastest-spinning pulsars corresponding to the tail of the distribution. Slight variations in the bulk of the population could hence impact the shape of the spectrum, and thus the composition.

We showed in the previous chapter how fast spinning pulsars can explain the observed spectrum of UHECRs (both Auger and TA) and the composition trend described by the Auger collaboration. To fit these two observables a mixed composition of Hydrogen, CNO, and Iron needs to escape the young supernova remnants accelerated via the fast spinning pulsar winds.

Another aspect of this model that we highlighted in this chapter is the connection between parameters needed to fit the extragalactic component and the presence of a Galactic component from Galactic pulsar births in the very high energy range (between 10^{16} and 10^{18} eV). The Galactic component is a natural counterpart to the extragalactic pulsars, although its shape and amplitude could vary with regard to the injection composition and the diffusion parameters. The fact that, within a reasonable range of parameters, the Galactic component does not overwhelm the observed VHECR flux shows that the pulsar model is self-consistent.

Moreover, the estimates presented here suggest that Galactic pulsars could be the main contributors to VHECRs, and bridge the gap between the supernova remnants and the extragalactic pulsars. Note that with this model, pulsars and their surrounding supernovae account for the whole cosmic-ray spectrum observed.

5. Multi-messenger signatures of the pulsar scenario

Secondary neutrinos and photons can be produced by UHECRs when they interact with ambient baryonic matter and radiation fields inside the source or during their propagation from source to Earth. These particles travel in geodesics unaffected by magnetic fields and bear valuable information of the birthplace of their progenitors. The quest for sources of UHECRs has thus long been associated with the detection of neutrinos and gamma rays that might pinpoint the position of the accelerators in the sky.

The detection of these particles is not straightforward however: first, the propagation of gamma rays with energy exceeding several TeV is affected by their interaction with CMB and radio photons. These interactions lead to the production of high energy electron and positron pairs which in turn up-scatter Cosmic Microwave Background (CMB) or radio photons by inverse Compton processes, initiating electromagnetic cascades. As a consequence, one does not expect to observe gamma rays of energy above ~ 100 TeV from sources located beyond a horizon of a few Mpc (Wdowczyk et al. 1972; Protheroe 1986; Protheroe & Stanev 1993). Above EeV energies, photons can again propagate over large distances, depending on the radio background, and can reach observable levels around tens of EeV (Lee 1998). Secondary neutrinos are useful because, unlike cosmic-rays and photons, they are not absorbed by the cosmic backgrounds while propagating through the Universe. In particular, they give a unique access to observing sources at PeV energies. However, their small interaction cross-section makes it difficult to detect them on the Earth requiring the construction of km^3 detectors (see, e.g., Anchordoqui & Montaruli 2010).

The birth of high-energy neutrino astronomy with IceCube

Several experiments have or are been built to search for high energy neutrinos, including DUMAND, AMANDA, NESTOR, ANTARES, IceCube, ANITA (Gorham et al. 2010), the currently in prototype phase radio instruments: the Askaryan Radio Array (ARA, Allison et al. 2012), ARIANNA (Barwick 2011), KM3Net and GRAND[1]. UHECR observatories such as Auger also have the exposure and techniques to identify extremely-high energy neutrinos and are starting to set stringent upper limits to the fluxes (Pierre Auger Collaboration et al. 2012).

IceCube has recently opened the breach for neutrino astronomy, by detecting two PeV energy neutrinos, followed by 35 others from $30\,\mathrm{TeV}-2\,\mathrm{PeV}$ energies (Abbasi et al. 2010; IceCube Collaboration 2013; Aartsen et al. 2014). The flux level is of order $10^{-8}\,\mathrm{GeV\,cm^{-2}\,s^{-1}\,sr^{-1}}$ per flavor and represents a $5.7\,\sigma$ excess above the atmospheric background (neutrinos produced by cosmic ray interactions with the atmosphere). The data are consistent with expectations for equal fluxes of all three neutrino flavors and with isotropic arrival directions, suggesting either numerous or spatially extended sources.

Galactic and extragalactic scenarios have been proposed to explain the observed flux, with a tendency to favor extragalactic models (in particular, starburst galaxies as in the model predicted by Loeb & Waxman 2006; Anchordoqui et al. 2014; Tamborra et al. 2014). Galactic models mostly involve a connection with the Fermi bubble structures (relatively large-scale structures recently detected in gamma-rays and radio, Su et al. 2010; Carretti et al. 2013) or the Galactic halo (Ahlers & Murase 2013; Lunardini et al. 2013; Neronov et al. 2014; Taylor et al. 2014).

Theoretical estimates

Secondary neutrinos and gamma-rays generated at UHECR sources have been investigated by a number of authors (Szabo & Protheroe 1994; Rachen & Mészáros 1998; Waxman & Bahcall 1999; Mücke et al. 1999; Mücke et al. 2000; Anchordoqui et al. 2008; Kachelrieß et al. 2008; Ahlers et al. 2009; Allard & Protheroe 2009; Mannheim et al. 2001, see also Decerprit & Allard 2011 and references therein) with

[1] The Giant Radio Antenna Neutrino Detector is a project planned to detect high energy neutrinos ($\gtrsim 10^{16}$ eV) via the geo-synchrotron effects induced in air-showers of up-going τ neutrinos. It is designed to cover $10^4\,\mathrm{km}^2$ with $45-90$ thousand antennas. The technique has been explored with the TREND experiment (Martineau-Huynh 2012), and the first 35-antenna prototype will be deployed in the summer of 2015.

particular focus on emissions from AGN and transient sources such as GRBs. The case of cluster accretion shocks has been studied by Inoue et al. (2007) and Murase et al. (2008a), and transient sources have been examined in details by Waxman & Bahcall (2000); Dai & Lu (2001); Dermer (2002); Murase et al. (2006, 2008b), and Murase & Ioka (2008) for GRBs and by Murase et al. (2009) for magnetars. The normalization and the very existence of these secondaries highly depend on assumptions about the opacity of the acceleration region and on the shape of the injection spectrum as well as on the phenomenological modeling of the acceleration. For instance, Waxman & Bahcall (1999) obtain an estimate for the cosmic neutrino flux, by comparing the neutrino luminosity to the observed cosmic ray luminosity, in the specific case where the proton photo-meson optical depth equals unity. If the source is optically thick, Allard & Protheroe (2009) demonstrate that cosmic rays are not accelerated to the highest energies and neutrinos above $E \sim$ EeV are sharply suppressed.

The existence of secondaries from interactions during the propagation of cosmic rays is less uncertain, but it is also subject to large variations according to the injected spectral index, chemical composition, maximum acceleration energy, and source evolution history. The magnetic field in the source environment, especially in clusters of galaxies, can play an important role by confining the charged UHECRs and thus leading to increased interaction probabilities (Berezinsky et al. 1997; Colafrancesco & Blasi 1998; Rordorf et al. 2004; de Marco et al. 2006; Armengaud et al. 2006; Murase et al. 2008a; Wolfe et al. 2008; Kotera et al. 2009).

It should be highlighted that due to the delay induced by intergalactic magnetic fields on charged cosmic rays, secondary neutrinos, photons, and gravitational waves should not be detected in time coincidence with UHECRs if the sources are not continuously emitting particles, but are transient such as GRBs and young pulsars.

The sensitivity of IceCube is already highly constraining GRB fireball-type UHECR acceleration models. In such models, the amount of neutrino production in the internal shock regions where ions should be accelerated can be calculated consistently, once assumptions are made on a finite set of parameters such as the baryonic loading, the acceleration efficiency to ultrahigh energies, the jet Lorentz factor, etc. Studies show that the parameter space allowed for these quantities would be strongly reduced if no neutrinos are observed from the position of detected GRBs in the next decade (Abbasi et al. 2011b; He et al. 2012; Li 2012; Hümmer et al. 2012; Baerwald et al. 2014).

In this chapter, we first give an overview of the cosmogenic messengers (produced by UHECRs during their propagation in the intergalactic medium), and discuss where the pulsar scenario described in the previous chapters fit in this picture. We then investigate the diffuse neutrino signature associated with the pulsar scenario, which will be a crucial test to probe the model with IceCube in the coming years. Finally, we discuss gravitational wave signatures of extremely magnetized neutron star (magnetar) scenarios for UHECRs.

5.1. Cosmogenic messengers

The propagation of UHECRs in the intergalactic medium should lead to the production of cosmogenic neutrinos and gamma-rays by interactions on the CMB, infrared and UV backgrounds. The expected cosmogenic neutrino and gamma-ray fluxes depend mostly on parameters inherent to cosmic-rays themselves (their composition and overall flux), but also on the injection index at the source and the source emissivity evolution history for diffuse fluxes (see e.g., Kotera et al. 2010b for a parameter scan over these astrophysical variables). The cosmogenic gamma-ray signatures further depend on the structure and strength of the intergalactic magnetic fields, because of the pair production/inverse Compton cascading of photons in the intergalactic medium.

5.1.1. Diffuse cosmogenic neutrinos fluxes

Kotera, K., Allard, D., & Olinto, A. V. 2010, J. Cos. and Astro. Phys., 10, 13

The diffuse cosmogenic neutrino flux has been calculated under varying assumptions, requiring a fit to the UHECR spectrum (e.g., Engel et al. 2001; Ave et al. 2005; Seckel & Stanev 2005; Hooper et al. 2005; Berezinsky 2006; Stanev et al. 2006; Allard et al. 2006; Takami et al. 2009; Kotera et al. 2010b). Figure 5.1 summarizes the effects of different assumptions about the UHECR source evolution, the Galactic to extragalactic transition, the injected chemical composition, and the maximum injection energy at the source $E_{\max}$, on the cosmogenic neutrino flux. It demonstrates that the parameter space is currently poorly constrained with uncertainties of several orders of magnitude in the predicted flux. UHECR models with large proton $E_{\max}(> 100$ EeV), source

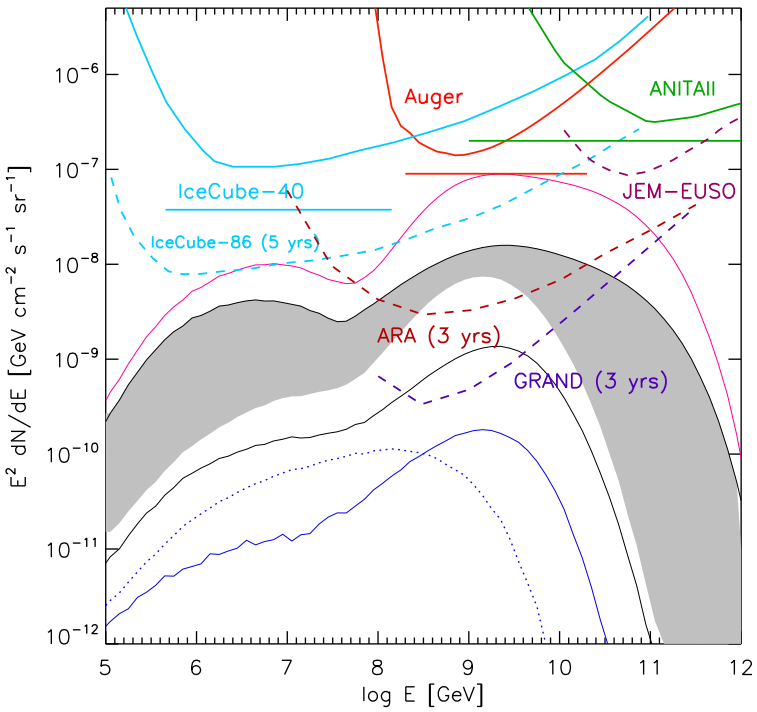

Figure 5.1.: *Cosmogenic neutrino flux for all flavors, for different UHECR parameters compared to instrument sensitivities. Pink solid line: strong source evolution case (Wall et al. 2005) with a pure proton composition, dip transition model, and $E_{\rm max} = 3$ ZeV. This model is already ruled out by the Fermi diffuse gamma-ray background measurements (Decerprit & Allard 2011). Blue lines: uniform source evolution with: iron rich (30%) composition and $E_{Z,\rm max} < Z$ 10 EeV (dotted line) and pure iron injection and $E_{Z,\rm max} = Z$ 100 EeV (solid). Grey shaded range brackets dip and ankle transition models, with evolution of star formation history for $z < 4$, pure proton and mixed 'Galactic' compositions, and large proton $E_{\rm max}(> 100\,{\rm EeV})$. Including the uniform source evolution would broaden the shaded area down to the black solid line. Current experimental limits (solid lines) assume 90% confidence level and full mixing neutrino oscillation. The differential limit and the integral flux limit on a pure E^{-2} spectrum (straight line) are presented for IceCube-40 (pale blue, Abbasi et al. 2010), ANITA-II (green, Gorham et al. 2010) and Auger (red, Abraham et al. 2009). For future instruments, we present the projected instrument sensitivities (dashed lines) for IceCube-86 after 5 yrs (pale blue, Abbasi et al. 2011), JEM-EUSO (Adams et al. 2012), ARA-37 for 3 years (Allison et al. 2012), GRAND for 3 years (see footnote 1 of this chapter).*

evolution corresponding to the star formation history or the GRB rate evolution, dip or ankle transition models (see Chapter 4), and pure proton or mixed 'Galactic' compositions are shaded in grey in Figure 5.1 and give detectable fluxes in the EeV range with $0.06-0.2$ neutrino per year at IceCube and $0.03-0.06$ neutrino per year for the Auger Observatory. This energy range should be soon explored by projected radio instruments such as the Askaryan Radio Array (ARA, Allison et al. 2012), ARIANNA (Barwick 2011), GRAND (see footnote 1 of this chapter).

If EeV neutrinos are detected, PeV information can help select between competing models of cosmic ray composition at the highest energy and the Galactic to extragalactic transition at ankle energies. With improved sensitivity, ZeV ($=10^{21}$ eV) neutrino observatories, such as ANITA and JEM-EUSO could explore the maximum acceleration energy.

5.1.2. Diffuse cosmogenic fluxes for the pulsar scenario

For a source evolution following the star formation rate, as can be expected for neutron stars, an injection of pure proton or proton-dominated compositions with power-law spectral index $\sim 2.0-2.5$ would successfully fit the observed UHECR spectrum. The resulting diffuse cosmogenic neutrino flux would lie within the gray shaded region of Fig. 5.1. For an iron dominated injection up to a few times 10^{20} eV and a proton dominated injection below 10^{19} eV (as we get in Fig. 4.2, but for a source evolution fol-

lowing the star formation rate) one expects a lower neutrino flux, peaking around $E_\nu \sim 10^{8.5}$ GeV with $E_\nu^2(\mathrm{d}N/\mathrm{d}E_\nu)|_{\max} \sim 5 \times 10^9\,\mathrm{GeV\ cm^{-2}\ s^{-1}\ sr^{-1}}$ (red dash-dotted line of Fig. 7 of Kotera et al. 2010b). For the diffuse cosmogenic gamma-ray background, the same fit to the observed UHECR spectrum gives fluxes peaking around $E_\gamma \sim 10\,\mathrm{GeV}$ of order $E_\gamma^2(\mathrm{d}N/\mathrm{d}E_\gamma)|_{\max} \sim 7\times10^{-13}$–$10^{-12}\,\mathrm{eV\,m^{-2}\,s^{-1}\,sr^{-1}}$ for both proton dominated compositions and for our proton to iron transition scenario (see Figs. 4 and 8 of Decerprit & Allard 2011).

5.1.3. Cosmogenic fluxes from single sources

Kotera, K., Allard, D., & Lemoine, M. 2011, A&A, 527, A54

Oikonomou, F., Murase, K., & Kotera, K. 2014, accepted in A&A, ArXiv e-prints: 1406.6075

For single sources, Decerprit & Allard (2011) showed that the cosmogenic neutrino flux could be within reach of IceCube for powerful steady sources (see also Essey et al. 2010). Only beamed sources (i.e., blazars) seem to satisfy the required luminosity condition to be observed by current instruments (otherwise, the required power exceeds the Eddington power), but the neutrino flux is then diluted by the deflection of cosmic rays (Murase et al. 2011). In the case of transient sources, the total received flux should be diluted by the ratio of the emission time to the spread in the arrival times due to the magnetic fields, $\Delta t_\mathrm{s}/\Sigma_t$, which could lower the flux of many orders of magnitude, preventing any detection. In the same token, as was discussed in Gabici & Aharonian (2005) and Kotera et al. (2011), the secondary gamma-ray emission (produced in the intergalactic medium) from a single transient source should be affected by dilution in time, and be below reach of next generation gamma-ray instruments.

The detectability of photons from the electromagnetic cascade triggered by pion production interactions has been addressed by several groups (e.g., Lee 1998; Ferrigno et al. 2004; Armengaud et al. 2006; Gelmini et al. 2007; Kotera et al. 2010a; Essey et al. 2010; Essey et al. 2010, 2011; Essey & Kusenko 2013; Murase et al. 2012; Tavecchio 2014; Takami et al. 2013). The dilution of the cascaded signal – due to the deflection of the electrons and positrons generated during the cascade – depends on the assumptions made regarding the configuration of the intergalactic magnetic fields (IGMF). More specifically, the gamma-ray flux scales as the fraction of the line of sight in which the magnetic field is smaller than the value B_θ such that the deflection

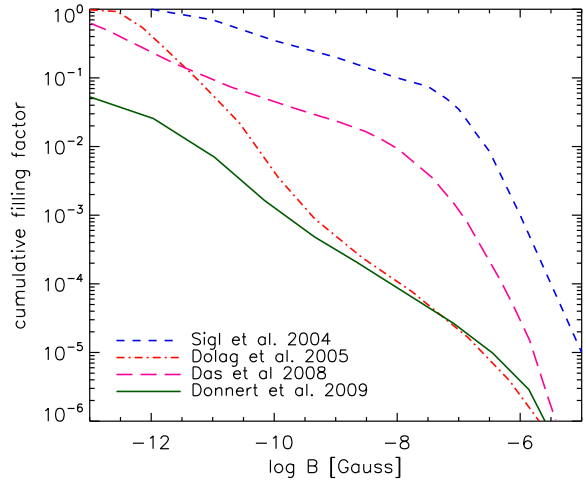

Figure 5.2.: *Cumulative volume filling factor of the extragalactic magnetic field of strength $> B$ for different numerical simulations. Blue dashed: Sigl et al. (2004), red dash-dotted: Dolag et al. (2005), pink long dashed: Das et al. (2008), green solid: Donnert et al. (2009). From Kotera & Olinto (2011).*

of the low energy cascade is θ (Kotera et al. 2010a). For reference, $B_\theta \simeq 2 \times 10^{-14}\,\mathrm{G}$ for $\theta = 1°$ and one can refer to Figure 5.2 for values of this fraction in different magnetic field configurations. Even under optimistic assumption on the magnetic field configuration, only sources with extremely high luminosities $L_{E,19} \gtrsim 3 \times 10^{44}$ erg s$^{-1}(d/100$ Mpc$)^{-2}$ and $L_{E,19} \gtrsim 10^{43}$ erg s$^{-1}(d/100$ Mpc$)^{-2}$ for $E > 10^{19}$ eV could be detected by current instruments such as H.E.S.S. and by the future CTA respectively, with fluxes of order $\sim 10^{-10}$ GeV cm^{-2} s^{-1} around $1-10$ TeV (Ferrigno et al. 2004; Kotera et al. 2010a).

In particular, Takami et al. (2013) showed how the leptonic and UHECR cascade emissions from blazars could be disentangled by the future CTA (see also Zech & Cerruti 2013, for the capabilities of the approach for a statistical discrimination). Indeed, a tail of emission at high energies due to continuous injection of high energy electrons from Bethe-Heitler pair production, could be measured in the integrated flux above ~ 500 GeV (depending on source redshift) for several luminous sources with $z \lesssim 1$ with the future CTA.

Gabici & Aharonian (2005, 2007) argued that one could search for the GeV photons emitted by the synchrotron radiation of the secondary electrons, in presence of substantial magnetic fields in the source environment (commonly called "pair echo/halo emission"). Again, only the cases of rare powerful sources with cosmic ray luminosity $L_{E,19} > 10^{44-46}$ erg s^{-1}

are promising in terms of detectability with both current and up-coming instruments. A source with a cosmic ray luminosity of $L_{E,19} \sim 10^{44}$ erg s^{-1} located at a distance $d \sim 100$ Mpc nearly overshoots the observed cosmic ray spectrum and is thus marginally excluded. Farther sources, with higher luminosity (e.g. $L_{E,19} = 10^{46}$ erg s^{-1} at $d = 1$ Gpc) would thus be more promising to observe in gamma-rays. Such distant sources would contribute to about 10% of the observed spectrum of UHECRs up to $E \sim 10^{19}$ eV, and the cosmic rays produced with higher energy would not reach the Earth due to energy losses (Kotera et al. 2010a).

Several authors (Atoyan & Dermer 2008; Murase et al. 2012; Dermer et al. 2012) have recently investigated the detectability of the synchrotron cascade emission from extreme TeV blazars[2] seeded by UHECRs, taking into account the inverse Compton cascade component in the intergalactic medium, for beamed UHE neutrals (photons and neutrons produced by interactions inside the source region).

In Oikonomou et al. (2014), we have focused on three extreme blazars: 1ES 0229+200, RGB J0710+591 and 1ES 1218+304, and shown that the generated synchrotron pair halo/echo flux from primary UHECRs at the peak energy, assuming that the source is in a magnetized filament, is not sensitive to variations in the overall IGMF strength. This signal is unavoidable in contrast to the inverse Compton pair halo/echo intensity. This is appealing in view of the large uncertainties on the IGMF in voids of large scale structure. It is also shown that the variability of blazar gamma-ray emission can be accommodated by the synchrotron emission of secondary products of UHE neutral beams if these are emitted by UHECR accelerators inside magnetised regions.

Finally, sources located at a distance $\lesssim 10$ Mpc accelerating UHECRs should produce ultrahigh energy photons during their propagation, that can reach the Earth before experiencing Compton cascading. Taylor et al. (2009) studied this potential signature in the particular case of our closest radio-galaxy Cen A (3.8 Mpc) and concluded that Auger should be able to detect $0.05 - 0.075$ photon per year from Cen A, assuming that it is responsible for 10% of the cosmic ray flux above 60 EeV, and assuming a 25% efficiency for photon discrimination.

In the framework of our pulsar scenario more specifically, because of the relatively low luminosity of each source and its transient characteristic (UHECRs are produced only at the earliest stages of the pulsar life), it is not expected that any cosmogenic signal from single sources be observed unless it is located close-by, within tens of Mpc. The dilution discussion for transient sources developed above apply. On the other hand, we demonstrate in the following sections that a diffuse neutrino component could be observed, that is produced in the source environment itself, either during the interaction with the supernova envelope, or during the acceleration process, within the pulsar wind nebula region.

5.2. Diffuse neutrino fluxes associated with the pulsar scenario

Fang, K., Kotera, K., Murase, K., & Olinto, A. V. 2014, submitted to Phys. Rev. D, ArXiv e-prints: 1311.2044

Assuming that cosmic rays are injected following the spin-down power and interact with the surrounding ejecta as in the model described in the previous chapters, we showed in Fang et al. (2013a) that within the parameter-space allowed by this newborn pulsar scenario to reproduce the observed cosmic-ray data (denoted by "minimal pulsar model" in the following), EeV neutrino production occurs *efficiently*. The diffuse neutrino flux produced lies below the current IceCube sensitivity, and is detectable by IceCube and ARA within a decade even in the most pessimistic case. This is a crucial test, since a non-detection can rule out the minimal newborn pulsar scenario within the next decade. The pulsar scenario would be all the more interesting if the heavy composition of UHECRs is confirmed, as photohadronic neutrinos from GRBs and AGN are difficult to detect if UHECRs are mostly nuclei Murase et al. (2008b).

Below we will use the notations employed in Section 3.3.1.

5.2.1. Neutrinos from a single pulsar

At $t = 1\,\mathrm{year}\, t_{\rm yr}$, proton-proton ($pp$) interactions have an effective optical depth $f_{pp} = R_{\rm ej}\, n_p \sigma_{pp} \kappa \sim 0.2\, M_{\rm ej,1}\, \beta_{-1.5}^{-2}\, t_{\rm yr}^{-2}$, with ejecta size $R_{\rm ej}(t) = \beta c t$, interaction cross section $\sigma_{pp} \sim 100\,\mathrm{mb}$, and inelasticity $\kappa \sim 0.7$. Since $\sigma_{Np} \sim A^{2/3}\sigma_{pp}$ and $\kappa \sim 0.7/A$, the effective optical depth for nuclei scales as $\sim A^{-1/3}$.

[2] Radio-loud galaxies presenting a bump of emission at TeV energies, and the particularity that, after correcting for the expected absorption of the intrinsic emission by the extragalactic background light, are exceptionally hard, and thus difficult to reconcile with a standard leptonic emission scenario (e.g., 1ES 1101-232, 1ES 0347-121, 1ES 0229+200, 1ES 1218+304, RGB J0710+591, see Aharonian et al. 2007c,a; Albert et al. 2006; Aharonian et al. 2007b; Acciari et al. 2009, 2010).

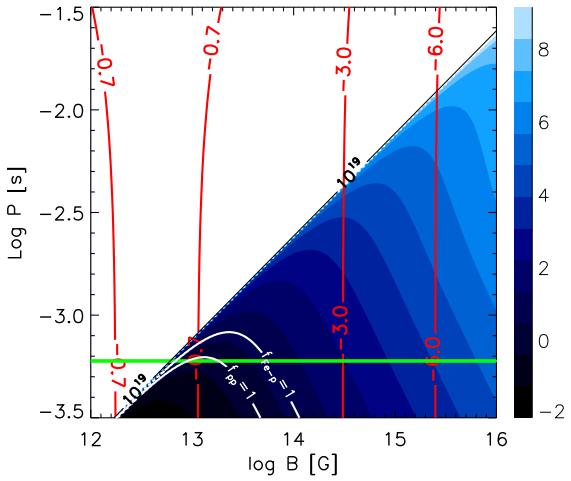

Figure 5.3.: *Effective optical depth* $\log f_{pp}$ *of hadronic interactions in a* $10\,M_\odot$ *supernova ejecta at the time a pulsar with initial period* P *and magnetic field* B *accelerates* 10^{19} eV *protons. Pulsars that can accelerate protons to above* 10^{19} eV *lie under the black line* ($\eta = 0.1$ *assumed). The blue shaded contours span* $f_{pp} = 10^{-2} - 10^{9}$ *(white contours:* $f_{pp} = 1$ *and* $f_{\mathrm{Fe}-p} = 1$ *for comparison). Red lines: pulsar probability distribution function* $\log f(P, B)$*. Green line: minimum spin period of a stable neutron star* $P_{\min} \approx 0.6$ ms *Haensel et al. (1999).*

At early times when UHECR production is possible, the secondary nuclei, nucleons and pions interact with target nucleons and produce higher order nuclei, neutrinos and pions (Murase et al. 2009).

Pions interact with protons with cross section $\sigma_{\pi p} \sim 5 \times 10^{-26}\,\mathrm{cm}^2$, producing additional neutrinos and pions that undergo further πp interactions. This cascade continues until $t_{\pi\mathrm{p}} > \gamma_\pi\,\tau_\pi$, when the πp interaction time $t_{\pi p}$ becomes longer than the primary or secondary pion's life time τ_π in the lab frame. This critical time is $t_\pi = 2 \times 10^6\,\mathrm{s}\,\eta_{-1}^{1/4}\,M_{\mathrm{ej},1}^{1/4}\,B_{13}^{-1/4}\,\beta_{-1.5}^{-3/4}$ (Murase et al. 2009). Then charged pions stop interacting and decay into neutrinos via $\pi^\pm \to e^\pm + \nu_e(\bar{\nu}_e) + \bar{\nu}_\mu + \nu_\mu$.

At the time when cosmic rays are accelerated to $Z10^{19}$ eV (leading to the neutrino energy $\sim 5 \times 10^{17}$ eV), pulsars are surrounded by an ejecta with effective optical depth (including energy losses) $f_{pp} \gtrsim 1$. The production of secondary nucleons is expected for $f_{Np} \gtrsim 1$, as shown in Fig. 5.3. This figure shows that neutrino production is unavoidable in most of the parameter space where UHECRs can be produced. Our results are only mildly sensitive to the ejecta mass as long as $M_{\mathrm{ej}} \gtrsim 3M_\odot$ (Fang et al. 2012). Thus, for typical Type II supernovae, hadronic interactions and the subsequent production of EeV neutrinos should be efficient in the minimal pulsar model.

We have calculated the interactions with the baryonic background of the supernova ejecta (assumed to consist of hydrogen, as more sophisticated composition have little effect on the escaped cosmic ray characteristics Fang et al. 2012) by Monte Carlo for injected nuclei and their cascade products as in Kotera et al. (2009); Fang et al. (2012, 2013b). Tables for πp interactions were generated using the hadronic model EPOS (Werner et al. 2006). Note that neutrinos from secondary nuclei contribute significantly and dominate over leading nuclei in neutrino production.

5.2.2. Diffuse neutrino intensity

The averaged neutrino and cosmic ray spectrum from the pulsar population following the distribution computed in Faucher-Giguère & Kaspi (2006) is given by Eq. (3.13). The population of extragalactic pulsars expected to contribute to the diffuse neutrino background then reads:

$$\Phi_\nu = \frac{f_{\mathrm{s}}}{4\pi} \int_0^{z_{\mathrm{D}}} \int_0^{t_\nu} \frac{\mathrm{d}N_\nu}{\mathrm{d}t'\,\mathrm{d}E_\nu\,4\pi D^2}\,\mathrm{d}t'\,\Re(z)\,4\pi D^2\,\frac{\mathrm{d}D}{\mathrm{d}z}\,\mathrm{d}z\ . \tag{5.1}$$

The inner integral counts the neutrinos emitted by each pulsar toward the Earth during its neutrino-loud lifetime $t_\nu = \min(t_{pp}, t_\pi)$. This averaged contribution from an individual star is then integrated over the entire source population in the universe up to the first stars, at redshift $z_{\mathrm{D}} \approx 11$. The local birth rate of pulsars is set to the rate of core-collapse supernovae $\Re(0) = \nu_{\mathrm{s}} n_{\mathrm{gal}} \sim 1.2 \times 10^{-4}\,\mathrm{yr}^{-1}\,\mathrm{Mpc}^{-3}$ (van den Bergh & Tammann 1991). The source emissivity is assumed to either follow the star formation rate (SFR), or be uniform over time.

The ion injection rate is reduced by the pair loading, particle acceleration mechanisms, and geometry of the current sheet, all taken into account in the prefactor $f_{\mathrm{s}} < 1$. As previously done, f_{s} is obtained by fitting the simulation output to the data. The resulting neutrino flux does *not* depend on f_s since it is directly normalized by the cosmic-ray data. The injected elements are divided into three groups (adding more elements does not refine the fit, and introduces unnecessary free parameters): H, CNO, and Fe. The relative abundance of the three groups of injected elements (H,CNO, Fe, see discussion in Chapter 4) is chosen to best fit the spectrum and the main estimators of the composition measured by Auger, the mean air-shower elongation rate $\langle X_{\max}\rangle$ and its root mean square $\mathrm{RMS}(X_{\max})$. Our best fit results are

obtained assuming SFR source evolution, ejecta mass $M_{\rm ej} = 10\,M_\odot$, wind acceleration efficiency $\eta = 0.3$, injected composition 50% H, 30% CNO, 20% Fe, and normalization $f_{\rm s} = 0.05$, as represented in Fig. 5.4.

The associated diffuse neutrino fluxes are shown in Fig. 5.5. The blue line corresponds to the cosmic-ray counterpart shown in Fig. 5.4, with SFR source emissivity evolution. The black line represents the flux for a uniform source emissivity, which is a conservative case. The neutrino spectrum consists of three components. The energy range below $\sim 10^{16}$ eV corresponds to pulsars that spin with period $P \gtrsim 20$ ms. Only few interactions happen as the ejecta is mostly diluted when cosmic rays are produced.

The all flavor neutrino flux sensitivities of the IceCube detector after one year and five years of operation are shown in Figure 5.5 (Abbasi et al. 2011), as well as the projected ARA-37 3-year sensitivity (Allison et al. 2012). In the SFR case, more appropriate in the pulsar scenario, the flux level of neutrinos from newborn pulsars is marginally consistent with the current non-detection at high energies, and should be detected in another three years of IceCube operation. The uniform case predicts a less optimistic flux, that still lies above the ARA 3-year sensitivity, and at a level that would be detected by IceCube within a decade.

The cosmogenic neutrinos produced during the intergalactic propagation are not shown in Figure 5.5. This flux would be of the order of the SFR case with mixed composition in Kotera et al. (2010b), represented by the lower boundary of the gray shaded region of their Fig. 5.1. The flux is below $\sim 6 \times 10^{-9}\,{\rm GeV\,cm^{-2}\,s^{-1}\,sr^{-1}}$, and is sub-dominant compared to the flux presented here.

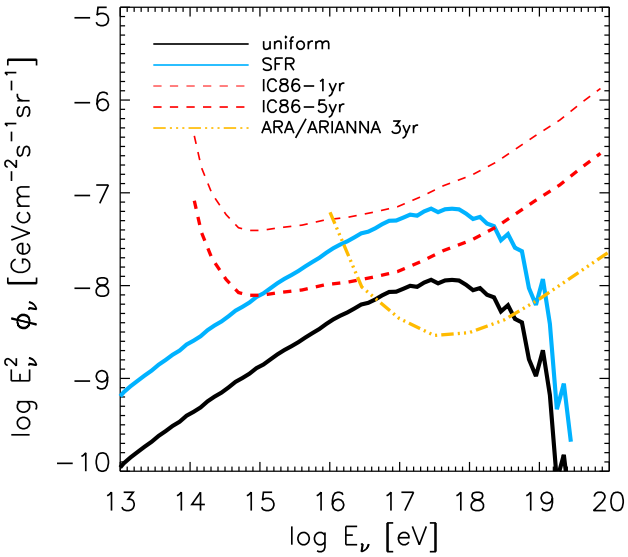

Figure 5.5.: *Diffuse neutrino flux ($\nu_\mu + \nu_e + \nu_\tau$ after neutrino mixing in space) from extragalactic newborn pulsar population with SFR (blue) or uniform (black) source emissivity, that would produce the measured UHECRs. All flavor neutrino flux sensitivities of the IceCube detector after 1 yr (red thin dash) and 5 yrs (red thick dash) of operation (Abbasi et al. 2011), expected 3-year ARA-37 sensitivities (orange dash dotted) (Allison et al. 2012).*

Discussion

As shown in Fig. 5.3, $f_{pp} \gtrsim 1$ at the time when cosmic rays are accelerated to $\sim Z10^{19}$ eV as long as $M_{\rm ej} \gtrsim 3M_\odot$ (corresponding to $\beta \lesssim 0.05$). The neutrino flux is also insensitive to the injection composition because neutrinos are efficiently produced at relatively early times. Ions are injected with a rate $\dot{N} \propto Z^{-1}$ and act effectively as A nucleons in hadronic interactions (so that the energy of neutrinos from any species with mass number A and charge Z is $\propto Z/A \sim 0.5$). The dependence on acceleration efficiency is small as long as $\eta \gtrsim 0.1$ (the minimum value for UHECR production).

As noted before, thermal and nonthermal radiations are also expected to lead to photodisintegration (Murase et al. 2009; Fang et al. 2012; Kotera et al. 2013). Murase et al. (2009) showed that the thermal radiation background of the supernova ejecta can play a role in the magnetar case. In addition, X-ray and γ-ray nonthermal fields in the pulsar wind nebula could be strong enough to compete with the hadronic channel. However, if photohadronic neutrinos are dominant, nuclei would be mostly disintegrated due to the larger photodisintegration cross sections (Murase & Beacom 2010), and the scenario would fail at satisfying our primary requirement of reproducing the Auger data.

A caveat of the pulsar origin is the uncertainties on the detailed acceleration mechanism. Though the viability of this scenario depends on an efficient acceleration process, since the cosmic-ray flux is normalized by the observations, the diffuse neutrino flux we predict does not depend on the underlying details. Fermi mechanisms lead to softer cosmic-ray injections than the hard E^{-1}-spectrum. However, the secondary products from interactions with the ejecta soften the spectrum to E^{-2} above 10^{17} eV, and this effect is less pronounced in the case of a softer intrinsic spectrum, because less high energy primaries are injected. The combination of these antagonist effects argues also against a significant

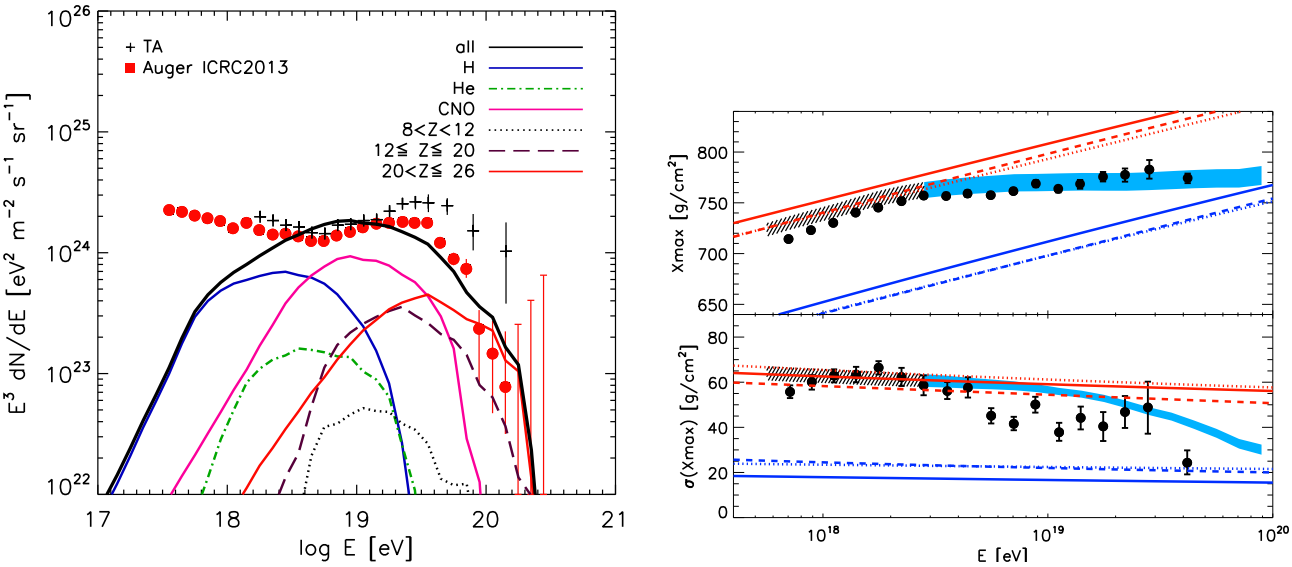

Figure 5.4.: Left: *Spectrum of UHECRs from newborn pulsars, assuming SFR source emissivity and* 50% *H,* 30% *CNO and* 20% *Fe at injection. Overlaid are measurements by Auger (Aab et al. 2013) and Telescope Array (Tameda et al. 2011) with energy rescaling suggested in Dawson et al. (2013).* Right: *Estimators of UHECR composition,* $\langle X_{\rm max}\rangle$ *and RMS(*$X_{\rm max}$*) of the Auger data (Aab et al. 2013) (black crosses) and simulation results with pulsar sources (blue shaded if pulsars contribute to more than* 80% *of the total flux, hashed otherwise). Hadronic interaction models EPOS-LHC (solid), QGSJetII-04 (dotted) and Sibyll2.1 (dash) are used (De Domenico et al. 2013). Red and dark blue lines: pure proton and iron compositions respectively. Note: the fit to the spectrum is different from Fig. 3.5 because the source emissivity is considered to follow the SFR here, while it was taken as uniform in the previous plot.*

change in the neutrino flux between $0.1-1\,$EeV, for softer injections.

As mentioned in Section 5, IceCube has reported the detection of 28 neutrinos at PeV energies and below (Abbasi et al. 2010; IceCube Collaboration 2013; Aartsen et al. 2014). No event has been observed yet at higher energies. Our model predicts a neutrino peak at $0.1-1\,$EeV, and a flux about an order of magnitude lower than the observed flux around PeV energies (a softer injection spectrum would lead to fewer UHECR interactions and would not add much neutrino flux at this energy). In principle, having a neutrino peak at PeV energies is possible for $\eta \ll 0.1$, but then, the UHECR data cannot be explained.

The minimal pulsar scenario predicts a diffuse neutrino flux of $\sim 10^{-8}-10^{-7}$ GeV cm^{-2} s^{-1} sr^{-1}. A lower neutrino flux is possible only in the case of i) a jet puncture, expected only for high-power winds, ii) a "shredding" of the envelope through Rayleigh-Taylor instabilities (Arons 2003), which could happen if $E_{\rm rot} > E_{\rm ej}$, iii) a thinner ejecta, for low-mass envelope or accretion-induced collapses. However, all these cases are nontypical and expected in rare types of supernovae. Also, particles escaping without interactions would not produce light secondary nuclei at lower energies, and it is not clear whether the produced cosmic rays can fit the data.

5.2.3. Neutrinos produced during acceleration in the PWN

Lemoine, M., Kotera, K. & Pétri, J. 2014, submitted to JCAP, ArXiv e-prints:***

The detection of neutrinos associated with hadronic and photo-hadronic interactions of nuclei in the nebula, during or after the acceleration process sketched in 3.2.2 (we will follow in this section the notations used in that section), would provide an unmabiguous test of the present scenario. Let us first consider the yield of neutrinos through photo-hadronic interactions on the nebula spectral energy distribution (SED), as calculated in Eq. (A.21). We consider only primary protons in this section; the neutrino yield for heavier nuclei will be smaller by a factor of a few.

The neutrino spectrum is then shaped by the accelerated proton spectrum and by the conversion efficiency. A parent proton produces 3 neutrinos per $p-n$ conversion, which takes place with probability 1/3 in each photopion interaction, thus on a timescale $t_{\gamma\pi^+} = 3t_{\gamma\pi}$, where $t_{\gamma\pi}$ is the photo-pion production timescale. At the detector, the neutrino carries a fraction $f_\nu/(1+z) \simeq 0.05/(1+z)$ of the parent proton energy $E_{\rm i}$, i.e. $E_\nu \simeq f_\nu E_{\rm i}/(1+z)$, with z the redshift of the source.

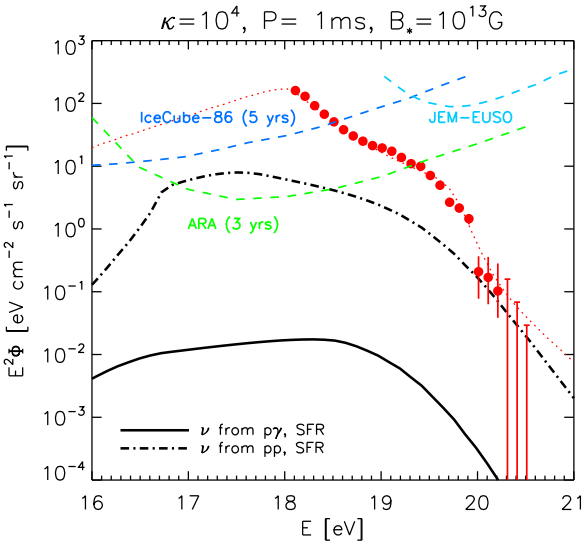

Figure 5.6.: *Neutrino spectra produced via pp (dot-dashed) and $p\gamma$ (solid) interactions for a population of pulsars with initial rotation period $P_{-3} = 1$, dipole magnetic field $B_{\star,13} = 1$, leptonic multiplicity $\kappa_4 = 1$, $\eta_{\rm rad} = 0$, $\eta_{\rm B} = 0.1$, and occurrence rate $\dot{n}_{\rm s}(0) = 28\ Gpc^{-3}\ yr^{-1}$ with a source evolution following the star formation rate. The sensitivity of IceCube-86 for 5 years (Abbasi et al. 2011), JEM-EUSO (Adams et al. 2012), and ARA-37 for 3 years (Allison et al. 2012) are overplotted. In red dotted lines, the fit to the UHECR spectrum measured by the Auger Observatory (Aab et al. 2013), in red circles.*

The time-dependent neutrino spectrum emitted by one PWN at luminosity distance $D_{\rm L}$ can be written:

$$E_\nu^2 \Phi_\nu(E_\nu, t) \;=\; \frac{(1+z)}{4\pi D_{\rm L}^2} E_\nu^2 \frac{3}{t_{\gamma\pi^+}(E_{\rm i})} \frac{{\rm d}E_{\rm i}}{{\rm d}E_\nu} \frac{{\rm d}N_{\rm i}}{{\rm d}E_{\rm i}} \;, \tag{5.2}$$

in terms of the parent proton spectrum ${\rm d}N_{\rm i}/{\rm d}E_i$ in the source. The latter is formally given by

$$\frac{{\rm d}N_{\rm i}(t)}{{\rm d}E_{\rm i}} \;=\; \eta_{\rm i} \int_0^t q_{\rm i}(t') \frac{L_{\rm w}(t')}{E_{\rm diss.}^2} \left[\frac{E_{\rm i,0}(t')}{E_{\rm diss.}(t')}\right]^{-s} \times \frac{{\rm d}E_{\rm i,0}(t')}{{\rm d}E_{\rm i}} e^{-\int_{t'}^t {\rm d}t''/t_{\rm exit}[t'', E_{i,0}(t'')]} {\rm d}t' \;, \tag{5.3}$$

with $q_{\rm i}(t') = (s-2)/\left\{1 - [\gamma_{\rm max}(t')/\gamma_{\rm diss.}(t')]^{2-s}\right\}$ a normalization prefactor. The energy $E_{\rm diss.} \equiv \gamma_{\rm diss.} m_p c^2$, while $E_{\rm i,0}(t')$ represents the energy of the proton at time t', which shifts down to $E_{\rm i}$ at time t due to adiabatic losses. The timescale $t_{\rm exit} = \left(t_{\gamma\pi^+}^{-1} + t_{\rm esc}^{-1}\right)^{-1}$ represents the timescale on which protons leave the source, either through $p-n$ conversion or through direct escape on timescale $t_{\rm esc}$. This solution neglects the energy loss associated with photo-pion production; the latter is small and the probability of exiting directly the source as a neutrons significant, therefore photo-pion production effectively acts as a loss term from the nebula.

In order to simplify the above calculation, we make the usual approximation, e.g. Rachen & Mészáros (1998), that neutrino production takes place during a timescale $t_{\rm loss} = \left[t_{\rm ad}^{-1} + t_{\rm esc}^{-1} + t_{\gamma\pi+}^{-1}\right]^{-1}$ and that the proton spectrum can be described by its time average on that timescale. Here, $t_{\rm ad} = R_{\rm PWN}/(\beta_{\rm PWN} c)$ characterizes the adiabatic loss timescale. Direct escape takes place on timescale $t_{\rm esc} \simeq R_{\rm PWN}\,(\gamma_{\rm i}/\gamma_{\rm conf})^{-1}$, corresponding to the assumption of diffusive escape with a Bohm scattering timescale $\sim r_{\rm g}/c$. The average proton spectrum is

$$\left\langle \frac{{\rm d}N_{\rm i}(t)}{{\rm d}E_{\rm i}} \right\rangle \;=\; \min\left(1, \frac{t_{\rm loss}}{t_{\rm p}}\right) \frac{\eta_i q_i L_{\rm p} t_{\rm p}}{E_{\rm diss.}^2} \left(\frac{E_{\rm i}}{E_{\rm diss.}^2}\right)^{-s} . \tag{5.4}$$

Indeed, if $t_{\rm loss} \gg t_{\rm p}$, the pulsar luminosity function can be approximated as impulsive, $L_{\rm w} \sim t_{\rm p} L_{\rm p} \delta(t - t_{\rm p})$, while if $t_{\rm loss} \ll t_{\rm p}$, the luminosity is approximately constant up to time $t_{\rm p}$, but at any time, the energy contained in protons is a fraction $t_{\rm loss}/t_{\rm p}$ of the energy injected over time $t_{\rm p}$. One thus derives a neutrino energy flux

$$E_\nu^2 \Phi_\nu \;\simeq\; \frac{1+z}{4\pi D_{\rm L}^2} \frac{f_\nu}{t_{\gamma\pi}} \min\left(1, \frac{t_{\rm loss}}{t_{\rm p}}\right) \eta_{\rm i} q_{\rm i} L_{\rm p} t_{\rm p} \left(\frac{E_\nu}{E_{\nu\star}^2}\right)^{2-s} , \tag{5.5}$$

with $E_{\nu\star} \equiv f_\nu E_{\rm diss.}/(1+z)$. To put figures on this result, consider a pulsar with $L_{\rm p} \sim 10^{45}\,{\rm erg/s}$ and spin-down timescale $t_{\rm p} \sim 3 \times 10^7\,{\rm s}$, at luminosity distance $D_{\rm L}$: the peak energy $E_{\nu\star} \sim 10^{17}\,{\rm eV}$, and the neutrino energy flux is: $E_{\nu\star}^2 \Phi_{\nu\star} \sim 0.6 \times 10^{-3}\,(D_{\rm L}/100\,{\rm Mpc})^{-2}\,{\rm eV\,cm^{-2}\,s^{-1}}$. The sensitivity of IceCube for point-sources is of order $1\,{\rm eV\,cm^{-2}\,s^{-1}}$, for the most optimistic declination angle (Abbasi et al. 2010). Therefore, only a (rare) chance occurrence of a source as above at distance $D_{\rm L} \lesssim 10\,{\rm Mpc}$ could produce a detectable flux in a km^3 neutrino telescope.

The diffuse neutrino flux produced by such PWNe can be evaluated as follows. Writing $\dot{n}_{\rm s}$ the occurrence rate per comoving volume element, the effective density at any time is $\max(t_{\rm loss}, t_{\rm p})\,\dot{n}_{\rm s}$, since $\max(t_{\rm loss}, t_{\rm p})$ indicates the effective duration of neu-

trino emission. The diffuse energy flux then reads

$$E_\nu^2 j_\nu = \frac{c}{4\pi}\int_0^{+\infty}\frac{\mathrm{d}z}{H(z)(1+z)}\,\dot{n}_\mathrm{s}\frac{t_\mathrm{loss}}{t_{\gamma\pi}} \times f_\nu\,\eta_\mathrm{i} q_\mathrm{i} L_\mathrm{p} t_\mathrm{p}\left(\frac{E_\nu}{E_{\nu\star}^2}\right)^{2-s}. \quad (5.6)$$

Note that $\dot{n}_\mathrm{s}$ may contain a redshift dependence, and that t_loss and $t_{\gamma\pi}$ depend on the (source rest-frame) energy $(1+z)E_\nu$.

In order to evaluate the neutrinos flux that results from pp interactions in the nebula environment, we consider only the interactions that arise as the cosmic rays cross the supernova remnant, given the very low density of particles within the nebula itself. As discussed in Fang et al. (2012) and Section 3.3.2, the optical depth to pp interactions during the crossing of a $10M_\odot$ supernova remnant can be written $\tau_{pp} \simeq 0.3\,\mathrm{yr}/t_\mathrm{esc}$. pp interactions only take place whenever $t_\mathrm{esc} < t_\mathrm{ad}$ and $t_\mathrm{esc} < t_{\gamma\pi^+}$. Given the small optical depth to photo-pion production, the latter condition is always satisfied; the former amounts to $\gamma > \beta_\mathrm{PWN}\gamma_\mathrm{conf}$, therefore the pp neutrino signal only concerns the highest energy range. It is then straightforward to evaluate the pp neutrino flux from a single source and the diffuse flux from Eqs. (5.5),(5.6), making the substitutions $t_{\gamma\pi} \to \tau_{pp}R_\mathrm{PWN}/c$ and $t_\mathrm{loss} \to t_\mathrm{esc}$.

Figure 5.6 presents the neutrino spectrum produced by pp (dot-dashed) and $p\gamma$ (solid) interactions, for protons accelerated with a spectral index of $s = 2.2$, for a population of pulsars with identical parameters, with initial rotation period $P_{-3} = 1$, dipole magnetic field $B_{\star,13} = 1$, leptonic multiplicity $\kappa_4 = 1$, $\eta_\mathrm{rad} = 0$, $\eta_\mathrm{B} = 0.1$. The birth rate of these sources are assumed to have an occurrence rate scaled to the star formation rate (SFR) with $\dot{n}_\mathrm{s} = 28\,\mathrm{Gpc}^{-3}\,\mathrm{yr}^{-1}$ at $z = 0$. The calculation of the cosmic-ray spectrum considers energy losses during propagation in the intergalactic medium. In this figure, the occurrence rate has been chosen so as to match the cosmic-ray flux at energies as low as 10^{18} eV, which provides a maximum neutrino flux for this scenario. In the $p\gamma$ production channel, adiabatic losses reduce considerably the flux for neutrinos produced below these energies.

The neutrino flux produced by pp interactions lies slightly below the 5-year sensitivity of IceCube-86 and above the 3-year sensitivity of the projected Askaryan Radio Array (ARA). It would thus be detectable in the next decade. Note that if the primaries were heavier nuclei and not protons, these estimates would be reduced of a factor of a few (see e.g., Murase & Beacom 2010).

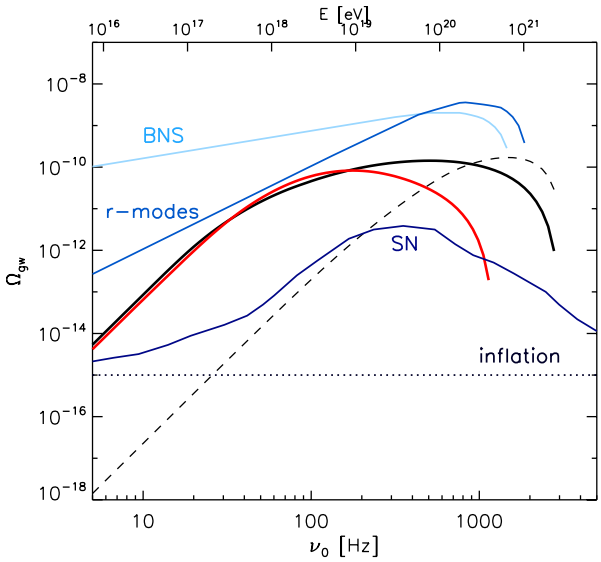

Figure 5.7.: *Energy densities of the gravitational wave backgrounds produced by astrophysical or cosmological mechanisms. Signal for a magnetar population with uniform parameters (black dashed), with distribution of initial voltages (solid black) and angular velocities (solid red), for $E_\mathrm{g} = 30$ EeV (see Kotera 2011 for more details). Backgrounds from binary neutron star coalescence (Regimbau & Mandic 2008), r-modes assuming that 1% of newly born neutron stars cross the instability window (Regimbau 2011), core-collapse supernovæ (Buonanno et al. 2005). Horizontal dotted line: maximum version of the gravitational wave stochastic spectrum produced during slow-roll inflation (Turner 1997).*

5.3. Gravitational-wave signatures for magnetars

Kotera, K. 2011, Phys. Rev. D, 84, 023002

Within the zoo of neutron stars, those with extremely strong surface dipole fields of $B \sim 10^{15}$ G and fast rotation at birth called *magnetars* (see Woods & Thompson 2006; Harding & Lai 2006; Mereghetti 2008 for reviews) have attracted particular attention because of their energetics (Arons 2003; Murase et al. 2009; Metzger et al. 2011b; Kotera 2011). This subpopulation, the existence of which was predicted in the 90s (Duncan & Thompson 1992), is accepted as the explanation to the observed Soft Gamma Repeaters and Anomalous X-ray Pulsars (Kouveliotou et al. 1998, 1999; Baring & Harding 2001).

A messenger that is scarcely discussed in relation to UHECRs is gravitational waves. If anisotropy sig-

nals reveal that the source is of transient type, one way to establish if UHECR sources could be magnetars would be to look for gravitational waves signals. Note that GRBs, which are transient sources commonly put forward as UHECR producers (though IceCube tends to put stringent constraints on the GRB fireball model as UHECR accelerators, see Abbasi et al. 2011b; He et al. 2012; Li 2012; Hümmer et al. 2012; Baerwald et al. 2014), are believed to produce only faint and signals below detectability (e.g., Piran 2004). In Kotera (2011), we showed that the distribution of magnetar initial voltages required to reconcile the produced spectrum to the observed one, should lead to higher stochastic gravitational wave signals from these objects than previously calculated (e.g., Regimbau & Mandic 2008). The observation of such a gravitational wave signal could be a probe that these objects meet the requirements (in terms of magnetization, rotation velocity, inertial momentum) to accelerate UHECRs to the highest energies.

Highly magnetized magnetars with fields $B \gtrsim 10^{15}\,\mathrm{G}$ should be strong emitters of gravitational waves. If protons are injected by pulsars, the hard produced spectrum requires a specific distribution of pulsar parameters (of their initial rotation velocity and/or their magnetic field strength) to soften the overall UHECR spectrum and fit the observations (Kotera 2011). In such a case, and for strong pulsar internal deformations, we argued that a characteristic diffuse gravitational wave signal would be produced, that could be detected with future generation detectors such as DECIGO or BBO, and are within reach of the sensitivity of the third generation LIGO-type detectors in correlation mode (LIGOIII, Einstein Telescope). Our most optimistic signal is shown in Fig. 5.7. The physical assumptions required for such a level of detection can be viewed as optimistic, but are still plausible in the magnetar formation scenarios. The signal obtained can be up to $3-4$ orders of magnitude higher than standard predictions in the frequency range $1-100$ Hz that will be best measured by these future generation instruments.

The neutron-star model presented in the previous chapters shows however that these strong magnetic fields would induce a fast spin-down time that could not allow the escape of UHECRs in presence of a dense supernova shell. The problem could be bypassed if the envelope is particularly under-dense, if particles could escape through a breech created by a proto-pulsar jet (but interactions with the radiative background would no longer be negligible in that case), or for envelope shredding scenarios as invoked by Arons (2003). For the milder fields favored in our scenario ($B \sim 10^{13}\,\mathrm{G}$), the gravitational wave signal is expected to be lower by many orders of magnitude, far below the reach of any planned instruments.

6. Diagnosing pulsar winds with cosmic-ray signatures

The studies described in the previous chapters aim at understanding the origin of UHECRs; they can be reversed to diagnose pulsar winds themselves. The interaction of pulsar winds with their surroundings offers indeed a chance to measure the energy and the composition of pulsar winds.

Pulsar wind nebulae, that develop due to shocks at the interface between the wind and the interstellar medium or the debris of the SN (see Appendix A and, e.g., Chevalier 2005; Bucciantini et al. 2006; Gaensler & Slane 2006; Kirk et al. 2009), are good calorimeters in this sense. This so-called"termination-shock" region is thought to be responsible for most of the emitted radiation by the nebula.

Upstream of the termination shock, the energy of the pulsar wind is distributed between electrons and positrons, ions, and magnetic fields, but the fraction of energy imparted to particles is uncertain. Near the neutron star, the Poynting flux is likely to be the dominant component of the outflow energy.

The effects of the interaction of the wind of a very young pulsar born with millisecond periods (from its birth to a few years later) with the surrounding supernova ejecta has curiously never been examined. The dumping of the tremendous rotational energy of the pulsar into the ejecta, over timescales of order a few years, should lead to peculiar luminosity supernovae. We examine in the next section the thermal and non thermal signatures of such events.

However, the observations of the pulsar wind nebula mostly gives us information about the properties of the shocked region, and not about the unshocked pulsar wind. Binary systems where pulsar winds irradiate the atmosphere of the companion and lead to peculiar emission features, can serve this purpose. We examine these effects in Section 6.2.

6.1. Signatures of pulsars in the light curves of early supernova ejecta

Kotera, K., Phinney, E. S., & Olinto, A. V. 2013, MNRAS, 432, 3228

Core-collapse supernovae are triggered by the collapse and explosion of massive stars, and lead to the formation of black holes or neutron stars (see, e.g., Woosley et al. 2002). In particular, pulsars are believed to be commonly produced in such events. The observed light curves of core-collapse supernovae present a wide variety of shapes, durations, and luminosities, that many studies have endeavored to model, considering the progenitor mass, explosion energy, radioactive nucleosynthesis, and radiation transfer mechanisms in the ejecta (e.g., Hamuy 2003; Utrobin & Chugai 2008; Baklanov et al. 2005; Kasen & Woosley 2009).

While they spin down, pulsars release their rotational energy in the form of a relativistic magnetized wind. The effects of a central pulsar on the early supernova dynamics and luminosity is usually neglected, as the energy supplied by the star is negligible compared to the explosion energy, for the bulk of their population. Some pioneering works have however sketched these effects (Gaffet 1977a,b; Pacini & Salvati 1973; Bandiera et al. 1984; Reynolds & Chevalier 1984), notably in the case of SN 1987A (McCray et al. 1987; Xu et al. 1988). More recently, Kasen & Bildsten (2010); Dessart et al. (2012) discussed that magnetars, a sub-class of pulsars born with extremely high dipole magnetic fields of order $B \sim 10^{14-15}$ G and millisecond spin periods, could deposit their rotational energy into the surrounding supernova ejecta in a few days. This mechanism would brighten considerably the supernova, and could provide and explanation to the observed superluminous supernovae (Quimby 2012).

In this section, we explore the effects of mildly magnetized pulsars born with millisecond periods (such as the Crab pulsar at birth) on the light curves of the early supernovae ejecta. Such objects are expected to inject their tremendous rotational energy in the supernovae ejecta, but over longer times compared to magnetars (of order of a few years). Indeed, the spin-down and thus the timescale for rotational energy deposition is governed by the magnetization of the star (see Eq. A.1).

We estimate the thermal and non thermal radiations expected from these specific objects, concentrating at times of a few years after the onset of the explosion. We find that the bolometric light curves present a high luminosity plateau (that can reach 10^{43-44} erg/s) over a few years, and that an equally

bright TeV gamma-ray emission could also appear after a few months to a few years, from the acceleration of particles in the pulsar wind, depending on the injection parameters. A milder associated X-ray peak (of luminosity 10^{40-42} erg/s) could also be produced around the same time. The observations of these signatures by the following up of a large number of supernovae could have important implications for the understanding of core-collapse supernovae and reveal the nature of the remnant compact object.

Quantities necessary for this analysis in the regimes of interest for the ejecta (optically thin or thick) can be found in Appendix A and C.

6.1.1. Bolometric radiation

We first estimate the total radiation expected from the supernova ejecta+pulsar wind nebula. The evolution of the ejecta is computed assuming a one zone core-collapse model (Arnett 1980). Detailed calculations are presented in Appendix C.1. How much energy of the pulsar wind will be transformed into radiation depends on many factors such as the nature of the wind (leptonic, hadronic or Poynting flux dominated), the efficiency of particle acceleration and of radiative processes. In a first step, these conditions can be parametrized by setting a fraction η_γ of the wind energy $E_{\rm p}$ that is converted to radiative energy (thermal or non thermal) in the pulsar wind nebula.

Fig. 6.1 presents the bolometric luminosity radiated from the ejecta+PWN system for various sets of pulsar parameters. Even with a $\eta_\gamma < 10\%$, the plateau in the light curve a few years after the explosion is highly luminous, especially for $P = 1\,$ms. This high luminosity plateau stems from the injection of the bulk of the pulsar rotational energy a few years after the supernova explosion. The luminosity is quickly suppressed for high B (for magnetar-type objects), due to the fast spin-down. Supernovae embedding isolated millisecond pulsars with standard magnetic field strengths would thus present unique radiative features observable a few years after their birth.

6.1.2. Thermal/non-thermal emissions

The bolometric radiation calculated in the previous section stems from the re-processing of high energy radiation created at the base of the SN ejecta, in the PWN region. In the standard picture of PWN, high energy particles (leptons and hadrons) are injected at the interface between the pulsar wind and the ejecta, and radiate high energy photons (X rays and gamma rays). These high energy photons can be either thermalized if the medium (the PWN and/or the SN ejecta) is optically thick to these wavelengths, or can escape from the ejecta and be observed as a high energy emission, if the medium they have to propagate through is optically thin. In this section, we calculate in more detail the emission a few years after the explosion, concentrating mainly on the case of a leptonic wind.

After many hundreds of years, observational evidence show that the energy repartition at the termination shock of pulsar wind nebulae is dominated by particles (e.g., Arons 2007). The conventional picture is thus that all but $\sim 0.3 - 1\%$ of the Poynting flux has already been converted into the plasma kinetic energy by the time the flow arrives the termination shock (Kennel & Coroniti 1984a,c; Emmering & Chevalier 1987; Begelman & Li 1992), $\sim 1\%$ appearing to be a level required to reproduce the observed shape of the Crab Nebula (Komissarov & Lyubarsky 2004; Del Zanna et al. 2004). As already mentioned in Section 3.2.2, how this transfer happens is subject to debate (see, e.g., Kirk et al. 2009).

Particles and the Poynting flux are injected in the pulsar wind nebula at the termination shock. We will note the energy repartition between electrons and positrons, ions and the magnetic field in the pulsar wind nebula: $L_{\rm p} = (\eta_{\rm e} + \eta_{\rm i} + \eta_{\rm B})L_{\rm p}$. The ratio between $\eta_{\rm i}$ and $\eta_{\rm e}$ is the subject of another debate (see e.g., Kirk et al. 2009). However, various authors (e.g., Gelfand et al. 2009; Fang & Zhang 2010; Bucciantini et al. 2011; Tanaka & Takahara 2011) seem to fit satisfactorily the observed emissions for various late time pulsar wind nebulae without adding any hadronic injection. We will thus focus on the emission produced for winds dominated by a leptonic component at the termination shock.

Note that if protons are energetically dominant in the wind, Amato et al. (2003) calculated that a large flux of neutrinos, gamma-rays and secondary pairs from p-p pion production should be expected from Crab-like pulsar wind nebulae around a few years after the supernova explosion. They estimate that the synchrotron emission from secondaries will be negligible, while TeV photon and neutrino emission could be detectable by current instruments if such young objects were present in our Galaxy.

Only 1% of the relativistic ions and magnetic fields components of the wind can be converted into thermal energy in the ejecta (Chevalier 1977). This fraction can be amplified in presence of, e.g., Rayleigh-Taylor mixing, or high energy cosmic ray diffusion

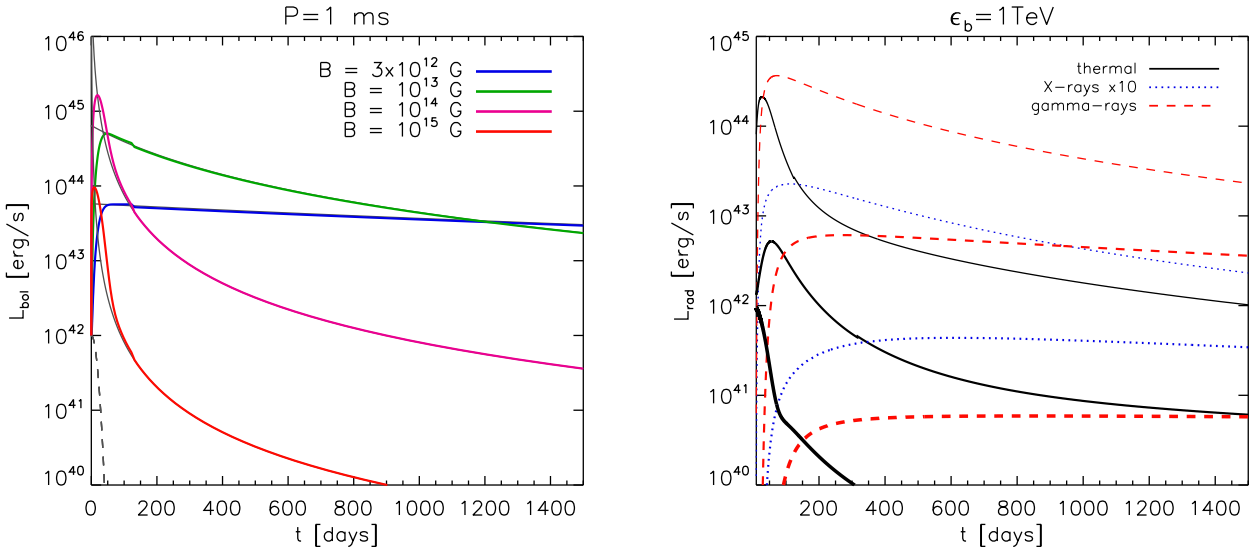

Figure 6.1.: Left: *Evolution of the bolometric radiated luminosity of the supernova as a function of time. The pulsar has a dipole magnetic field of increasing strength as indicated, and period* $P_{\rm i} = 1\,ms$. *The supernova ejecta has* $M_{\rm ej} = 5\,M_\odot$ *and* $E_{\rm ej} = 10^{51}$ *erg. The gray lines give the evolution of the pulsar luminosity* $L_{\rm p}$ *for each initial spin period. The gray dashed lines are the contribution of the ordinary core-collapse supernova to the radiated luminosity* $L_{\rm SN}$. *We have assumed* $\eta_\gamma = 1$. *The slight discontinuity is due to the numerical calculation of the integral in Eq. (C.10), and marks the transition between* $t < t_{\rm thin}$ *and* $t > t_{\rm thin}$. Right: *Thermal emission (black solid lines), non thermal X-ray emission (blue dotted) emitted at energy varying between* $100\,{\rm keV} - 1\,{\rm GeV}$ *for* $\epsilon_{\rm b} = 1$ *TeV, and non thermal gamma-ray emission (red dashed) at 1 TeV, expected from a SN ejecta with* $M_{\rm ej} = 5\,M_\odot$ *and* $E_{\rm ej} = 10^{51}$ *erg* s^{-1}, *embedding a pulsar with dipole magnetic field of* $B = 10^{13}$ *G and period* $P_{\rm i} = 1, 3, 10$ *ms (increasing thickness), assuming* $\eta_B = 0.01$, $\eta_e = 1 - \eta_B$, *and a break energy* $\epsilon_{\rm b} = 1$ *TeV. Caution: for visibility, the X-ray luminosity is multiplied by 10.*

into the ejecta.

Pair injection in the PWN

According to the original idea by Kennel & Coroniti (1984a), the pair injection spectrum into the pulsar wind nebula should present a Maxwellian distribution due to the transformation of the bulk kinetic energy of the wind into thermal energy, and a non-thermal power-law tail formed by pairs accelerated at the shock. Hybrid and PIC simulations have shown indeed such a behavior (e.g., Bennett & Ellison 1995; Dieckmann & Bret 2009; Spitkovsky 2008). Spitkovsky (2008) finds that 1% of the particles are present in this tail, with 10% of the total injected energy. The bulk of the particle energy would then be concentrated around the kinetic energy upstream of the termination shock

$$\epsilon_{\rm b} = kT_{\rm e} = \gamma_{\rm w} m_{\rm e} c^2 \quad (6.1)$$

$$\sim 5 \times 10^{11}\,{\rm eV}\,\frac{\gamma_{\rm w}}{10^6}\,, \quad (6.2)$$

with $\gamma_{\rm w}$ the Lorentz factor of the wind. The non-thermal tail would start around $\epsilon_{\rm b}$ and continue up to higher energies with a spectral index $\gtrsim 2$. In practice, from a theoretical point of view, Lorentz factors as high as $\gamma_{\rm w} \sim 10^6$ are difficult to reach, and current simulations are only capable of producing $\gamma_{\rm w}$ of order a few hundreds (Spitkovsky 2008; Sironi & Spitkovsky 2009).

However, observationally, various authors (Kennel & Coroniti 1984a, but also more recently, e.g., Gelfand et al. 2009; Fang & Zhang 2010; Bucciantini et al. 2011; Tanaka & Takahara 2011) demonstrated that the non-thermal radiation produced by the injection of either one single power-law or a broken power-law peaking around $\epsilon_{\rm b} \sim 1\,{\rm TeV}$, and extending up to PeV energies, could fit successfully the observed emission of various young pulsar wind nebulae. Such a high break energy implies either a high Lorentz factor for the wind $\gamma_{\rm w} \sim 10^{5-6}$, or an efficient acceleration mechanism enabling particles to reach $0.1 - 1\,{\rm TeV}$ energies. At higher energies, another acceleration mechanism has to be invoked to produce particles up to PeV energies. Bucciantini et al. (2011) discuss that $\epsilon_{\rm b}$ could possibly be viewed as a transition energy between Type II and Type I

Fermi acceleration from low at high energies. This would provide a physical explanation to the broken power-law shape, and alleviate the issue of the high wind Lorentz factor. At high energies, acceleration could also happen in the course of reconnection of the striped magnetic field in the wind, at the termination shock (Lyubarsky 2003; Pétri & Lyubarsky 2007). However, it is not clear yet whether this process can lead to a non-thermal particle distribution. One can expect additional particle acceleration in the wind itself, via surf-riding acceleration (Chen et al. 2002; Contopoulos & Kazanas 2002; Arons 2002, 2003). This non-thermal component would not necessarily be processed when injected at the shocks if the particle Larmor radii are large compared to the size of the shock.

In the following, we will assume that pairs are injected in the pulsar wind nebula following a broken power-law of the form

$$\frac{\mathrm{d}\dot{N}}{\mathrm{d}\epsilon}(\epsilon,t) = \frac{\eta_{\mathrm{e}} L_{\mathrm{p}}(t)}{\epsilon_{\mathrm{b}}^2} \begin{cases} (\epsilon/\epsilon_{\mathrm{b}})^{-\alpha} & \text{if} \quad \epsilon_{\mathrm{min}} \leq \epsilon < \epsilon_{\mathrm{b}} \\ (\epsilon/\epsilon_{\mathrm{b}})^{-\beta} & \text{if} \quad \epsilon_{\mathrm{b}} \leq \epsilon \leq \epsilon_{\mathrm{max}} \end{cases} \tag{6.3}$$

where $\alpha < 2 < \beta$, ϵ_{min} and ϵ_{max} are the minimum and maximum cut-off energies respectively, and ϵ_{b} the peak of the injection distribution $\epsilon(\mathrm{d}N/\mathrm{d}\epsilon) \sim 0.1 - 1\,\mathrm{TeV}$. It is commonly assumed that $\epsilon_{\mathrm{b}} \propto \gamma_{\mathrm{w}} \propto \sqrt{L_{\mathrm{p}}(t)}$, but such an assumption would imply very high wind Lorentz factors ($> 10^9$) at early times, that seem incompatible with the simulations and theoretical models discussed above. It is likely that the Lorentz factor experiences a saturation above a certain value, and for simplicity, we will assume that ϵ_{b} is constant over time. For our purpose of deriving a rough estimate of the fraction of high energy emission that can escape the ejecta at early times, such an approximation will suffice. A thorough calculation of the emission spectrum would require time-dependent energy loss calculations for particles beyond the one zone approximation that we use here. Del Zanna et al. (2004, 2006) have shown indeed that the high energy emission is strongly affected by the details of the flow dynamics just downstream of the termination shock.

Radiation by accelerated pairs

The bulk of the electron distribution will predominantly radiate in synchrotron and experience inverse Compton (IC) scattering off the produced synchrotron photons. Inverse Compton scattering off the thermal photons of the ejecta and off the Cosmic Microwave Background (CMB) are negligible compared to the former two processes. The cooling timescale of IC scattering off the thermal photons of the SN ejecta is also much longer than the timescale for self-comptonization of the synchrotron emission. This estimate includes only the contribution of the thermal photons of the standard supernova ejecta, as the thermalization of the non-thermal components described here happen on larger timescales, in the optically thin regime which is of interest to us.

The synchrotron cooling timescale of accelerated electron reads

$$t_{\mathrm{syn}} = \frac{3 m_e^2 c^3}{4 \sigma_{\mathrm{T}} \epsilon_{\mathrm{c}} U_B} \ , \tag{6.4}$$

with $U_B = B_{\mathrm{PWN}}^2/8\pi$. At the early stages that we consider here, the characteristic energy of radiating particles is $\epsilon_{\mathrm{c}}(t) = \epsilon_{\mathrm{b}}$. The characteristic synchrotron radiation frequency can be expressed

$$\nu_{\mathrm{c}}(t) = 0.29 \frac{3 e B_{\mathrm{PWN}}(t)}{4\pi m_e^3 c^5} \epsilon_{\mathrm{c}}^2 \ . \tag{6.5}$$

Accelerated electrons also scatter off these synchrotron photons by IC, producing photons at energy

$$\nu_{\mathrm{IC}} = \nu_{\mathrm{KN}} \equiv \frac{m_e c^2}{\gamma_e h} \quad \text{if } \nu_{\mathrm{c}} > \nu_{\mathrm{KN}} \ , \tag{6.6}$$

$$= \nu_{\mathrm{c}} \quad \text{if } \nu_{\mathrm{c}} \leq \nu_{\mathrm{KN}} \ , \tag{6.7}$$

with a cooling timescale

$$t_{\mathrm{IC,syn}} = \frac{3 m_e^2 c^4}{4 \sigma_{\mathrm{T}} c \epsilon_{\mathrm{c}} U_{\mathrm{syn}}} \ , \tag{6.8}$$

where U_{syn} is the synchrotron photon energy density. Electrons radiate in synchrotron and self-compton processes with the following power ratio: $P_{\mathrm{IC}}/P_{\mathrm{syn}} = U_{\mathrm{syn}}/U_B$. Assuming that the energy of the accelerated electron population is concentrated in its peak energy ϵ_{b}, this implies synchrotron and IC luminosities of $L_{\mathrm{syn}} = \eta_B \eta_e/(\eta_B + \eta_e) L_{\mathrm{p}}$ and $L_{\mathrm{IC}} = \eta_e^2/(\eta_B + \eta_e) L_{\mathrm{p}}$ respectively. Obviously, the value of η_B has an impact on the synchrotron emission, but not on the IC emission.

The IC radiation is mostly emitted at the break energy of the injection of electrons. The synchrotron emission spans from gamma/X-ray (until a few years) to optical wavelengths (after thousands of years). At the time of interest in this study, X-rays are thus mainly emitted between $0.1 - 100\,\mathrm{keV}$ for $\epsilon_{\mathrm{b}} = 0.1\,\mathrm{TeV}$, and around $100\,\mathrm{keV} - 1\,\mathrm{GeV}$ for $\epsilon_{\mathrm{b}} = 1\,\mathrm{TeV}$.

6.1.3. Thermalization in the ejecta

The X-ray opacity ($\sim 0.1 - 100\,\mathrm{keV}$) is dominated by photoelectric absorption in metals. Above $\sim 100\,\mathrm{keV}$,

very hard X-rays and gamma-rays experience predominantly Compton scattering, and pair production above $\sim 10\,\mathrm{MeV}$. The opacities of these processes for various atomic media are given in Fig. 6.2[1]. At a given time t, the optical depth of the ejecta to the characteristic synchrotron photon emission ν_c reads

$$\tau_\mathrm{syn}(t) = v_\mathrm{ej} t \kappa_{\nu_\mathrm{c}}(t) \rho_\mathrm{SN}(t) \ , \tag{6.9}$$

where ρ_SN is the ejecta matter density as in Eq. (3.9). The dominant thermalization process for the TeV IC radiation is pair production by $\gamma - \gamma$ interactions. The timescale for thermalization via this process is however slightly longer than the dynamical time; hence the ejecta appears mostly optically thin to this radiation. We note τ_IC for the optical depth of the ejecta to the IC emission.

The luminosity in the characteristic energies $h\nu_\mathrm{c}$ and $h\nu_\mathrm{IC}$ after thermalization, noted respectively $L_\mathrm{X}(t)$ and $L_\gamma(t)$, and the luminosity in thermal photons, $L_\mathrm{th}(t)$, are calculated as follows

$$L_\mathrm{X}(t) = L_\mathrm{syn}(\nu_\mathrm{c}, t)\, e^{-\tau_\mathrm{syn}(t)} \tag{6.10}$$

$$L_\gamma(t) = L_\mathrm{IC}(\nu_\mathrm{IC}, t)\, e^{-\tau_\mathrm{IC}(t)} \tag{6.11}$$

$$L_\mathrm{th}(t) = L_\mathrm{rad}(t) - L_\mathrm{X}(t) - L_\gamma(t) \ . \tag{6.12}$$

The right hand panel of Figure 6.1 presents the thermal emission (black), X-ray emission (blue dotted) at $h\nu_\mathrm{c} \sim 0.1 - 100\,\mathrm{keV}$ for $\sim 100\,\mathrm{keV} - 1\,\mathrm{GeV}$ for $\epsilon_\mathrm{b} = 1\,\mathrm{TeV}$, and 1 TeV gamma ray emission (red dashed) expected from a SN ejecta with $M_\mathrm{ej} = 5\,M_\odot$ and $E_\mathrm{ej} = 10^{51}\,\mathrm{erg\,s^{-1}}$, embedding a pulsar with dipole magnetic field of $B = 10^{13}\,\mathrm{G}$ and period $P_\mathrm{i} = 1, 3, 10\,\mathrm{ms}$ (increasing thickness), assuming $\eta_B = 0.01$, $\eta_e = 1 - \eta_B$, and a break energy $\epsilon_\mathrm{b} = 1\,\mathrm{TeV}$.

A decrease in flux is expected in the thermal component after a few months to years, when the ejecta becomes optically thin to gamma-rays. For a lower break energy ($\epsilon_\mathrm{b} = 0.1\,\mathrm{TeV}$) we showed in Kotera et al. (2013) that the thermal component can then recover, as the X-ray emission vanishes, because of the increase of the ejecta optical depth for lower energy photons. One robust result is that, in both break energy cases, for fast pulsar rotation periods $P_\mathrm{i} \leq 3\,\mathrm{ms}$, the associated gamma-ray flux around $0.1 - 1\,\mathrm{TeV}$ emerges at a level that should be detectable at a few tens of Mpc, and remains strong over many years.

[1]From http://henke.lbl.gov/optical_constants/ for $30\,\mathrm{eV} \leq h\nu < 1\,\mathrm{keV}$ and http://physics.nist.gov/cgi-bin/Xcom/ for $1\,\mathrm{keV} \leq h\nu < 100\,\mathrm{GeV}$.

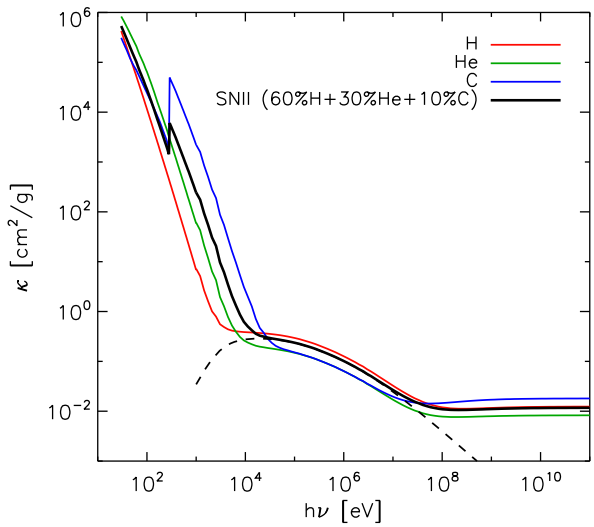

Figure 6.2.: *Atomic scattering opacities of high energy photons on H, He, C, and a mixture of composition mimicking that of a type II core-collapse supernova ejecta (60% H, 30% He and 10% C). The black dashed line indicates the contribution of Compton scattering in the latter composition case.*

6.1.4. Discussion, conclusion

We have estimated in this section the thermal and non thermal radiations expected from supernova ejectas embedding pulsars born with millisecond periods, concentrating at times a few years after the onset of the explosion. The bolometric light curves should present a high luminosity plateau (that can reach $> 10^{43}\,\mathrm{erg/s}$) over a few years. A more detailed emission calculation considering the acceleration of leptons in the pulsar wind nebula region shows that an X-ray and a particularly bright TeV gamma-ray emission (of magnitude comparable to the thermal peak) should appear around one year after the explosion. This non thermal emission would indicate the emergence of the pulsar wind nebula from the supernova ejecta.

The light curves calculated in this paper are simple estimates, that do not take into account second order effects of radioactive decay of ^{56}Ni, recombination, etc. (see, e.g., Kasen & Woosley 2009). The non-thermal components are also evaluated assuming that all the leptonic energy is concentrated in one energy bin. A more detailed analysis should be conducted, taking into account the shape of the spectra and its evolution in time, in order to get a more accurate representation of the emission, and for a thorough comparison with observational data. Depending on

the spectral indices, a non monoenergetic electron injection spectrum could lead to a decrease of the peak luminosity of one order of magnitude.

Our computation of the evolution of the PWN (radius, magnetic field) is also basic, and could benefit from more thorough estimations. Our toy model suffices however in the scope of this study, where the aim is to demonstrate the importance of multi-wavelength follow ups of SN lightcurves. We also assumed a relatively high magnetization η_B of the wind at the termination shock, following estimates that reproduce the features of the Crab nebula (Komissarov & Lyubarsky 2004; Del Zanna et al. 2004).

Several earlier works treat some of the aspects invoked above in more detail. For example, in the context of evolution of pulsar wind nebulae, early works by Pacini & Salvati (1973); Rees & Gunn (1974); Bandiera et al. (1984); Weiler & Panagia (1980); Reynolds & Chevalier (1984) take into account the detailed evolution of particle energy distribution and radiation spectrum. Most of these works aim at calculating radiation features of observed plerions, a few hundred of years after the explosion. However, their modeling at earlier times, especially in the work of Reynolds & Chevalier (1984), lays the ground for the more detailed calculations that should be performed in our framework.

The level of synchrotron emission predicted here can thus be viewed as optimistic values. However, the gamma-ray flux that is predicted does not depend on the magnetization, and remains fairly robust to most parameter changes.

Currently, only a handful of supernovae have been followed over a period longer than a year, and no object, except for SN 1987A, has been examined in X-rays or TeV gamma-rays a year after the explosion. Among the objects that have been followed in optical bands, SN 2003ma (Rest et al. 2011) has an abnormally bright luminosity at the peak, and a long bright tail over many years. The six type II supernovae followed by Otsuka et al. (2012) present various shapes of light curves, and a cut-off in the thermal emission after a few years. Our study demonstrates that the features in these light curves could also be due to the energy injection from the pulsar, that could compete with the other processes that are more commonly considered, such as the light echo of the peak luminosity, or the radioactive decay of ^{56}Ni. An associated X-ray and TeV gamma-ray emission emerging around a few months to a year after the explosion would constitute a clear signature of pulsar rotational energy injection. It is also interesting to note that the emergence of a pulsar wind nebula has been recently reported from radio observations for SN 1986J (Bietenholz et al. 2010), though over longer timescales than predicted for the objects studied in this paper.

Some authors (Murase et al. 2011; Katz et al. 2011; Svirski et al. 2012) have discussed that shock breakouts from stars surrounded by a thick wind could lead to bright X-ray peak after a few months, similar to the signal discussed in this paper. This degeneracy can be overcome by the observation of the gamma-ray signal, which should be absent in the shock breakout scenario. Detailed analysis of the respective X-ray spectra should also help distinguish the two scenarios.

The follow up of bright type II supernovae over a few years after the explosion in different wave bands would thus reveal crucial information on the nature of the compact remnant. These suveys should be made possible with the advent of optical instruments such as LSST, and the use of powerful instruments for transient event detection, such as the Palomar Transient Factory or Pan-STARR. The bright X-ray signal should be detected by NuSTAR for supternovae out to redshifts $z \sim 0.5$, and the even brighter gamma-ray signal could be observed by HESS2, by the future Cerenkov Telescope Array (CTA), and by HAWC which will be the choice instrument to explore the transient sky at these energies. For CTA, an adequate survey of the sky outside the Galactic plane could spot gamma-ray sources of luminosity 10^{43} erg/s as predicted by this work within a radius of ~ 150 Mpc (G. Dubus, private comm.). Assuming a gaussian pulsar period distribution centered around 300 ms as in Faucher-Giguère & Kaspi (2006), implies that 0.3% of the total population has spin periods < 6 ms. With this estimate, one could find 4 bright sources within 150 Mpc. This is consistent with the numbers quoted in early works by Srinivasan et al. (1984); Bhattacharya (1990). These authors estimated the birthrate of Crab-like pulsar-driven supernova remnants to be of order 1 per 240 years in our Galaxy.

Pulsars born with millisecond periods embedded in standard core-collapse supernova ejectas, as described in this paper, are promising candidate sources for ultrahigh energy cosmic rays (Fang et al. 2012, 2013b). In the framework of UHECRs, an injection of order 1% of the Goldreich-Julian density into ions would suffice to account for the observed flux, assuming that 1% of Type II supernovae give birth to pulsars with the right characteristics to produce UHECRs (i.e., pulsars born with millisecond periods and magnetic fields $B \sim 10^{12-13}$ G, Fang et al. 2012).

The observation of the peculiar light curves predicted here could thus provide a signature for the production of UHECRs in these objects. Though no spatial correlation between arrival directions of UHECRs and these supernovae is expected (because of time delays induced by deflections in magnetic fields), an indication of the birth rate of these supernovae could already give direct constraints on this source model. Photo-disintegration and spallation of accelerated nuclei in the supernova ejecta could also lead to an abundant high energy neutrino production (Murase et al. 2009 consider such a neutrino production in the case of magnetars instead of fast-rotating pulsars), that could be detected with IceCube, and correlated with the position of identified peculiar supernovae.

6.2. Effects of millisecond pulsar winds on binary companions

Phinney, E. S., & Kotera, K. in prep.

Millisecond pulsars with evaporating $0.01 - 0.03\,M_\odot$ remnant companions and orbital periods of $2 - 15$ hours are known as "black widow pulsars". Similar systems with M-dwarf[2] companions have recently been discovered, and christened "redback pulsars". These systems offer a unique opportunity to understand the nature of pulsar winds. The companions in many of these systems are observed to be hotter on the pulsar-facing side of the companion, so the companion is acting as a 'beam dump' for the pulsar wind.

Until very recently, the study of the irradiation of companion white dwarf atmospheres by pulsar winds had not attracted much attention, due to the scarcity of observations. A detailed theoretical investigation of such interactions would have today an especially large impact. Indeed, radio follow-up of gamma-ray sources identified by the Fermi gamma-ray satellite has led to an explosion in the number of these close binary systems: several are listed in Roberts (2011), and a more recent list (Ransom, personal communication) contains 18 such objects, among which only 3 are not detected by Fermi. Fermi has discovered many single millisecond pulsars, and major campaigns of multi-wavelength follow-up (radio, infrared, optical, X-ray) have begun. It is timely to begin to prepare a deeper theoretical understanding, and quantitative models of the pulsar wind interaction with the companions.

[2]M-dwarfs are small and relatively cool stars of the main sequence, of M spectral type, also called "red dwarfs".

In most of these systems, the pulsar wind impinges a substantial irradiative flux on its companion. It is thus theoretically expected that the white dwarf be heated and show a strong day/night variation. Phinney et al. (1988) made this prediction shortly after the discovery of the original black-widow pulsar B1957+20, and the expected orbital modulation of the thermal emission from the companion was quickly observed by Fruchter et al. (1990). Recent data from Reynolds et al. (2007) and van Kerkwijk et al. (2011) shows that most of the expected pulsar wind flux is indeed absorbed and reradiated. This is also the case for the similar system PSR J2051-0827 (Stappers et al. 1996, 1999). By contrast, the companion to PSR J0751+1807 did not behave as expected. If all the wind flux were promptly absorbed and reradiated, back of the envelope calculations state that the dayside bolometric flux should be about twice the night-side one. In fact there is no detectable modulation of the flux (Bassa et al. 2006).

The idea of constraining the bulk Lorentz factor of the pulsar wind and the shock geometry in the compact pulsar wind nebula scenario for gamma-ray binaries by computing the unshocked wind emission and comparing it to observations was investigated by Dubus (2006a,b); Dubus et al. (2008); Cerutti et al. (2008, 2010) (see also Dubus 2013 for a review on the gamma-ray emission of binary systems). These authors concentrated on pulsars with main-sequence binary companions and on mostly leptonic winds.

We explore in this section the effects of a relativistic pulsar wind on its companion, for black widow and redback pulsar binary systems. We concentrate on the case where the electromagnetic energy of the wind has been transferred into kinetic energy at an earlier stage, before it interacts with the companion atmosphere. A careful calculation of the energy deposition in the atmosphere by relativistic particles is necessary because the emission profiles depend on how deep the heating is (first if it is below the photosphere, and second if the thermal timescale from the heating depth is longer or shorter than the rotation period. Since the photospheric opacity of the companions varies by several orders of magnitude over the observed range of $T_{\rm eff}$ (and the particles arrive at a range of angles), comparisons of the photospheric spectra between systems can in principle determine the amount of heat deposition with depth, constraining or determining the energy distribution and composition of the pulsar winds. The depth of the heating is also important to determining the level of mass loss from the companion due to the wind thermally driven by the heating. By compar-

ing the sources with many companion masses and temperatures (hence a range of atmospheric column densities), we could constrain the particle composition and energy of the pulsar winds irradiating them.

6.2.1. Irradiation of companions: analytical estimates

Most numerical applications in this section assume values close to those observed for PSR 1957+20. The wind, when it reaches the companion, could be composed of electromagnetic energy, leptons or ions. In this study, we concentrate on the two latter cases.

Energy flux of pulsar winds intercepted by the companion

The energy loss rate of a pulsar with moment of inertia I, rotation period Ps, and period derivative $\dot{P}$ reads (e.g., Shapiro & Teukolsky 1983 – rewriting Eq. A.5):

$$\dot{E}_{\rm R} = I(2\pi)^2 \frac{\dot{P}}{P^3} \sim 3.9 \times 10^{35}\,{\rm erg\,s^{-1}}\, I_{45} \dot{P}_{-20} P_{-3}^{-3} \ . \tag{6.13}$$

The energy flux in the pulsar wind at distance r large compared to the pulsar light cylinder radius, $R_{\rm L} = cP/(2\pi) \sim 4.8 \times 10^8\,{\rm cm}$, can then be written (Arons & Tavani 1993):

$$F_{\rm w} = \frac{\dot{E}_{\rm R}}{4\pi f_{\rm p} r^2} = \frac{I\pi}{f_{\rm p} r^2} \frac{\dot{P}}{P^3} \ , \tag{6.14}$$

where we noted $f_{\rm p} = \Delta\Omega_{\rm p}/(4\pi)$ the fraction of the sky into which the pulsar wind is emitted[3].

The companion can intercept a fraction f of this flux, provided that it falls in the wind beam. We note the semi-major axis of the companion orbit $a = 0.6 R_\odot (P_{\rm b}/{\rm hr})^{2/3} (M/1.5 M_\odot)^{1/3}$, with $P_{\rm b}$ the binary period in hours. The characteristic age of the pulsar is noted $\tau_{\rm c} = P/2\dot{P}$. A low-mass white dwarf, not externally heated, will cool to a temperature $T_{\rm eff} \sim$ a few $10^3\,{\rm K}$ in $1-10\,{\rm Gyr}$. The ratio of the incident flux in the pulsar wind on the "day" side of the companion to the natural cooling flux on the "night" side would thus be

$$\begin{aligned} f_e &= \frac{f F_{\rm W}}{\sigma_{\rm T} T_{\rm eff}} \\ &\sim 2 \times 10^3 f f_{\rm p} P_{-3}^{-2} \tau_{\rm c,Gyr}^{-1} M_{1.5}^{-2/3} \\ &\quad \times \left(\frac{P_{\rm b}}{1{\rm hr}}\right)^{-4/3} \left(\frac{T_{\rm eff}}{4 \times 10^3\,{\rm K}}\right)^{-4} \ , \end{aligned} \tag{6.16}$$

where we have assumed an isotropic wind emission, and a full interception fraction for the numerical estimate.

Particle acceleration in pulsar winds

As has been discussed throughout this thesis and in particular in Appendix B, the combination of the strong magnetic moment and fast rotation induces voltage drops across the pulsar wind. This enables particles of charge Z and mass number A experiencing a fraction $\eta = 0.3\,\eta_3$ (as in the Crab) of these voltage drops to be accelerated to Lorentz factor:

$$\gamma = \eta \frac{Ze}{m_{\rm i} c^2} \Phi \sim 6.9 \times 10^5 \frac{Z}{A} (I_{45} \dot{P}_{20} P_3^{-3})^{1/2} \ . \tag{6.17}$$

Energy losses

In principle, ions accelerated in the wind should not experience major energy losses before reaching the white dwarf atmosphere. Indeed, using Eqs. (6.14) and (6.15), one can calculate the intensity of the magnetic field at a distance r from the pulsar:

$$\begin{aligned} B &= \left(\frac{\sigma}{1+\sigma} \frac{\dot{E}_{\rm R}}{c f_{\rm p} r^2}\right)^{1/2} \\ &\sim 36 \left(\frac{\sigma}{1+\sigma} \frac{1}{f_{\rm p}}\right)^{1/2} (I_{45} \dot{P}_{20} P_3^{-3})^{1/2} \frac{a_{11}}{r}\,{\rm G} \ , \end{aligned} \tag{6.18}$$

where $a_{11} = a/10^{11}\,{\rm cm}$ is the orbital separation. The Larmor radius of ions in this magnetic field, at distance r from the pulsar, then reads:

$$r_{\rm L} = 1.8 \times 10^{10}\, Z \eta_3 \frac{r}{a_{11}} \left(\frac{1+\sigma}{\sigma} f_{\rm p}\right)^{1/2} {\rm cm} \ . \tag{6.19}$$

Hence, we have $r_{\rm L} \ll a$ and the particles are coupled to the wind. The adiabatic losses are negligible, as the linear acceleration time over a distance r to energy E reads (in the comoving frame): $t_{\rm acc} = Er/(\gamma c e Z \Phi) \sim \eta r/(\gamma c) \sim 1.4 \times 10^{-6}\, \eta_3 (r/a_{11})(A/Z)(I_{45} \dot{P}_{20} P_3^{-3})^{-1/2}\,{\rm s}$ and the wind dynamical time $t_{\rm dyn} = r/(\gamma c)$, yielding $t_{\rm acc} < t_{\rm dyn}$.

Using Eq. (21) of Arons & Tavani (1993), one can demonstrate that $t_{\rm acc} \ll t_{\rm syn}$, thus synchrotron losses are negligible.

[3] Note that $F_{\rm w}$ can also be expressed:

$$F_{\rm w} = \frac{cB^2}{4\pi} \left(\frac{1+\sigma}{\sigma}\right) \ , \tag{6.15}$$

defining $\sigma \equiv B^2/[4\pi\gamma c^2 (N_{\rm i} m_{\rm i} + m_e N_e)]$, the ratio of the magnetic energy flux to the kinetic energy flux, with γ is the Lorentz factor of the flow, as in Section 3.2.2.

However, a bow-shock could form in the region of interaction between the pulsar wind and the evaporated material of its companion. The magnetic field should be enhanced at the shock, and could lead to synchrotron losses for ions if the enhancement is of several orders of magnitude. The trajectory of accelerated particles ions would also be affected, the thickness of the shock (~ 0.1 pc, Gaensler & Slane 2006) being typically larger than the Larmor radius. Particles could then be re-accelerated by Fermi-type processes, though the cooling due to photo-disintegration in the X-ray radiation field of the shock[4] could limit the process.

Electrons on the other hand are bound to cool by radiation losses in the wind magnetic field to

$$\gamma_e = \frac{3}{2}\frac{m_e c^2}{e^{3/2} B_{\rm shock}^{1/2}} . \qquad (6.20)$$

They could also be further accelerated by shock-acceleration at the bow shock, the maximum energy depending again on the radiation losses that they would experience in the shock magnetic field, as well as the Inverse Compton losses.

The detailed computation of these effects are beyond the scope of this study. We assume that a non-negligible fraction of the pulsar rotational energy impinges the companion atmosphere under the form of high energy photons or particles. The details of how these were accelerated is not considered, and the energy reached is left essentially as a free parameter.

Day/night effects and atmosphere heating

From Eq. (6.16), we expect the companions of millisecond pulsars with orbital periods less than about 10 hours to be efficiently heated by the incident pulsar wind. As described in Section 6.2.4, PSR B1957+20. PSR J2051-0827 and PSR 47Tuc W show indeed a clear orbital modulation. By contrast, the companion to PSR J0751+1807, which should have a day-side twice as bright as the night side ($f_e \sim 1$), presents no detectable modulation.

The ratio of the heating column depth to the photospheric column depth: $\xi = \Sigma_{\rm heat}/\Sigma_{\rm phot}$ (see Appendix D for a definition of these quantities) is a useful diagnostic of the expected behavior of companions subject to irradiation. Deep heating ($\xi \gg 1$), which is seen to occur in hot atmospheres (> 4000K), will produce the usual photospheric temperature profile decreasing outwards, leading to the usual absorption lines, but at the new (irradiated) temperature.

Since the heating is seen to be put into regions where the flux is carried by convection, the deep heating can affect the convective stability and thus the atmospheric structure. Enough heating can also lead to an long isothermal region (especially as it occurs in the temperature range where hydrogen is becoming ionized, and the opacity rapidly varying with T) and thus affect the cooling of the white dwarf (Phinney et al. 1988).

Shallow heating ($\xi < 1$), which is seen to occur in cool atmospheres, produces a flat or inverted temperature profile at or above the photosphere, leading to weakening of the lines, or even the appearance of the lines in emission.

6.2.2. Shower development in companion atmospheres

We estimate in this section the heating depth $\Sigma_{\rm heat}$ of the companion atmospheres, as a function of the nature of the primary and its initial energy.

Consider a hadronic shower in hydrogen, initiated by a proton of energy E_0. Very crudely, after the proton has propagated through a mean column density $X_{\rm h} \sim 30\,{\rm g\ cm^{-2}}$, one or more pion pairs are typically formed, with Lorentz factor $\gamma < E_0/m_p$. If there are no further interactions, the $\pi^\pm$ quickly decay to muons and neutrinos, while π^0 decay even more quickly to two photons, initiating an electromagnetic cascade with characteristic radiation column $X_0 \sim 64\,{\rm g\ cm^{-2}}$. The muons are more penetrating, with radiation length $X_\mu \sim 500\,{\rm g\ cm^{-2}}$, and decay after travelling 0.66γ km, typically more than the companion's atmospheric scale height. The created pions and photons continue to create more particles, and the total number thus exponentiates roughly as $N \propto 3^{\Sigma/X_h - 1}$, until $E_0/N < 1$GeV when ionization losses degrade the energy into heat, ending the shower. The column depth at which the heat is mostly deposited is thus approximately

$$\Sigma_{\rm heat,h} \sim X_{\rm h} \ln(E/1{\rm GeV}) . \qquad (6.21)$$

Electromagnetic showers develop similarly, but typically only $e^\pm$ pairs or (bremsstrahlung) photons are produced, and the ionization losses only become important once the energies of electrons in the showers have dropped below $E_{\rm c} \sim 370\,$MeV. The heat is thus deposited roughly at column depth

$$\Sigma_{\rm heat,e} \sim X_0 \ln(E/E_{\rm c}) \pm 0.5 \qquad (6.22)$$

[4] Huang & Becker (2007) measure that the X-ray luminosity of PSR B1975+20 is of order $L_X(0.3-10\,{\rm keV}) \sim 10^{31}$ erg/s.

where the upper sign is for photon-initiated showers and the lower for electron initiated ones.

The photon densities at the depths of atmospheres of interest are low enough that inverse Compton and other photon interactions can be neglected at this crude level.

Numerical treatment

Hadronic, photo-hadronic, and lepto-hadronic cascades can be treated more accurately with GEANT4 up to particle energy $E = 100\,\mathrm{TeV}$. Particles are injected in a beam and propagated in the simulated atmosphere structure, and the energy deposited is recorded at each interaction, for primary and secondary particles.

Particles can be tracked down to an energy E_{cut} that can be set. Below this energy, the particle is considered as "lost" in the atmosphere, and its energy is counted as deposited energy. One can follow a particle of type i down to the energy $E_{\mathrm{cut},i}$ at which its radiation length $X_i(E_{\mathrm{cut},i}) < f_{\mathrm{h}} X_{\mathrm{h}}$, where $X_{\mathrm{h}} \sim 30\,\mathrm{g\,cm^{-2}}$ is the mean radiation length for a hadronic shower initiated by a proton of energy $1\,\mathrm{GeV}$, and $f_{\mathrm{h}} \sim 0.2$. The cut-off energy should then be the minimum cut-off energy among all the particles considered: $E_{\mathrm{cut}} = \min(E_{\mathrm{cut},i})$. The estimates from Physical Reference Data[5] on the radiation lengths as a function of energy for electrons, photons and hadrons lead to $E_{\mathrm{cut}} \sim 0.6\,\mathrm{MeV}$. In practice, our simulations show that the energy deposition does not vary strikingly for different $E_{\mathrm{cut}} < 100\,\mathrm{MeV}$.

Figure 6.3 shows the fraction of the initial energy deposited in the atmosphere, as a function of atmospheric depth, for an initial energy of $E_{\mathrm{i}} = 1\,\mathrm{TeV}$, for three types of primaries: protons (blue solid), electrons (red dashed) and gamma-rays (green dash-dotted). The simulated depths are in agreement with the analytical values found previously, although the relative difference between the depth of electron and proton showers is less pronounced. This difference stems from the detailed treatment of the secondaries in the code.

Figure 6.4 presents the rate of energy deposition for various initial particle energies, for a proton primary. As expected, higher initial particle energies lead to deeper heating. The shower development saturates around $10^3\,\mathrm{g\,cm^{-2}}$ above $E \sim 1\,\mathrm{TeV}$, following the shape of the logarithmic function of Eq. (6.21).

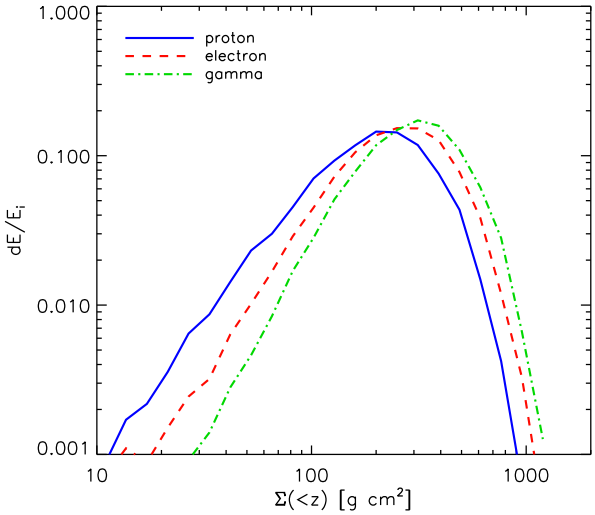

Figure 6.3.: *Fraction of the initial energy deposited in the atmosphere, as a function of atmospheric depth, for an initial energy of $E_{\mathrm{i}} = 1$ TeV, for three types of primaries: protons (blue solid), electrons (red dashed) and gamma-rays (green dash-dotted).*

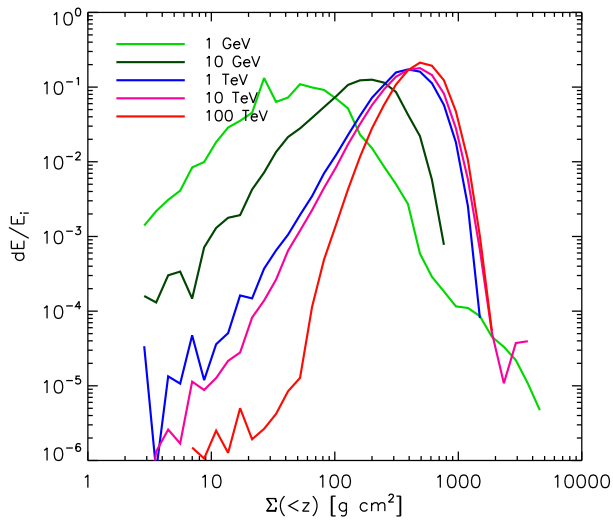

Figure 6.4.: *Fraction of the initial energy deposited in the atmosphere, as a function of atmospheric depth, for various initial energies, for proton primaries. The noise at low energy is due to the limited number of numerical runs.*

[5] http://www.nist.gov/pml/data/

6.2.3. Effects on white dwarf atmospheres

The column density structure of white dwarf hydrogen atmospheres at three temperatures (bracketing the gravity and temperature of PSR J0751+1807's companion) are shown in Figure 6.5. The scale heights of the atmospheres are similar to that of Earth, about 10 km. The atmospheric scale heights at $X_{\rm h}$, for these models are respectively, 0.08 km, 0.36 km, and 15 km for the 2692 K, 4571 K and 7413 K models.

The models were evolved using the code (which includes hydrogen shell-flashes, settling and diffusion) described in Panei et al. (2007), and the atmospheres were computed with the code described in Rohrmann et al. (2002). In each panel, the top (bottom) label corresponds to the top (bottom) curve.

The figure demonstrates that in atmospheres with $T_{\rm eff} > 4000\,{\rm K}$, showers deposit their heat well below the photosphere. In cooler atmospheres (whose opacity is dominated by induced-dipole H_2 interactions and non-ideal effects), most showers deposit their energy near or *above* the photosphere.

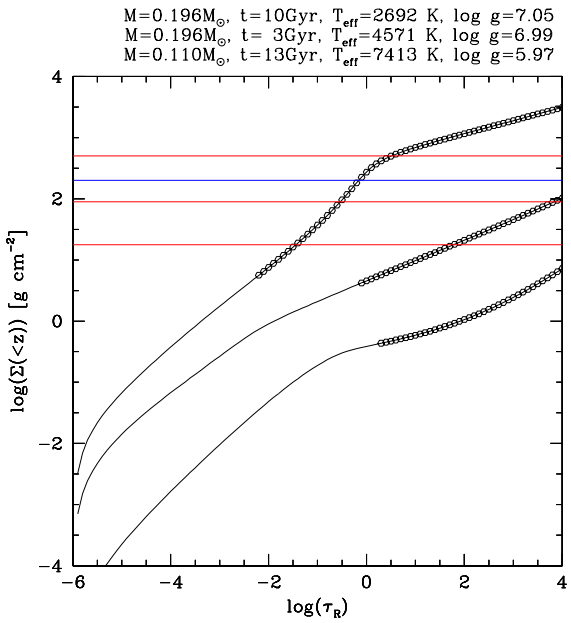

Figure 6.5.: *Column density above points in the atmosphere, as a function of the Rosseland-mean optical depth to those points (i.e. the atmosphere's photosphere is at* $\log(\tau_R) \sim 0$*). Points where more than half the flux is carried by convection are indicated by small circles. The curves, from top to bottom, have effective temperatures of 2692 K, 4571 K and 7413 K, and the gravity g [cm* s^{-2}*] specified in the top label. The blue (second from top) horizontal line indicates* $\Sigma_{\rm heat,h}(E_{\rm i} = 1\,{\rm TeV})$*. The three red horizontal lines (from top to bottom) indicate respectively* $\Sigma_{\rm heat,e}(E_{\rm i} = [1\,{\rm TeV}, 1\,{\rm GeV}])$ *and* $\Sigma_{\rm heat,\gamma}(E_{\rm i} = 1\,{\rm MeV})$ *for a photon primary.*

6.2.4. Comparisons with observations

To date, about 20 black widow and redback systems have been identified, with most of them residing in globular clusters and a handful located in the field. Radio eclipses have been detected in approximately half of the cluster systems and in both of the field systems.

Shortly after the discovery of the original "black widow" pulsar B1957+20 (parameters given in table 6.1), Phinney et al. (1988) predicted a large f_e, and the expected orbital modulation of the thermal emission from the companion was quickly observed by Fruchter et al. (1990). The most recent data, from Reynolds et al. (2007) and van Kerkwijk et al. (2011) shows that most of the expected pulsar wind flux is indeed absorbed and reradiated. This is also the case for the similar system PSR J2051-0827 (see table 6.1; Stappers et al. 1996, 1999).

By contrast, the companion to PSR J0751+1807 (parameters given in table 6.1) has $f_e \sim 1$, so if all the wind flux were promptly absorbed and reradiated, the day-side bolometric flux should be about twice the night-side one. In fact there is no detectable modulation of the flux (Bassa et al. 2006).

All three systems discussed above have degenerate white or brown dwarf companions. The first irradiated system with a non-degenerate companion, PSR J1023+0038, was finally recognised in 2009 (Archibald et al. 2009). As shown in table 6.1, the orbital modulation of the thermal emission from the companion is present, and in fact had been discovered (Thorstensen & Armstrong 2005) several years before the source was recognised as a millisecond pulsar.

PSR J1023+0038 is now considered the prototypical "redback" pulsar. In 2000-2001, the source had emission lines and an accretion disk, which, from the X-ray limits, must have been prevented from reaching the neutron star, likely by the propeller effect. Since 2002, the source no longer has emission lines (i.e. the accretion disk has vanished), but has a millisecond radio and gamma-ray pulsar, optical modulation of the companion on the orbital period, and an X-ray flux modulated on the orbital period (interpreted as emission from the shocked pulsar wind (Arons & Tavani 1993) and likely also on the pulse period (Archibald et al. 2010).

Pulsar	P [ms]	$\dot{E}/10^{34}$ erg s^{-1}	$P_{\rm b}$ [h]	$M_{\rm c}$ [$M_\odot$]	$R/R_{\rm L}$ [K]	f_e [K]	$T_{\rm h}$	$T_{\rm c}$
B1957+20	1.61	11	9.2	0.021	0.7-0.9	0.7	8000	2900
J2051-0827	4.51	0.5	2.4	0.027	0.6	0.5	4500	< 3000
J0751+1807	3.48	0.8	6.3	0.20	0.03	< 0.1	3700	3700
J1023+0038	1.69	~ 5	4.8	0.2	1	> 0.2	6100	5650

Table 6.1.: *Table of pre-Fermi Galactic pulsars with white dwarf or M-dwarf companions. P is the spin period, $\dot{E}$ the spin-down luminosity, $P_{\rm b}$ the binary orbital period, $M_{\rm c}$ the mass of the irradiated companion, $R/R_{\rm L}$ the ratio of the companion radius to the Roche lobe radius, f_e the fraction of an isotropically distributed $\dot{E}$ emitted in orbitally-modulated thermal radiation by the irradiated companion; $T_{\rm h}$ and $T_{\rm c}$ are approximate values of the observationally estimated peak temperature of the hot 'day' side of the companion and the temperature of the cold 'night' side. Sources of data are given in the text.*

Table 6.1 lists the four pre-Fermi system properties. The first three are Galactic "black widow pulsars" with low mass degenerate companions. The fourth is the prototypical "redback pulsar" with a dwarf M star companion. Besides these Galactic systems, a similar, but less well-studied system is known in the globular cluster 47 Tuc, MSP 47 Tuc W (Edmonds et al. 2002). Also of interest is the X-ray millisecond pulsar SAX J1808.4-3657 (Heinke et al. 2008), which should not have shown a hot dayside and a cool night side, but *did*, even though the X-rays in quiescence are not enough to heat the companion. This suggests that there a relativistic wind from the pulsar heats the companion, even though it the system is not observed as a radio pulsar.

Efficient heating in PSRs B1957+20, J2051-0827 companions

Careful spectroscopic study of PSR B1957+20 (van Kerkwijk et al. 2011) has shown that the "deep heating" approximation is remarkably good. There is no evidence for temperature inversions, which would be revealed in emission lines or modification of absorption line profiles. This in great contrast to UV-illuminated companions in pre-CV systems. Almost all the energy flux in the wind of pulsar B1957+20 is clearly penetrating much farther below the photosphere of its companion than would hard UV photons.

This is not qualitatively surprising if only the relativistic particles in the pulsar wind penetrated through the reverse shock into the companion's atmosphere. However, typical pulsar wind models yield ions and pairs with Larmor radii much larger than the ~ 10 km scale height of the white dwarf atmosphere, up to the radius of the companion itself. So non-MHD plasma effects will be important at the shock and contact discontinuity, and could lead to thermal heating of the upper atmosphere. The observed absence of significant high-altitude heating provides a limit to this.

In systems like this, thought to have been spun-up by accretion from a common envelope, the spin axis should be close to perpendicular to the orbit plane. Therefore the companion should be intercepting not the polar wind, but a wind with striped magnetic field (Spitkovsky 2006; Arons 2007; Kalapotharakos & Contopoulos 2009). In the low density environment of an unshocked wind, if the reconnection energy is shared with only a few particles, so high energies can be obtained (Kirk 2004), helping to convert a high σ (ratio of magnetic to particle energy flux) wind to the low one indicated at the scale of pulsar wind nebulae (see review by Kirk et al. 2009). However, when this wind encounters the plasma-loaded atmosphere of the companion, it is suggestive that more of the energy is not dissipated thermally: the wind dynamic pressure of the black widow pulsars matches the pressure of the companion atmosphere at a Rosseland optical depth $\tau_{\rm R} < 10^{-6}$, far above the photosphere. Shocked wind particles would hardly interact at all, but the lack of emission is rather hard to square with the evidence from the radio eclipses (Thompson et al 1994) that the companion has a wind which can be entrained into the pulsar wind.

Lack of modulation in PSR J0751+1807 companion

When the companion's progenitor became radiative at the end of mass transfer, the collapse of the $\sim 0.01 M_\odot$ envelope, presumably initially tidally locked onto the white dwarf would spin the companion up to a rotation period of $5 - 30$ minutes (depending on exactly when tides are assumed to decouple). This rotation period will be substantially less than the thermal time $t_{\rm rad}$ at the heating

depth for incident particles of energies greater than 10 GeV, thus opening the possibility that the reason that modulation is not observed in this system is not that the pulsar wind is not present, but that the companion is not tidally locked, and rotating so rapidly that the modulation is erased (just as the temperature of the Earth's upper atmosphere does not vary much between day and night, since the thermal time is longer than a day).

To go beyond the rough order of magnitude estimates above, more careful calculations must be done. Effects from magnetic fields associated to the companion, particle acceleration at the bow-shock, more accurate modelings of the structure of the companion atmosphere and its evolution once the wind energy is deposited should be taken into account. Of particular interest is whether the distributed heating from the showers from low energy particles, or particles with a range of energies, deposits enough energy in the upper atmosphere to create observable emission lines. These will enable us to use the systems to constrain the controversial pair multiplicities and energies, and compositions of pulsar wind model.

7. Perspectives

Since their discovery more than a hundred years ago, cosmic rays have provided a well of excitement and enigma for particle physicists and astrophysicists, with their colossal energies, and their mysterious extra-solar origins. A connection between cosmic rays and pulsars was suggested in the decades following the discovery of the first pulsar, but was never deeply investigated, in particular at the highest energies. The recent multi-messenger data related to cosmic-rays and the boom in pulsar observations make it timely to dig into this matter now.

We have sketched in this thesis the key issues that cosmic rays raise at various energies, and their possible connections to pulsars. At energies above the knee, we have discussed the potential of pulsar populations to accelerate particles and to reproduce the measured cosmic-ray data. More specifically, we have found that the production of ultrahigh energy cosmic rays in these objects could give a picture that is surprisingly consistent with the latest data from the Auger Observatory.

All energy ranges from 10 GeV to 100 EeV, multi-messengers, and multi-wavelengths should be considered altogether to solve the long-standing mystery of the origins of these high energy charged particles. With the birth of high-energy neutrino astronomy, we stand today at the threshold of an exciting multi-messenger era, where we will cross-correlate neutrino, gamma-ray, and cosmic-ray information in order to understand the workings of the most powerful sources in the Universe. Cosmic rays definitely play a central role in this exploration, as they are at the origin of the other two types of messengers. We have discussed how the signatures associated to a pulsar model can be used as tools to diagnose the nature of pulsars and their winds.

The coming years are expected to be thrilling with the advent of many instruments such as CTA, HAWC, JEM-EUSO, KM3Net, DecaCube, GRAND, which will confirm or exclude our theoretical predictions, enabling us to shape up further the scenarios. Deep un-targeted surveys are being carried out with Palomar Transient Factory, Pan-STARRS, Sky-Mapper, and will be enhanced by the advent of LSST[1]. These will be able to follow a large number of supernovae and ground-breaking observations could be made, that would have important implications for understanding UHECRs, pulsar winds, and core-collapse supernovae. The Square Kilometer Array will shed light on the structure and strength of intergalactic magnetic fields, allowing us to constrain the arrival directions of the high energy particles. On the numerical side, advances in Particle In Cell simulations will likely probe acceleration mechanisms at play in the sources, help identify the producers of UHECRs and investigate the morphology of pulsar winds. Plasma experiments in laboratories could also participate in elucidating the acceleration processes.

The ongoing theoretical endeavor and the numerous instruments planned and in operation ensure that important progress will be made in astroparticle and pulsar physics the next decades.

[1] http://www.lsst.org/lsst/science/scientist_transient

A. Characteristics of millisecond pulsar wind nebulae

We note $M_{\rm ej}$ and $E_{\rm ej}$ as the mass and initial energy of the supernova ejecta. The pulsar has an inertial momentum I, radius $R_\star$, initial rotation velocity $\Omega_{\rm i}$ (corresponding initial period $P_{\rm i} = 2\pi/\Omega_{\rm i}$), and dipole magnetic field B. Numerical quantities are noted $Q_x \equiv Q/10^x$ in cgs units, unless specified otherwise.

The interaction between the pulsar wind and the supernova ejecta leads to the formation of the following structures, illustrated in Fig. A.1: a forward shock at the interface of the shocked and unshocked ejecta, and a reverse shock at the interface between the shocked and unshocked wind (commonly called "termination shock"). The shocked material between the forward and the reverse shock constitutes the pulsar wind nebula (PWN, e.g., Chevalier 1977; Chevalier & Fransson 1992; Gaensler & Slane 2006).

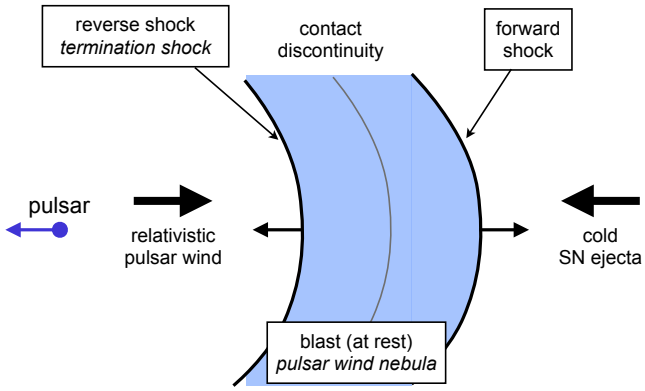

Figure A.1.: *Scheme of the structures created by the interaction between the pulsar wind and the SN ejecta in the blast rest mass frame.*

A.1. Pulsar wind energetics and timescales

The pulsar spins down by electromagnetic energy losses that is transferred to the surrounding environment. The deposition of this energy happens over the spin-down timescale of the pulsar (Shapiro & Teukolsky 1983):

$$t_{\rm EM} = \frac{9Ic^3}{2B^2R_\star^6\Omega_{\rm i}^2} \sim 3.1\times10^7\,{\rm s}\, I_{45}B_{13}^{-2}R_{\star,6}^{-6}P_{\rm i,-3}^2 \ . \tag{A.1}$$

If gravitational wave losses are substantial, the star spins down over a timescale

$$t_{\rm GW} = \frac{5c^5P^4}{2^{10}\pi^4GI\epsilon^2} \sim 1.5\times10^6\,{\rm s}\, P_{\rm i,-3}^4 I_{45}^{-1}\epsilon_{-4}^2 \ , \tag{A.2}$$

with ϵ the ellipticity created by the interior magnetic fields of the star (Usov 1992; Bonazzola & Gourgoulhon 1996; Ostriker & Gunn 1969). Typically $\epsilon = \beta R_\star^8B^2/(4GI^2) \sim 4\times10^{-4}\beta_2R_{\star,6}^8B_{15}^2I_{45}^{-2}$, where β is the magnetic distortion factor introduced by Bonazzola & Gourgoulhon (1996), which measures the efficiency of the interior magnetic field in distorting the star. This factor depends on the equation of state of the star interior and on its magnetic field geometry. Bonazzola & Gourgoulhon (1996) finds that the value of β can range between $1-10$ for perfectly conducting interiors (normal matter), $10-100$ for type I superconductors and can reach $\gtrsim 100$ for type II superconductors (for a detailed study on the connection between magnetars as sources of UHECRs and gravitational waves, see Kotera 2011 and Section 5.3). In the following, we will note

$$t_{\rm p} \equiv (t_{\rm EM}^{-1} + t_{\rm GW}^{-1})^{-1} \ , \tag{A.3}$$

and typically assume $t_{\rm EM} \ll t_{\rm GW}$.

The pulsar wind carries a total energy:

$$E_{\rm p} = \frac{I\Omega_{\rm i}^2}{2} \sim 1.9\times10^{52}\,{\rm erg}\, I_{45}P_{\rm i,-3}^2 \ , \tag{A.4}$$

and injects a luminosity (Shapiro & Teukolsky 1983)

$$L_{\rm w}(t) = \frac{L_{\rm p}}{(1+t/t_{\rm p})^2} \ , \tag{A.5}$$

with initial luminosity $L_{\rm p} = E_{\rm p}/t_{\rm p} \simeq 0.64\times10^{45}P_{-3}^{-4}B_{\star,13}^2R_{\star,6}^6\,{\rm erg/s}$, into the cold supernova ejecta. The evolution of the pulsar luminosity over time, for magnetic dipole spin-down, is represented in Fig. A.2. More specifically, the wind luminosity decreases as $L_{\rm w}(t) = L_{\rm p}/(1+t/t_{\rm p})^{(n+1)/(n-1)}$, in terms of the breaking index n and spin-down time $t_{\rm p}$ on a typical spin-down timescale. For magneto-dipole

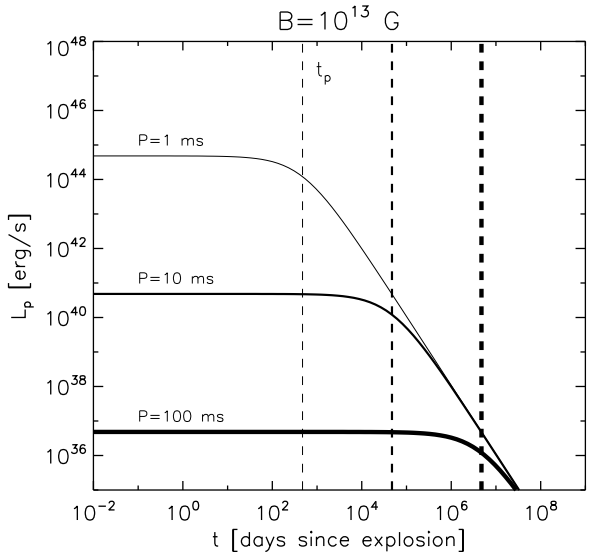

Figure A.2.: *Evolution of the pulsar luminosity L_p as a function of time, for magnetic dipole spin-down. The pulsar has a dipole magnetic field of $B = 10^{13}\,G$, and period $P_\mathrm{i} = 1, 10, 100\,ms$ (increasing thickness). The vertical dashed lines correspond to the spin-down timescale t_p for each intial spin period.*

losses in the vacuum, $n = 3$, while observations rather indicate $n \sim 2 - 2.5$. Nevertheless, we will be interested in the structure of the nebula at time t_p, at which a substantial fraction of the rotational energy has been output into the nebula; the breaking index controls the later evolutionary stages, therefore it will not impact significantly our results. We thus adopt $n = 3$ for simplicity in what follows.

A.2. Pulsar wind nebula radius and magnetic field

For an ordinary core-collapse supernova, the ejecta expands into the circumstellar medium at a characteristic final velocity

$$\begin{aligned} v_\mathrm{ej} &= v_\mathrm{SN} = \left(2\frac{E_\mathrm{ej}}{M_\mathrm{ej}}\right)^{1/2} \\ &\sim 4.5\times10^8\,\mathrm{cm\,s^{-1}}\,E_\mathrm{ej,51}^{1/2}M_\mathrm{ej,5}^{-1/2}\ , \end{aligned} \tag{A.6}$$

where $M_\mathrm{ej,5} \equiv M_\mathrm{ej}/5\,M_\odot$. After a few expansion timescales $t_\mathrm{ex} = R_\mathrm{ej,i}/v_\mathrm{SN}$, where $R_\mathrm{ej,i}$ is the radius of the star that led to the explosion, the ejecta enters into a stage of homologous expansion where its size scales as $R = v_\mathrm{ej}t$.

The characteristic velocity of the ejecta is not affected by the pulsar wind nebula expansion if $E_\mathrm{p} \ll E_\mathrm{ej}$. However, if the pulsar input energy overwhelms the initial ejecta energy $E_\mathrm{p} \gg E_\mathrm{ej}$, the ejecta is swept up into the shell at a final shell velocity $v_\mathrm{f} = (2E_\mathrm{p}/M_\mathrm{ej})^{1/2}$ (Chevalier 2005). Taking into account these two extreme cases, one can estimate the characteristic ejecta velocity as

$$v_\mathrm{ej} = v_\mathrm{SN}(1 + E_\mathrm{p}/E_\mathrm{ej})^{1/2}\ . \tag{A.7}$$

For $E_\mathrm{p} \ll E_\mathrm{ej}$, the evolution of the pulsar wind nebula takes place in the central part of the SN ejecta, where the density profile is nearly flat, with $\rho \propto t^{-3}(r/t)^{-m}$. We will assume here that $m = 0$. For times $t \le t_\mathrm{p}$ where $L_\mathrm{w} \sim E_\mathrm{p}/t_\mathrm{p}$, the radius of the pulsar wind nebula can then be expressed (Chevalier 1977)

$$R_\mathrm{PWN} \sim \left(\frac{125}{99}\frac{v_\mathrm{ej}^3E_\mathrm{p}}{M_\mathrm{ej}t_\mathrm{p}}\right)^{1/5} t^{6/5}\ . \tag{A.8}$$

Beyond the characteristic velocity v_SN, the density profile of the ejecta steepens considerably, reaching spectral indices $b \gtrsim 5$ (e.g., Matzner & McKee 1999). For $E_\mathrm{p} \gg E_\mathrm{ej}$, the pulsar wind nebula expands past this inflection point and its size depends on whether the swept-up shell breaks up by Rayleigh-Taylor instabilities. Chevalier (2005) discusses that if the shell does not break up, the expansion is determined by the acceleration of a shell of fixed mass, thus, for $t \le t_\mathrm{p}$, $E_\mathrm{p} \gg E_\mathrm{ej}$, and no shell disruption

$$\begin{aligned} R_\mathrm{PWN} &= \left(\frac{8}{15}\frac{E_\mathrm{p}}{M_\mathrm{ej}t_\mathrm{p}}\right)^{1/2} t^{3/2} \\ &\sim 2.2\times10^{16}\,\mathrm{cm}\,E_\mathrm{p,52}^{1/2}M_\mathrm{ej,5}^{-1/2}t_\mathrm{p,yr}\ . \end{aligned} \tag{A.9}$$

Otherwise, the evolution of the nebula is set by pressure equilibrium, and $R_\mathrm{PWN} \propto t^{(6-b)/(5-b)}$ (for $t < t_\mathrm{p}$, $E_\mathrm{p} \gg E_\mathrm{ej}$). In the following, because the fate of the shell is unclear at this stage, we will use Eq. (A.9) as an illustration.

For $t > t_\mathrm{p}$, L_p drops, and the swept-up material tends towards free expansion. One can roughly assume the relation

$$R_\mathrm{PWN}(t > t_\mathrm{p}) = R_\mathrm{PWN}(t_\mathrm{p})\frac{t}{t_\mathrm{p}}\ , \tag{A.10}$$

where $R_\mathrm{PWN}(t_\mathrm{p})$ is the size of the pulsar wind nebula in Eqs. (A.8,A.9).

These analytical solutions fail whenever L_w depends on time, e.g. at times $\gtrsim t_\mathrm{p}$, or when radiative cooling of the blast becomes important. The latter

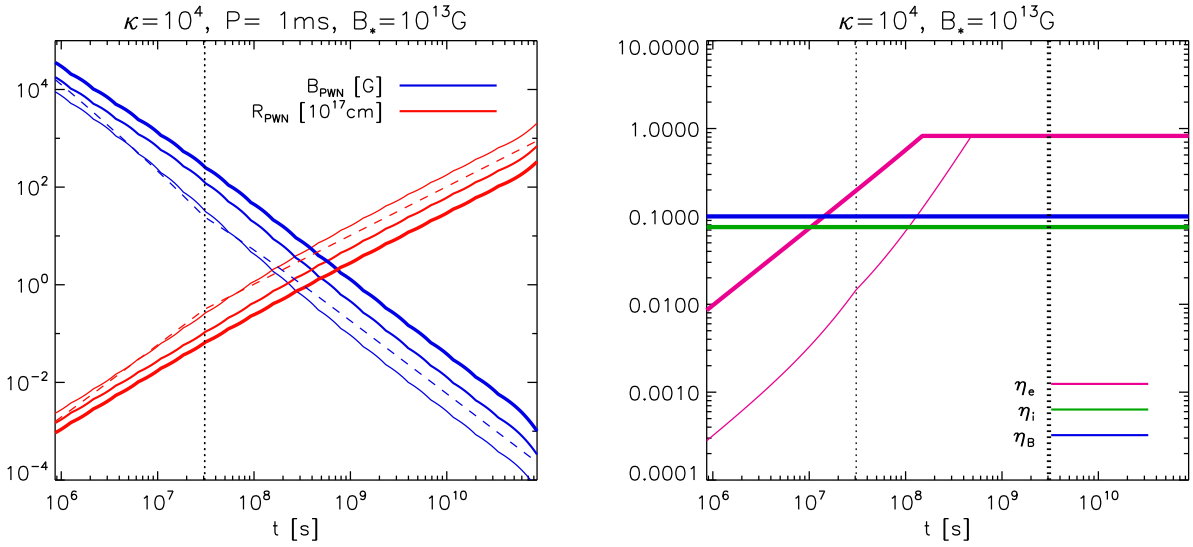

Figure A.3.: *Evolution in time of pulsar wind dynamical quantities, for pulsar dipole magnetic field $B_{\star,13} = 1$, leptonic multiplicity $\kappa_4 = 1$ and assuming $\eta_{\rm B} = 0.1$. Left: Case of a pulsar with initial rotation period $P_{-3} = 1$. Red lines: radius of the nebula (obtained by integrating numerically Eqs. A.11–A.15). Increasing thick lines are for $\eta_{\rm rad} = 0, 0.9, 0.99$. The dashed lines represent the analytical adiabatic case (Eq. A.9). Blue lines: corresponding mean magnetic field in the pulsar wind nebula $B_{\rm PWN}$ (Eq. A.16). Right: Fraction of the pulsar luminosity dissipated into magnetic energy in the nebula (η_B, blue), to leptons (η_e, pink) and to ions ($\eta_{\rm i}$, green). Initial rotation periods $P_{-3} = 1$ (thin lines), and $P_{-3} = 10$ (thick lines). The vertical dotted line indicates the spin-down timescale $t_{\rm p}$.*

possiblity is to be considered, because the electrons cool through synchrotron faster than a dynamical timescale, contrary to what happens in PWNe such as the Crab (Lemoine et al. in prep.). Therefore, if dissipation is efficient, most of the wind luminosity input into the nebula is actually lost into radiation. In order to account for this effect, we use an improved version of Eqs. (A.8,A.9), in which $(1-\eta_{\rm rad})L_{\rm w}$ represents the actual power deposited into the nebula, $\eta_{\rm rad} = 1-\eta_B-\eta_{\rm i}$ representing the fraction of luminosity converted into radiation through pair cooling (η_B: fraction of energy in the magnetic field, $\eta_{\rm i}$: fraction of energy in ions, in the nebula).

These approximations are used to provide analytical estimates of the various quantities characterizing the nebula at time $t_{\rm p}$. Then, we complement these estimates with a detailed numerical integration of the following system:

$$\dot{R}_{\rm PWN} = \beta_{\rm PWN} c \quad (A.11)$$

$$\dot{R}_{\rm es} = \beta_{\rm es} c \quad (A.12)$$

$$\dot{U}_{\rm sw} = (\beta_{\rm w} - \beta_{\rm ts})\, L_{\rm w} - P_{\rm rad} - 4\pi R_{\rm PWN}^2 \beta_{\rm PWN} c\, p_{\rm PWN}, \quad (A.13)$$

$$\dot{M}_{\rm se} = (\beta_{\rm es} - \beta_{\rm ej})\, 4\pi r_{\rm es}^2 \rho_{\rm ej} c, \quad (A.14)$$

$$\dot{U}_{\rm se} = (\beta_{\rm es} - \beta_{\rm ej})\, 4\pi r_{\rm es}^2 \rho_{\rm ej} c^3 + 4\pi R_{\rm PWN}^2 \beta_{\rm PWN} c\, p_{\rm PWN}. \quad (A.15)$$

All quantities are defined in the source rest frame; they are as follows: $R_{\rm PWN}$ corresponds to the radius of the contact discontinuity, interpreted as the size of the nebula; $R_{\rm es}$ represents the location of the outer shock of the nebula, propagating in the supernova remnant; to a very good approximation, $R_{\rm es} \simeq R_{\rm PWN}$ (thin-shell approximation); $\beta_{\rm es}$ consequently represents the velocity of this outer shock while $\beta_{\rm ts}$ denotes the velocity of the termination shock; $U_{\rm sw}$ represents the energy contained in the shocked wind region, beneath the contact discontinuity; $P_{\rm em}$ represents the power lost through radiation; since the electrons cool faster than an expansion timescale (see below), one can write $P_{\rm em} = (1-\eta_B-\eta_{\rm i})\,(\beta_{\rm w}-\beta_{\rm ts})\,L_{\rm w}$, in terms of the fraction of power injected into the nebula in magnetic field (η_B) and ions ($\eta_{\rm i}$). $\beta_{\rm PWN}$ represents the velocity of the pulsar wind nebula in the source rest frame. $p_{\rm PWN}$ represents the pressure inside the nebula, which can be well approximated by $U_{\rm sw}/(4\pi R_{\rm PWN}^3)$ (Bucciantini et al. 2011); the term associated to $p_{\rm PWN}$ consequently represents adiabatic losses for $U_{\rm sw}$; $M_{\rm se}$ denotes the mass accumulated in the shocked ejecta region, between the contact discontinuity and the outer shock; $\beta_{\rm ej}$ corresponds to the velocity of the supernova remnant ejecta, in the source frame; finally, $U_{\rm se}$ denotes the energy contained in the shocked ejecta region. To a good approximation, $U_{\rm se} - M_{\rm se}c^2 \simeq M_{\rm se}\beta_{\rm PWN}^2 c^2/2$ since

the ejecta is non-relativistic.

These equations can be obtained by integrating the equations of particle current density and energy-momentum conservation over the spatial variables, between the boundaries of interest. This procedure introduces the brackets $(\beta_{\rm w} - \beta_{\rm ts})$ for $\dot{U}_{\rm sw}$ and $(\beta_{\rm es} - \beta_{\rm ej})$ for $U_{\rm se}$, which correspond to the fact that the boundaries of the shocked wind and shocked ejecta are delimited by the moving shock waves. The velocity of the termination shock in the source frame depends non-trivially on the degree of magnetization of the shock; for $\sigma_{\rm b} \ll 1$, however, $\beta_{\rm ts} \ll \beta_{\rm w}$ (Kennel & Coroniti 1984b) and $\beta_{\rm w} \simeq 1$, therefore we approximate $\beta_{\rm w} - \beta_{\rm ts} \simeq 1$. For the outer shock, assuming it is strong, non-radiative and non-relativistic, one has $\beta_{\rm es} - \beta_{\rm ej} \simeq 4(\beta_{\rm PWN} - \beta_{\rm ej})/3$. This closes the system.

The dependence on the parameters in this equation are obtained through Eq. (A.9). These values match the numerical evaluation for $\eta_{\rm rad} \lesssim 0.9$. Hereafter, for illustration, we will place ourselves in the adiabatic case: $1 - \eta_{\rm rad} \sim 1$.

The mean magnetic field in the nebula, $B_{\rm PWN}$, is given by

$$\begin{aligned} B_{\rm PWN} &= \left(\frac{6\eta_{\rm B} \int_0^t L_{\rm w}(t')\mathrm{d}t'}{R_{\rm PWN}^3} \right)^{1/2} \\ &\simeq 24\, P_{-3}^{-1} \eta_B^{1/2} R_{\rm PWN,16.5}^{-3/2} I_{45}^{1/2}\, \hat{t}^{-9/4}\ \mathrm{G}\ . \end{aligned} \tag{A.16}$$

η_B denotes the magnetic fraction of the energy injected into the nebula (see Figure A.3), accounting for dissipation, i.e. $\eta_B = \sigma_{\rm PWN}/(1+\sigma_{\rm PWN})$. As mentioned above, we assume $\eta_B \lesssim 1$, corresponding to efficient dissipation of wind luminosity into particle random energies. Figure A.3 presents the evolution in time of pulsar wind dynamical quantities ($R_{\rm PWN}$ and $B_{\rm PWN}$) calculated analytically and by numerical integration. Both results agree for the adiabatic case at the spin-down time. The right panel depicts the evolution of the distribution of the energy fractions $\eta_{\rm i}$, η_e and $\eta_{\rm B}$.

A.3. Energy distribution in the pulsar wind nebula

Electron-positron pairs are injected into the nebula with a bulk Lorentz factor of order unity (if $\sigma_{\rm PWN} \lesssim 1$) and random Lorentz factor noted γ_e, corresponding to the minimum of two values: $\gamma_{\rm diss.}$, corresponding to the random Lorentz factor acquired through dissipation (Eq. 3.2), and $\gamma_{\rm e-loss}$, corresponding to the radiation reaction limiting Lorentz factor through cooling processes during dissipation. Of course, γ_e cannot be lower than the Lorentz factor of the wind at the termination shock, $\gamma_{\rm w}$, which is unknown. We assume that $\gamma_{\rm w} < \min(\gamma_{\rm diss.}, \gamma_{\rm e-loss})$. This is not a strong assumption, since the latter two Lorentz factors are quite large: $\gamma_{\rm diss.} \simeq 2.9 \times 10^8 (1+\sigma_{\rm B})^{-1}(1+x_{\rm i})^{-1}\, \kappa_4^{-1} P_{-3}^{-2} B_{13} R_{\star,6}^3$.

The Lorentz factor $\gamma_{\rm e-loss}$ which limits the acceleration of pairs in dissipation/acceleration processes is:

$$\begin{aligned} \gamma_{\rm e-loss} &= \frac{3}{2} \frac{m_e c^2}{e^{3/2} B_{\rm PWN}^{1/2}} \\ &\simeq 2.4 \times 10^7\, \eta_B^{-1/4} P_{-3}^{1/2} R_{\rm PWN,16.5}^{3/4} I_{45}^{-1/4} \hat{t}^{9/8}\ . \end{aligned} \tag{A.17}$$

In terms of $\gamma_{\rm e-loss}$ and $\gamma_{\rm diss.}$, one can define the fractions of energy η_e and η_i carried by the electrons and the ions in the nebula:

$$\eta_e = \frac{1-\eta_B}{1+x_{\rm i}} \min\left(1, \frac{\gamma_{\rm e-loss}}{\gamma_{\rm diss.}}\right)\ , \quad \eta_i = \frac{(1-\eta_B)x_{\rm i}}{1+x_{\rm i}}\ . \tag{A.18}$$

The quantity η_e is understood to characterize the energy injected in pairs in the nebula, after dissipation/acceleration processes, but before synchrotron cooling has taken place. Clearly, for the above fiducial parameters, $\eta_e \ll 1$ at time $t_{\rm p}$, meaning that most of the energy dissipated into the electrons has been radiated at the radiation reaction limit, producing photons of energy $\sim 50\,$MeV. This radiation does not contribute to the radiation losses of ultra-high energy ions but it may lead to a specific signature of disspation processes in such young PWNe. In contrast, $\gamma_{\rm e-loss} \gg \gamma_{\rm diss.}$ in the Crab nebula, so that the electrons can take away most of the dissipated energy without losing it to radiation.

A.4. Electron synchrotron SED of the pulsar wind nebula

In such compact PWNe, the electrons cool through synchrotron on a timescale that is much shorter than a dynamical timescale, down to non-relativistic velocities, since the cooling Lorentz factor is given by

$$\begin{aligned} \gamma_{\rm c} &\simeq \frac{6\pi m_e c^2 \beta_{\rm PWN}}{\sigma_{\rm T} B_{\rm PWN}^2 R_{\rm PWN}} \\ &\simeq 8.8 \times 10^{-2}\, \eta_B^{-1} P_{-3}^4 \beta_{\rm PWN} B_{13}^{-4} R_{\star,6}^{-12} I_{45}^2 \hat{t}^3\ . \end{aligned} \tag{A.19}$$

This represents a major difference with respect to the case of the Crab nebula, for which most electrons

do not cool on an expansion timescale, due to the smaller amount of energy injected into the wind and to the larger size of the nebula.

The above allows us to characterize the spectral energy distribution (SED) of the nebula; in particular, the low-frequency spectral luminosity is represented by

$$L_{\nu,\mathrm{syn}} \simeq \eta_e L_\mathrm{w} \left(\frac{\epsilon}{\epsilon_e}\right)^{1/2} \quad (\epsilon_\mathrm{c} < \epsilon < \epsilon_e) \tag{A.20}$$

with $\epsilon_\mathrm{c} = h\nu_\mathrm{c}$ and $\epsilon_e = h\nu_\mathrm{e}$ in terms of the synchrotron peak frequencies associated to Lorentz factors γ_c and $\gamma_e = \min(\gamma_{\mathrm{e-loss}}, \gamma_{\mathrm{diss.}})$. In Fig. A.3, we plot the time evolution of the various quantities that characterize the nebula, i.e. the mean magnetic field, the mean nebular radius and the fractions of energy η_e, η_B and η_i.

The number density of the low-frequency synchrotron photons with $\nu < \nu_e$ (that will interact with the accelerated ultrahigh energy cosmic rays) is[1]

$$\epsilon_\gamma \frac{\mathrm{d}n_\gamma}{\mathrm{d}\epsilon_\gamma} \simeq \eta_e \left(\frac{\epsilon_\gamma}{\epsilon_e}\right)^{1/2} \frac{L_\mathrm{w}}{4\pi R_\mathrm{PWN}^2 c\epsilon_\gamma} \quad (\epsilon_\mathrm{c} < \epsilon_\gamma < \epsilon_e) \ . \tag{A.21}$$

[1] for clarity, we assume $1 + x_\mathrm{i} \sim 1$, $1 - \eta_B \sim 1$ in the expressions that follow

B. The unipolar induction toy model

In this Appendix, we recall the classical equations used to describe the acceleration of cosmic rays in pulsars, under the unipolar induction toy model. Section 3.2 and Lemoine et al. (in prep.) gives a more accurate description of the process.

The pulsar has an inertial momentum I, radius $R_\star$, initial rotation velocity Ω_i (corresponding initial period $P_\mathrm{i} = 2\pi/\Omega_\mathrm{i}$), and dipole magnetic field B. Numerical quantities are noted $Q_x \equiv Q/10^x$ in cgs units, unless specified otherwise.

B.1. Voltage drop across pulsar magnetospheres

For isolated pulsars (not recycled binary pulsars) or magnetars, the internal, mainly toroidal magnetic field partially threads the magnetar crust, making up a mainly poloidal magnetosphere with surface dipole strengths $B_\mathrm{d} \sim 10^{11-15}$ G that are required to account for the observed spin-down rates. This dipole component decreases as $B(r) = (1/2)B_\mathrm{d}(R_\star/r)^3$ according to the distance from the star's surface r, with $R_\star$ the radius of the star. Beyond the light cylinder radius

$$R_\mathrm{L} \equiv \frac{c}{\Omega} \,, \tag{B.1}$$

the dipole field structure cannot be causally maintained and the field becomes mostly azimuthal, with field lines spiraling outwards and with strength decreasing as $B(r) \sim B(R_\mathrm{L})(R_\mathrm{L}/r)$. The out-flowing relativistic plasma at $r > R_\mathrm{L}$ (the pulsar or magnetar "wind") thus has in principle magnetospheric voltage drops across the magnetic field of magnitude (Blasi et al. 2000; Arons 2003):

$$\Phi_\mathrm{wind} \sim rB(r) \sim R_\mathrm{L}B(R_\mathrm{L}) = \frac{\Omega^2\mu}{c^2} \tag{B.2}$$

$$\sim 10^{20}\mu_{30.5}\Omega_4^2 \ \mathrm{V} \,, \tag{B.3}$$

where $\mu = B_\mathrm{d}R_\star^3/2 = 10^{30.5}$ cgs $B_{\mathrm{d},13}R_{\star,6}^3$ is the neutron star dipole moment.

B.2. Maximum acceleration energy

In the classical unipolar induction toy-model of cosmic-ray acceleration in pulsars, we assume that particles of charge Z can experience a fraction η of that potential. They can then be accelerated to the initial energy (Blasi et al. 2000; Arons 2003):

$$E_0 = Ze\,\Phi\,\eta = 7\times10^{19}\,\mathrm{eV}\,\eta\,Z\,B_{13}\,P_{\mathrm{i},-3}^{-2} \,. \tag{B.4}$$

Energy losses by gravitational waves and electromagnetic radiation lead to the spin-down of the pulsar (see Shapiro & Teukolsky 1983 and references therein), and thus to the production of particles of lower and lower energies as time goes. The acceleration energy at time t reads

$$E_\mathrm{CR}(t) = E_0\,(1+t/t_\mathrm{p})^{-1} \,, \tag{B.5}$$

where t_p was defined in Eq. (A.3).

B.3. Injected flux

Inside the light cylinder, the magnetosphere corotates with the star and the ion density corresponds to the maximum current density of particles extracted from the star surface, i.e., the Goldreich-Julian charge density. Under the assumption that this density (Goldreich & Julian 1969)

$$\dot{N}_\mathrm{GJ} = \frac{B_\star R_\star^3\Omega^2}{ec} \tag{B.6}$$

is entirely tapped in the outflow for acceleration, one can write the instantaneous particle injection rate $\dot{N}_\mathrm{i}$ as a function of Ω and thus of the particle energy at a given time E. The energy spectrum of the particles accelerated by a magnetar during its spin-down reads:

$$\frac{\mathrm{d}N_\mathrm{i}}{\mathrm{d}E} = \dot{N}_\mathrm{i}\left(-\frac{\mathrm{d}t}{\mathrm{d}\Omega}\right)\frac{\mathrm{d}\Omega}{\mathrm{d}E} \,. \tag{B.7}$$

Using the expression of the pulsar spin-down rate (Eq. A.5), one can derive the energy spectrum of the accelerated particles (Arons 2003):

$$\frac{\mathrm{d}N_\mathrm{i}}{\mathrm{d}E} = \frac{9}{4}\frac{c^2 I}{Ze\mu}E^{-1}\left(1+\frac{E}{E_\mathrm{g}}\right)^{-1} \,, \tag{B.8}$$

where

$$E_\mathrm{g} = \frac{5}{72}\frac{Z\eta e\mu^3}{GI^2\varepsilon^2} = 3\times10^{20}\frac{Z\eta_1\mu_{33}^3}{I_{45}^2\varepsilon_2^2}\,\mathrm{eV} \,, \tag{B.9}$$

is the critical gravitational energy at which gravitational wave and electromagnetic losses are equal, with ϵ the ellipticity of the star (see Eq. A.2 and following paragraph). We neglect the influence of r-mode instabilities on the magnetar spin-down: this effect should mainly affect the cut-off of the injected energy spectrum by modifying the energy loss component due to gravitational wave losses (Arons 2003).

The gravitational wave losses start dominating at the highest energies when the magnetic field of the star becomes $\mu \gtrsim 10^{33}$ cgs. Magnetars are thus affected by these losses. For pulsars with milder fields that are the main concern of this paper, gravitational wave losses are negligible, and $E_{\rm g} \gg 10^{20}$ eV. In this case, the injected spectrum reads (Blasi et al. 2000):

$$\frac{{\rm d}N_{\rm i}}{{\rm d}E} = 5 \times 10^{23}\, I_{45} (Z_{26}\, \mu_{30.5}\, E_{20})^{-1} {\rm eV}^{-1}, \quad \text{(B.10)}$$

The spin-down time at which particles of energy E can be accelerated in the voltage drop, when gravitational wave losses are negligible, reads (Arons 2003):

$$\begin{aligned} t_{\rm spin}(E) &= \frac{9}{8} \frac{I c^3}{\mu^2 \Omega_{\rm i}^2} \left(\frac{E_{\rm i}}{E} - 1 \right) \\ &\sim 3 \times 10^7\, E_{20.5}^{-1} \frac{Z_{26} \eta_1 I_{45}}{\mu_{30.5}} \text{ s.} \quad \text{(B.11)} \end{aligned}$$

where $E_{\rm i}$ is the maximum acceleration energy corresponding to the initial angular velocity $\Omega_{\rm i}$. The spin-down time at which particles of energy E can be accelerated does not depend on the initial rotation velocity of the neutron star $\Omega_{\rm i}$, for $E \ll E_{\rm i}$.

C. Early supernova ejecta lightcurves

We use below the notations of Appendix A.

After a few expansion timescales $t_{\rm ex} = R_{\rm ej,i}/v_{\rm SN}$, where $R_{\rm ej,i}$ is the radius of the star that led to the explosion, the supernova ejecta enters into a stage of homologous expansion where its size scales as $R = v_{\rm ej} t$ and its internal energy as $E_{\rm int}(t) \sim (E_{\rm ej}/2)(t_{\rm ex}/t)$.

The ejecta is first optically thick to electron scattering. Noting κ and ρ the opacity and density of the supernova envelope, one can estimate the optical depth of the ejecta: $\tau = R\kappa\rho$. Assuming a constant central supernova density profile (see Matzner & McKee 1999 and Chevalier 2005 for more detailed modeling of the interior structure of supernovae) $\rho = 3M_{\rm ej}/(4\pi R^3)$, one can define the effective diffusion time (for thermal photons to cross the ejecta):

$$t_{\rm d} \equiv \left(\frac{M_{\rm ej}\kappa}{4\pi v_{\rm ej} c}\right)^{1/2} \sim 1.6\times10^6\,{\rm s}\, M_{\rm ej,5}^{1/2}\kappa_{0.2}^{1/2}\left(\frac{v_{\rm ej}}{2\times10^9\,{\rm cm\,s^{-1}}}\right)^{-1/2}, \quad \text{(C.1)}$$

with the opacity to electron scattering defined as $\kappa_{0.2} \equiv \kappa/(0.2\,{\rm g^{-1}\,cm^2})$ for thermal photons. This sets the timescale of the supernova light curve, under the assumption that the opacity remains constant throughout the ejecta (no ionization effect), and in the absence of pulsar or ^{56}Ni heating. For more detailed computation of the these timescales, see, e.g., Kasen & Woosley (2009).

As the ejecta expands, it reaches a time $t_{\rm thin}$ when it becomes optically thin to electron scattering, for thermal photons ($\tau = 1$):

$$t_{\rm thin} = \left(\frac{3M_{\rm ej}\kappa}{4\pi v_{\rm ej}^2}\right)^{1/2} \sim 1.9\times10^7\,{\rm s}\left(\frac{v_{\rm ej}}{2\times10^9\,{\rm cm\,s^{-1}}}\right). \quad \text{(C.2)}$$

For the numerical estimates of $v_{\rm ej}$, we are using the final velocity of the ejecta after its modification by the shock at the interface between the pulsar wind and the initial ejecta, for $E_{\rm ej,51}$, $M_{\rm ej,5}$, and $P_{\rm i} = 10^{-3}$ s (see Eq. A.7).

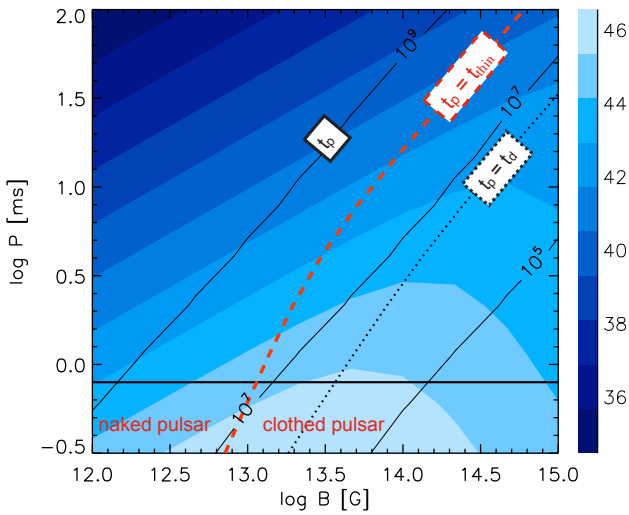

Figure C.1.: *Contour plot of the bolometric luminosity of supernova+pulsar wind nebula systems at 1 yr after explosion, as a function of initial period P and magnetic field B. The various regimes for radiative emissions are represented. The solid lines indicate pulsar spin-down timescale in seconds (Eq. A.3). The red dashed lines represent the pulsar population for which $t_{\rm p} = t_{\rm thin}$, and separate naked and clothed pulsars (see text). The dotted lines represent $t_{\rm p} = t_{\rm d}$.*

We will consider two regimes for the calculation of radiative emissions from the ejecta: optically thin ($t > t_{\rm thin}$), and optically thick ($t < t_{\rm thin}$) for thermal photons. The deposition of pulsar rotational energy will have different effects on the supernova radiative emissions according to the optical depth of the ejecta at time $t_{\rm p}$. Figure C.1 pictures these various regimes. The red dashed lines represent the pulsar population for which $t_{\rm p} = t_{\rm thin}$: on its left-hand side, most of the rotational energy of the pulsar is injected when the supernova ejecta is optically thin to electron scattering (the pulsar is *naked*). On the right-hand side of the red dashed line, the pulsar energy can enhance the luminosity of the supernova, as it is injected while the ejecta is still optically thick (the pulsar is *clothed*).

C.1. Bolometric luminosity lightcurve

In what follows, we calculate the total radiation expected from the supernova ejecta+pulsar wind nebula. The evolution of the ejecta is computed assuming a one zone core-collapse model. This approximation is debatable for times $t \lesssim t_{\rm d}$, as the radiation should be mainly emitted in the central regions, close to the pulsar wind nebula, and not uniformly distributed as the matter over a single shell. This is not expected to be limiting for our study however, as we are most interested in the late-time light curves (a few years after the explosion), when the ejecta starts to become optically thin.

How much energy of the pulsar wind will be transformed into radiation depends on many factors such as the nature of the wind (leptonic, hadronic or Poynting flux dominated), the efficiency of particle acceleration and of radiative processes. In a first step, these conditions can be parametrized by setting a fraction η_γ of the wind energy $E_{\rm p}$ that is converted to radiative energy (thermal or non thermal) in the pulsar wind nebula.

Under the one zone model approximation, the radiation pressure dominates throughout the remnant, $P = E_{\rm int}/3V$, with V the volume of the ejecta. The internal energy then follows the law:

$$\frac{1}{t}\frac{\partial}{\partial t}[E_{\rm int} t] = \eta_\gamma L_{\rm p}(t) - L_{\rm rad}(t) \ . \qquad \text{(C.3)}$$

The radiated luminosity $L_{\rm rad}$ depends on the ejecta optical depth:

$$\frac{L_{\rm rad}(t)}{4\pi R^2} = \frac{E_{\rm int} c}{(4\pi/3)R^3} \quad t > t_{\rm thin} \qquad \text{(C.4)}$$

$$= \frac{E_{\rm int} c}{(4\pi/3)\tau R^3} \quad t \leq t_{\rm thin} \qquad \text{(C.5)}$$

which yields

$$L_{\rm rad}(t) = \frac{3}{\beta_{\rm ej}}\frac{E_{\rm int}}{t} \quad t > t_{\rm thin} \qquad \text{(C.6)}$$

$$= \frac{E_{\rm int} t}{t_{\rm d}^2} \quad t \leq t_{\rm thin} \qquad \text{(C.7)}$$

where we note $\beta_{\rm ej} \equiv v_{\rm ej}/c$. For $t < t_{\rm thin}$, we assumed that the totality of the luminosity $\eta_\gamma L_{\rm p}$ deposited in the ejecta as photons is thermalized, and used the diffusion transport approximation Arnett (1980). In the optically thin regime, photons do not diffuse and propagate straight out of the ejecta.

Equation (C.3) yields

$$E_{\rm int}(t > t_{\rm thin}) = \frac{\eta_\gamma E_{\rm p}}{1+3/\beta_{\rm ej}}\left[h_1\left(\frac{t}{t_{\rm p}}\right) - h_2\left(\frac{t}{t_{\rm p}}\right)\right] \qquad \text{(C.8)}$$

$$E_{\rm int}(t \leq t_{\rm thin}) = \frac{1}{t}\, e^{-\frac{t^2}{2t_{\rm d}^2}}\left[\int_{t_{\rm ex}}^{t} e^{\frac{x^2}{2t_{\rm d}^2}}\frac{\eta_\gamma E_{\rm p} t_{\rm p} x}{(t_{\rm p}+x)^2}{\rm d}x + E_{\rm ej}\, t_{\rm ex}\, e^{\frac{t_{\rm ex}^2}{2t_{\rm d}^2}}\right] . \qquad \text{(C.9)}$$

The hypergeometric functions are noted:

$$h_1(x) \equiv \ {}_2F_1(1, 1+3/\beta_{\rm ej}, 2+3/\beta_{\rm ej}, -x) \qquad \text{(C.10)}$$

$$h_2(x) \equiv \ {}_2F_1(2, 1+3\beta_{\rm ej}, 2+3/\beta_{\rm ej}, -x) \qquad \text{(C.11)}$$

Note that $L_{\rm rad}(t) \sim \eta_\gamma L_{\rm p}(t)$ for $t > t_{\rm thin}$.

To calculate the total bolometric radiated luminosity, we add to $L_{\rm rad}(t)$ the contribution of the ordinary core-collapse supernova radiation $L_{\rm SN}(t)$. $L_{\rm SN}(t)$ is calculated following Eq. (5) of Chatzopoulos et al. (2012), assuming an initial luminosity output of 10^{42} erg/s, as is estimated by Woosley & Heger (2002) in their Eq. (41), for $M_{\rm ej} = 5\,M_\odot$ and $E_{\rm ej} = 10^{51}\,{\rm erg\,s^{-1}}$. $L_{\rm SN}$ only contributes when $E_{\rm p} < E_{\rm SN}$.

C.2. Photo-disintegration in supernova ejectas

Ultrahigh energy ions can also experience photo-pion production or photo-disintegration in the radiation fields generated in the nebula, at the interface between the pulsar wind and the supernova shell.

The thermal component in the supernova ejecta peaks at energy $\epsilon_\gamma = kT \sim 0.4\,(\eta_{\gamma,1}\eta_{\rm th})^{1/4} E_{\rm ej,52}^{-1/8} M_{\rm ej,1}^{3/8} t_{\rm yr}^{-3/4}$ eV, with energy density $U_{\rm th} \sim 0.5\,\eta_{\gamma,1}\eta_{\rm th} E_{\rm ej,52}^{-1/2} M_{\rm ej}^{3/2} t_{\rm yr}^{-3}\,{\rm erg\,cm^{-3}}$, where $\eta_{\gamma,1} \equiv \eta_\gamma/0.1$. This background leads to a cooling time by photo-disintegration of order:

$$t_{A\gamma,{\rm th}} = [c\,\xi_{A\gamma}(\Delta\epsilon_{A\gamma}/\bar{\epsilon}_{A\gamma})\sigma_{A\gamma} U_{\rm th}/\epsilon_\gamma]^{-1} \qquad \text{(C.12)}$$

$$\sim 10^5 A_{56}^{-0.21}\left(\frac{E_{\rm ej,52}}{\eta_{\gamma,1}^2\eta_{\rm th}^2}\right)^{3/8} M_{\rm ej,10}^{-9/8} t_{\rm yr}^{9/4} \qquad \text{(C.13)}$$

where $\Delta\epsilon_{A\gamma}/\bar{\epsilon}_{A\gamma} \sim 0.4\,A_{56}^{0.21}$, $\sigma_{A\gamma} \sim 8\times10^{-26}\,A_{56}\,{\rm cm^{-2}}$ (Murase et al. 2008b), and we take for the elasticity of the $A\gamma$ interaction: $\xi_{A\gamma} = 1/A$ (which is a crude approximation). This estimate of the cooling time is valid for cosmic-ray energy $E_{A,{\rm peak}} \sim 4\times10^{17}\,(\eta_{\gamma,1}\eta_{\rm th})^{-1/4} E_{\rm ej,52}^{1/8} M_{\rm ej,10}^{-3/8} t_{\rm yr}^{3/4}$ eV, and is about one order of magnitude larger for $E_A \gtrsim E_{A,{\rm peak}}$, as the photo-disintegration cross-section lowers. At the highest energies ($E_A \sim 10^{20}$ eV), photo-disintegration could thus play a role on the escape of cosmic rays if the radiation and thermalization efficiencies are higher than

$\eta_\gamma \eta_{\rm th} \gtrsim 10^{-2}$. The rate of wind energy going to radiation is evaluated to be of order 10% (e.g., Kasen & Bildsten 2010), but the thermalization fraction of these photons, $\eta_{\rm th}$, is not known, due to the uncertainties on the opacities in the internal shock region. Mixing and Rayleigh-Taylor instabilities effects creating finger-type structures could lead to a leaking of the high energy photons, and the thermalization fraction could be as low as $\lesssim 10\%$. A higher acceleration efficiency η would also enable particles to reach the highest energies by the time the radiation field intensity has become negligible. Given these uncertainties, and for simplicity, we will assume in this paper that the radiation field can be neglected for the escape of UHECRs from supernova envelopes, the baryonic background playing the major role.

The thermal photon energy density in the ejecta $U_{\rm th}$ reads

$$U_{\rm th} = \frac{3}{4\pi R_{\rm ej}^3} \int_0^t L_{\rm th} {\rm d}t' \ . \qquad \text{(C.14)}$$

The corresponding ejecta temperature then reads $T = (U_{\rm th}/a)^{1/4}$, where a is the radiation constant. This thermal component peaks at energy $\epsilon_{\gamma,{\rm th}} = kT$. The thermal radiation background leads to a cooling time by photo-disintegration for a proton can be written

$$\begin{aligned} t_{p\gamma,{\rm th}} &= \left(c\, \xi_{p\gamma} \sigma_{p\gamma} \frac{\Delta\epsilon_{p\gamma}}{\bar{\epsilon}_{p\gamma}} \frac{U_{\rm th}}{\epsilon_{\gamma,{\rm th}}} \right)^{-1} \qquad \text{(C.15)} \\ &\sim 10\,{\rm s}\, \eta_\gamma^{-3/4} \eta_{\rm th}^{-3/4} I_{45}^{3/8} P_{{\rm i},-3}^{3/4} M_{{\rm ej},1}^{-9/8} t_{7.5}^{9/4} \end{aligned}$$

where $\Delta\epsilon_{p\gamma}/\bar{\epsilon}_{p\gamma} \sim 1.5$, $\sigma_{p\gamma} \sim 5 \times 10^{-28}\,{\rm cm}^{-2}$, and the elasticity of the $p\gamma$ interaction $\xi_{p\gamma} = 0.5$. For nuclei,

$$\begin{aligned} t_{A\gamma,{\rm th}} &= \left(c\, \xi_{A\gamma} \frac{\Delta\epsilon_{A\gamma}}{\bar{\epsilon}_{A\gamma}} \sigma_{A\gamma} \frac{U_{\rm th}}{\epsilon_{\gamma,{\rm th}}} \right)^{-1} \qquad \text{(C.16)} \\ &\sim 10^4\,{\rm s}\, A_{56}^{-0.21} \eta_\gamma^{-3/4} \eta_{\rm th}^{-3/4} I_{45}^{3/8} P_{{\rm i},-3}^{3/4} M_{{\rm ej},1}^{-9/8} t_{7.5}^{9/4} \end{aligned}$$

where $\Delta\epsilon_{A\gamma}/\bar{\epsilon}_{A\gamma} \sim 0.4\, A_{56}^{0.21}$, $\sigma_{A\gamma} \sim 8 \times 10^{-26}\, A_{56}\,{\rm cm}^{-2}$ (Murase et al. 2008b), and we take for the elasticity of the $A\gamma$ interaction: $\xi_{A\gamma} = 1/A$.

The thermal and non-thermal radiation backgrounds at the early stages of the nebula can be computed in more details following Kotera et al. (2013) and Section 6.1.2. The contribution of the non-thermal component to losses can be calculated following the same line as for the thermal component, assuming that the photon spectrum peaks at $\epsilon_{\rm b}$ for the Inverse Compton radiation, and at the characteristic energy for the synchrotron X-ray emission.

It can be calculated that the thermal background dominates over the non-thermal backgrounds throughout the pulsar (B, P) parameter space. By comparing equations (C.15−C.16) and (3.10), we find that protons will essentially interact by photo-pion production in the thermal background of the SN ejecta, for mildly magnetized pulsars. For nuclei, hadronic interactions would dominate as long as the radiation and thermalization fractions are $\eta_\gamma \eta_{\rm th} \lesssim 10^3$. Mixing and Rayleigh-Taylor instabilities effects creating finger-type structures could lead to a leaking of the high energy photons, and the thermalization fraction could be as low as $\lesssim 10\%$. We have also assumed that the radiation background is isotropic. In the case of a jet-like structure, the radiation field would be beamed and the corresponding photon energy experienced by the proton would scale with $1/\Gamma$, Γ being the Lorentz factor of the jet. For lower dissipation efficiency into radiation, and for beamed radiation, the contribution of the radiative background should be lower, and it is likely that the hadronic interactions become dominant over a large fraction of the parameter space that enables the acceleration of particles to UHE.

D. Radiative transfer basics in stellar atmospheres

Here we give a few elements of radiative transfer in stellar atmospheres, necessary to understand the heating of binary companion atmospheres in Section 6.2. For more details on this subject, one can refer to, e.g., Rybicki & Lightman (1985).

D.1. Atmospheric column densities

Atmosphere column densities read

$$\Sigma(<z) \equiv \int_0^z z'\rho(z')\mathrm{d}z' \ , \tag{D.1}$$

where the matter density at a given depth can be modeled roughly as $\rho(z) = \rho_0 \exp(z/h)$, with ρ_0 and h depend on the atmospheric structure that we consider.

D.2. Rosseland Approximation

Optical depths at a depth z for photons of frequency ν can be written $\tau_\nu(z) = \int_0^z \alpha_\nu(z')\mathrm{d}z'$, where we have introduced the absorption coefficient $\alpha_\nu(z)$.

At large optical depths in a star, the mean free path of photons λ_ν is generally much shorter than temperature or density gradient scales. One can then assume that matter and photons are in a local thermal equilibrium. Because λ_ν is also smaller than the radius of curvature of surfaces of equal temperature and density, we can assume a plane-parallel geometry[1]. Under these assumptions, one can write that the radiated intensities at frequency ν approach the Planck function: $I_\nu = B_\nu(T)$.

It is then possible to define a mean absorption coefficient as a function of the temperature T, called the Rosseland mean:

$$\begin{aligned} \alpha_\mathrm{R}(T) &= \frac{\partial B_\nu(T)}{\partial T}\left[\int_0^\infty \frac{\partial B_\nu(T)}{\partial T}\alpha_\nu^{-1}\mathrm{d}\nu\right]^{-1} \\ &= \frac{4\sigma_T T^3}{\pi}\left[\int_0^\infty \frac{\partial B_\nu(T)}{\partial T}\alpha_\nu^{-1}\mathrm{d}\nu\right]^{-1} \end{aligned} \tag{D.2}$$

This quantity is defined as an average absorption coefficient over the temperature derivative of the black-body function $B_\nu(T)$. The Rosseland mean optical depth is then defined as

$$\tau_\mathrm{R}(z) = \int_0^z \alpha_\mathrm{R}(z')\mathrm{d}z' \ . \tag{D.3}$$

The Rosseland approximation for the local total photon flux can be calculated as:

$$F = -\frac{16\,\sigma_\mathrm{T} T^3}{3\alpha_\mathrm{R}}\frac{\partial T}{\partial z} \ . \tag{D.4}$$

This equation shows that radiative energy transport deep in a star can be pictured as a conductive process, with an effective heat conductivity of $-16\,\sigma_\mathrm{T}T^3/(3\alpha_\mathrm{R})$.

D.3. The photosphere

The photosphere can be defined as the region where the Rosseland-mean optical depth $\tau_\mathrm{R}(z_\mathrm{phot}) \sim 1-2/3$. The temperature at the photosphere equals the effective temperature in the Stefan-Boltzman law, T_eff. The energy transport is dominated by convection deep below the photosphere, and by radiation at and above the photosphere.

[1] In the plane-parallel approximation, the material properties (temperature, absorption coefficient, etc.) depend only on the depth in the medium.

Bibliography

Aab, A. et al. 2013

Aartsen, M. G., Ackermann, M., Adams, J., et al. 2014, ArXiv e-prints

Abbasi, R., Abdou, Y., Abu-Zayyad, T., et al. 2013, Astropart. Phys., 44, 40

Abbasi, R., Abdou, Y., Abu-Zayyad, T., et al. 2011a, ApJ, 740, 16

Abbasi, R., Abdou, Y., Abu-Zayyad, T., et al. 2010, Physical Review Letters, 104, 161101

Abbasi, R., Abdou, Y., Abu-Zayyad, T., et al. 2011b, Physical Review Letters, 106, 141101

Abbasi, R. et al. 2010, Phys.Rev.Lett., 104, 161101

Abbasi, R. et al. 2011

Abbasi, R. U. et al. 2008, Physical Review Letters, 100, 101101

Abbasi, R. U. et al. 2009, Astroparticle Physics, 32, 53

Abbasi, R. U. et al. 2010, ArXiv e-prints

Abdo, A. A., Ackermann, M., Ajello, M., et al. 2009a, Phys. Rev. Lett., 102, 181101

Abdo, A. A., Allen, B., Aune, T., et al. 2008, Phys. Rev. Lett., 101, 221101

Abdo, A. A., Allen, B. T., Aune, T., et al. 2009b, ApJ, 698, 2121

Abraham, J., Abreu, P., Aglietta, M., et al. 2010a, Phys. Rev. Lett., 104, 091101

Abraham, J., Abreu, P., Aglietta, M., et al. 2010b, Phys. Lett. B, 685, 239

Abraham, J. et al. 2009, Phys. Rev. D, 79, 102001

Abreu, P., Aglietta, M., Ahn, E. J., et al. 2010, Astropart. Phys., 34, 314

Abreu, P. et al. 2011, 32nd International Cosmic Ray Conference, Beijing, China, arXiv:1107.4804

Abreu, P. et al. 2011

Abreu, P. et al. 2013, JCAP, 1305, 009

Abu-Zayyad, T. et al. 2001, Astrophys.J., 557, 686

Acciari, V. A., Aliu, E., Arlen, T., et al. 2010, ApJ Lett., 715, L49

Acciari, V. A., Aliu, E., Arlen, T., et al. 2009, Ap. J., 695, 1370

Ackermann, M., Ajello, M., Allafort, A., et al. 2012, Physical Review Letters, 108, 011103

Ackermann, M., Ajello, M., Allafort, A., et al. 2013, Science, 339, 807

Ackermann, M., Ajello, M., Atwood, W. B., et al. 2010, Phys. Rev. D, 82, 092004

Adams, J. et al. 2012

Adriani, O., Barbarino, G. C., Bazilevskaya, G. A., et al. 2009, Nature, 458, 607

Adriani, O., Barbarino, G. C., Bazilevskaya, G. A., et al. 2011, Phys. Rev. Lett., 106, 201101

Adriani, O., Barbarino, G. C., Bazilevskaya, G. A., et al. 2009, Nature, 458, 607

Adriani, O., Barbarino, G. C., Bazilevskaya, G. A., et al. 2013, Phys. Rev. Lett., 111, 081102

Aglietta, M. et al. 2003, Conference C03-07-31, 183

Aguilar, M., Alberti, G., Alpat, B., et al. 2013, Phys. Rev. Lett., 110, 141102

Aharonian, F., Akhperjanian, A. G., Anton, G., et al. 2009, A&A, 508, 561

Aharonian, F., Akhperjanian, A. G., Barres de Almeida, U., et al. 2007a, A&A, 473, L25

Aharonian, F., Akhperjanian, A. G., Barres de Almeida, U., et al. 2007b, A&A, 475, L9

Aharonian, F., Akhperjanian, A. G., Bazer-Bachi, A. R., et al. 2007c, A&A, 470, 475

Ahlers, M., Anchordoqui, L. A., & Sarkar, S. 2009, Phys. Rev. D, 79, 083009

Ahlers, M. & Murase, K. 2013, ArXiv e-prints

Ahn, E.-J., Engel, R., Gaisser, T. K., Lipari, P., & Stanev, T. 2009, Phys.Rev., D80, 094003

Ahn, H. S. et al. 2008, in International Cosmic Ray Conference, Vol. 2, 79

Albert, J., Aliu, E., Anderhub, H., et al. 2006, ApJ Lett., 642, L119

Alcock, C., Farhi, E., & Olinto, A. 1986, ApJ, 310, 261

Alcock, C. & Hatchett, S. 1978, Astrophys. J., 222, 456

Alcock, C. & Olinto, A. 1988, Annual Review of Nuclear and Particle Science, 38, 161

Allard, D., Ave, M., Busca, N., et al. 2006, J. Cos. and Astro. Phys., 9, 5

Allard, D., Busca, N. G., Decerprit, G., Olinto, A. V., & Parizot, E. 2008, J. Cos. and Astro. Phys., 10, 33

Allard, D., Parizot, E., & Olinto, A. V. 2007, Astropart. Phys., 27, 61

Allard, D., Parizot, E., Olinto, A. V., Khan, E., & Goriely, S. 2005, A&A, 443, L29

Allard, D. & Protheroe, R. J. 2009, A&A, 502, 803

Allison, P., Auffenberg, J., Bard, R., et al. 2012, Astropart.Phys., 35, 457

Aloisio, R., Berezinsky, V., & Gazizov, A. 2009, ArXiv e-prints, 0907.5194

Aloisio, R. & Berezinsky, V. S. 2005, ApJ, 625, 249

Amato, E., Guetta, D., & Blasi, P. 2003, Astron. Astrophys., 402, 827

Amenomori, M. et al. 2005, Astrophys.J., 626, L29

Amenomori, M. et al. 2006, Science, 314, 439

Anchordoqui, L. A., Hooper, D., Sarkar, S., & Taylor, A. M. 2008, Astroparticle Physics, 29, 1

Anchordoqui, L. A. & Montaruli, T. 2010, Ann. Rev. Nucl. Part. Sci., 60

Anchordoqui, L. A., Paul, T. C., da Silva, L. H. M., Torres, D. F., & Vlcek, B. J. 2014, ArXiv e-prints

Antoni, T. et al. 2003, Nucl.Instrum.Meth., A513, 490

Apanasenko, A. V. et al. 2001, in International Cosmic Ray Conference, Vol. 5, 1622

Apel, W. et al. 2011, Phys.Rev.Lett., 107, 171104

Apel, W. D., Arteaga-Velázquez, J. C., Bekk, K., et al. 2013, Astropart. Phys., 47, 54

Apel, W. D. et al. 2009, ArXiv 0906.4007

Archibald, A. M., Kaspi, V. M., Bogdanov, S., et al. 2010, ApJ, 722, 88

Archibald, A. M., Stairs, I. H., Ransom, S. M., et al. 2009, Science, 324, 1411

Arkani-Hamed, N., Finkbeiner, D. P., Slatyer, T. R., & Weiner, N. 2009, Phys. Rev. D, 79, 15014

Armengaud, E., Sigl, G., & Miniati, F. 2006, Phys. Rev. D, 73, 083008

Arnett, D. 1996, Supernovae and Nucleosynthesis: An Investigation of the History of Matter from the Big Bang to the Present

Arnett, W. D. 1980, ApJ, 237, 541

Arons, J. 1983, ApJ, 266, 215

Arons, J. 2002, in Astronomical Society of the Pacific Conference Series, Vol. 271, Neutron Stars in Supernova Remnants, ed. P. O. Slane & B. M. Gaensler, 71

Arons, J. 2003, ApJ, 589, 871

Arons, J. 2007, ArXiv: 0708.1050

Arons, J. & Scharlemann, E. T. 1979, ApJ, 231, 854

Arons, J. & Tavani, M. 1993, ApJ, 403, 249

Atoyan, A. & Dermer, C. D. 2008, ApJ Lett., 687, L75

Ave, M. et al. 2005, Astropart. Phys., 23, 19

Baerwald, P., Bustamante, M., & Winter, W. 2014, ArXiv e-prints: 1401.1820

Baklanov, P. V., Blinnikov, S. I., & Pavlyuk, N. N. 2005, Astronomy Letters, 31, 429

Bandiera, R., Pacini, F., & Salvati, M. 1984, ApJ, 285, 134

Baring, M. G. & Harding, A. K. 2001, ApJ, 547, 929

Barwick, S. 2011, International Cosmic Ray Conference, 4, 238

Bassa, C. G., van Kerkwijk, M. H., & Kulkarni, S. R. 2006, A&A, 450, 295

Beck, R. 2008, in AIP Conf Series, ed. F. A. Aharonian et al., Vol. 1085, 83

Beck, R., Gaensler, B., & Feretti, L. 2007, SKA and the Magnetic Universe (Springer-Verlag), 103

Bednarek, W. & Bartosik, M. 2004, A&A, 423, 405

Bednarek, W. & Protheroe, R. J. 1997, Physical Review Letters, 79, 2616

Bednarek, W. & Protheroe, R. J. 2002, Astroparticle Physics, 16, 397

Begelman, M. C. & Li, Z.-Y. 1992, ApJ, 397, 187

Bell, A. R. 1978, Month. Not. Roy. Astron. Soc., 182, 147

Bell, A. R. & Lucek, S. G. 2001, MNRAS, 321, 433

Bennett, L. & Ellison, D. C. 1995, Journal of Geophysical Research, 100, 3439

Berezinsky, V. 2006, Nuclear Physics B Proceedings Supplements, 151, 260

Berezinsky, V., Gazizov, A., & Grigorieva, S. 2005, Phys.Lett.B, 612, 147

Berezinsky, V., Gazizov, A., & Grigorieva, S. 2006, Phys. Rev. D, 74, 043005

Berezinsky, V. S., Blasi, P., & Ptuskin, V. S. 1997, ApJ, 487, 529

Berezinsky, V. S. & Grigorieva, S. I. 1988, Astron. Astrophys., 199, 1

Bertone, G., Isola, C., Lemoine, M., & Sigl, G. 2002, Phys. Rev. D, 66, 103003

Bhattacharjee, P. 2000, Physics Reports, 327, 109

Bhattacharya, D. 1990, Journal of Astrophysics and Astronomy, 11, 125

Biermann, P. L. & Cassinelli, J. P. 1993, Astron. Astrophys. , 277, 691

Bietenholz, M. F., Bartel, N., & Rupen, M. P. 2010, ApJ, 712, 1057

Bignami, G. F., Caraveo, P. A., & Mereghetti, S. 1992, ApJ Lett., 389, L67

Blaksley, C., Parizot, E., Decerprit, G., & Allard, D. 2013, A&A, 552, A125

Blandford, R. & Eichler, D. 1987, Phys. Rep., 154, 1

Blasi, P. 2011, in **Cosmic Rays for Particle and Astroparticle Physics**, edited by S. Giani, C. Leroy, and P. G. Rancoita, Proceedings of the 12th ICATPP Conference,, pp. 493

Blasi, P. 2013, Nuclear Physics B Proceedings Supplements, 239, 140

Blasi, P. & Amato, E. 2012a, J. Cos. and Astro. Phys., 1, 10

Blasi, P. & Amato, E. 2012b, J. Cos. and Astro. Phys., 1, 11

Blasi, P., Burles, S., & Olinto, A. V. 1999, ApJl, 514, L79

Blasi, P., Epstein, R. I., & Olinto, A. V. 2000, ApJ Lett., 533, L123

Blum, K., Katz, B., & Waxman, E. 2013

Bonazzola, S. & Gourgoulhon, E. 1996, A&A, 312, 675

Borla Tridon, D. 2011, International Cosmic Ray Conference, 6, 43

Bradt, H., Rappaport, S., & Mayer, W. 1969, Nature, 222, 728

Bucciantini, N., Arons, J., & Amato, E. 2011, MNRAS, 410, 381

Bucciantini, N., Quataert, E., Arons, J., Metzger, B. D., & Thompson, T. A. 2007, MNRAS, 380, 1541

Bucciantini, N., Thompson, T. A., Arons, J., Quataert, E., & Del Zanna, L. 2006, MNRAS, 368, 1717

Budnev, N., Chvalaiev, O., Gress, O., et al. 2009, Nucl.Phys.Proc.Suppl., 190, 247

Budnik, R., Katz, B., MacFadyen, A., & Waxman, E. 2008, ApJ, 673, 928

Buonanno, A., Sigl, G., Raffelt, G. G., Janka, H., & Müller, E. 2005, Phys. Rev. D, 72, 084001

Carretti, E., Crocker, R. M., Staveley-Smith, L., et al. 2013, Nature, 493, 66

Cerutti, B., Dubus, G., & Henri, G. 2008, A&A, 488, 37

Cerutti, B., Malzac, J., Dubus, G., & Henri, G. 2010, A&A, 519, A81

Cesarsky, C. J. 1980, Ann. Rev. Astron. Astrophys., 18, 289

Chang, J., Adams, J. H., Ahn, H. S., et al. 2008, Nature, 456, 362

Chatzopoulos, E., Wheeler, J. C., & Vinko, J. 2012, ApJ, 746, 121

Chen, D. 2008, in International Cosmic Ray Conference, Vol. 4, 103–106

Chen, P., Tajima, T., & Takahashi, Y. 2002, Physical Review Letters, 89, 161101

Cheng, K. S., Ho, C., & Ruderman, M. 1986a, ApJ, 300, 500

Cheng, K. S., Ho, C., & Ruderman, M. 1986b, ApJ, 300, 522

Cheng, K. S. & Usov, V. V. 2006, Phys. Rev. D, 74, 127303

Chevalier, R. A. 1977, in Astrophysics and Space Science Library, Vol. 66, Supernovae, ed. D. N. Schramm, 53

Chevalier, R. A. 2005, ApJ, 619, 839

Chevalier, R. A. & Fransson, C. 1992, ApJ, 395, 540

Chi, X., Cheng, K. S., & Young, E. C. M. 1996, ApJ Lett., 459, L83

Cholis, I., Goodenough, L., Hooper, D., Simet, M., & Weiner, N. 2009, Phys. Rev. D, 80, 123511

Cirelli, M. & Panci, P. 2009, Nucl. Phys. B, 821, 399

Cirelli, M., Panci, P., & Serpico, P. D. 2010, Nucl. Phys. B, 840, 284

Cocke, W. J., Disney, M. J., & Taylor, D. J. 1969, Nature, 221, 525

Colafrancesco, S. & Blasi, P. 1998, Astroparticle Physics, 9, 227

Contopoulos, I. & Kazanas, D. 2002, ApJ, 566, 336

Cronin, J. W. 2011, European Physical Journal H, 36, 183

Dai, Z. G. & Lu, T. 2001, ApJ, 551, 249

Das, S., Kang, H., Ryu, D., & Cho, J. 2008, ApJ, 682, 29

Dawson, B. R. et al. 2013, EPJ Web Conf., 53, 01005

De Domenico, M., Settimo, M., Riggi, S., & Bertin, E. 2013, JCAP, 1307, 050

de Marco, D., Hansen, P., Stanev, T., & Blasi, P. 2006, Phys. Rev. D, 73, 043004

Decerprit, G. & Allard, D. 2011, ArXiv 1107.3722

Del Zanna, L., Amato, E., & Bucciantini, N. 2004, A&A, 421, 1063

Del Zanna, L., Volpi, D., Amato, E., & Bucciantini, N. 2006, A&A, 453, 621

Delahaye, T., Kotera, K., & Silk, J. 2014, ArXiv e-prints: 1404.7546

Delahaye, T., Lavalle, J., Lineros, R., Donato, F., & Fornengo, N. 2010, Astron. Astrophys., 524, A51

Delahaye, T., Lineros, R., Donato, F., et al. 2009, Astron. Astrophys., 501, 821

Delahaye, T., Lineros, R., Donato, F., Fornengo, N., & Salati, P. 2008, Phys. Rev. D, 77, 22

Dermer, C. D. 2002, ApJ, 574, 65

Dermer, C. D., Murase, K., & Takami, H. 2012, ApJ, 755, 147

Dessart, L., Hillier, D. J., Waldman, R., Livne, E., & Blondin, S. 2012, ArXiv e-prints

Dieckmann, M. E. & Bret, A. 2009, ApJ, 694, 154

Dolag, K., Grasso, D., Springel, V., & Tkachev, I. 2005, J. Cos. and Astro. Phys., 1, 9

Donato, F., Fornengo, N., Maurin, D., Salati, P., & Taillet, R. 2004, Phys. Rev. D, 69, 063501

Donato, F., Maurin, D., Brun, P., Delahaye, T., & Salati, P. 2009, Phys. Rev. Lett., 102, 5

Donato, F., Maurin, D., Salati, P., et al. 2001, Astrophys. J., 563, 35

Donnert, J., Dolag, K., Lesch, H., & Müller, E. 2009, MNRAS, 392, 1008

d'Orfeuil, B. R., Allard, D., Lachaud, C., et al. 2014

Dubus, G. 2006a, A&A, 451, 9

Dubus, G. 2006b, A&A, 456, 801

Dubus, G. 2013, A&ARv, 21, 64

Dubus, G., Cerutti, B., & Henri, G. 2008, A&A, 477, 691

Duncan, R. C. & Thompson, C. 1992, ApJ Letters, 392, L9

Edmonds, P. D., Gilliland, R. L., Camilo, F., Heinke, C. O., & Grindlay, J. E. 2002, ApJ, 579, 741

Emmering, R. T. & Chevalier, R. A. 1987, ApJ, 321, 334

Engel, R., Seckel, D., & Stanev, T. 2001, Phys. Rev. D, 64, 093010

Erlykin, A. D. & Wolfendale, A. W. 2002, Journal of Physics G Nuclear Physics, 28, 359

Erlykin, A. D. & Wolfendale, A. W. 2006, Astropart. Phys., 25, 183

Essey, W., Ando, S., & Kusenko, A. 2011, Astroparticle Physics, 35, 135

Essey, W., Kalashev, O. E., Kusenko, A., & Beacom, J. F. 2010, Phys. Rev. Lett., 104, 141102

Essey, W., Kalashev, O. E., Kusenko, A., & Beacom, J. F. 2010, Physical Review Letters, 104, 141102

Essey, W. & Kusenko, A. 2013, ArXiv e-prints

Fang, J. & Zhang, L. 2010, A&A, 515, A20

Fang, K., Kotera, K., Murase, K., & Olinto, A. V. 2013a, ArXiv e-prints: 1311.2044

Fang, K., Kotera, K., & Olinto, A. V. 2012, ApJ, 750, 118

Fang, K., Kotera, K., & Olinto, A. V. 2013b, J. Cos. and Astro. Phys., 3, 10

Faucher-Giguère, C.-A. & Kaspi, V. M. 2006, ApJ, 643, 332

Fermi, E. 1949, Phys. Rev., 75, 1169

Ferrigno, C., Blasi, P., & de Marco, D. 2004, Nucl. Phys. B Proc. Suppl., 136, 191

Fowler, J., Fortson, L., Jui, C., et al. 2001, Astropart.Phys., 15, 49

Fritz, G., Henry, R. C., Meekins, J. F., Chubb, T. A., & Friedman, H. 1969, Science, 164, 709

Fruchter, A. S., Berman, G., Bower, G., et al. 1990, ApJ, 351, 642

Gabici, S. & Aharonian, F. A. 2005, Physical Review Letters, 95, 251102

Gabici, S. & Aharonian, F. A. 2007, ApJ Lett., 665, L131

Gaensler, B. M. & Slane, P. O. 2006, ARAA, 44, 17

Gaffet, B. 1977a, ApJ, 216, 565

Gaffet, B. 1977b, ApJ, 216, 852

Gallant, Y. A. & Arons, J. 1994, ApJ, 435, 230

Gelfand, J. D., Slane, P. O., & Zhang, W. 2009, ApJ, 703, 2051

Gelmini, G., Kalashev, O., & Semikoz, D. V. 2007, Astroparticle Physics, 28, 390

Giacinti, G., Kachelriess, M., Semikoz, D., & Sigl, G. 2011, Astropart.Phys., 35, 192

Giacinti, G. & Sigl, G. 2012, Phys. Rev. Lett., 109, 071101

Giller, M. & Lipski, M. 2002, Journal of Physics G Nuclear Physics, 28, 1275

Ginzburg, V. L. & Syrovatskii, S. I. 1964, The Origin of Cosmic Rays (Macmillan, New York)

Giuliani, A., Cardillo, M., Tavani, M., et al. 2011, ApJ Lett., 742, L30

Globus, N., Allard, D., & Parizot, E. 2008, A&A, 479, 97

Gold, T. 1968, Nature, 218, 731

Goldreich, P. & Julian, W. H. 1969, ApJ, 157, 869

Gorham, P. W. et al. 2010, arXiv:1003.2961

Grasso, D., Profumo, S., Strong, A. W., et al. 2009, Astropart. Phys., 32, 140

Green, D. A. 2009, Bulletin of the Astronomical Society of India, 37, 45

Greisen, K. 1966, Phys. Rev. Lett., 16, 748

Grigorov, N. L. et al. 1971, in ICRC, Vol. 1, 172

Guillian, G., Hosaka, J., Ishihara, K., et al. 2007, Phys. Rev. D, 75, 062003

Gunn, J. E. & Ostriker, J. P. 1969, Physical Review Letters, 22, 728

Haensel, P., Lasota, J. P., & Zdunik, J. L. 1999, A&A, 344, 151

Halpern, J. P. & Holt, S. S. 1992, Nature, 357, 222

Hamuy, M. 2003, ApJ, 582, 905

Han, J. L. 2008, Nuclear Physics B Proceedings Supplements, 175, 62

Harari, D., Mollerach, S., & Roulet, E. 2002, Journal of High Energy Physics, 7, 6

Harding, A. K. & Lai, D. 2006, Reports on Progress in Physics, 69, 2631

Harding, A. K. & Muslimov, A. G. 2001, ApJ, 556, 987

Harding, A. K. & Muslimov, A. G. 2002, ApJ, 568, 862

He, H.-N., Liu, R.-Y., Wang, X.-Y., et al. 2012, ApJ, 752, 29

Heinke, C. O., Deloye, C. J., Jonker, P. G., Wijnands, R., & Taam, R. E. 2008, in American Institute of Physics Conference Series, Vol. 1068, American Institute of Physics Conference Series, ed. R. Wijnands, D. Altamirano, P. Soleri, N. Degenaar, N. Rea, P. Casella, A. Patruno, & M. Linares, 209–216

Heinke, C. O. & Ho, W. C. G. 2010, ApJL, 719, L167

Hillas, A. M. 1984, Ann. Rev. Astron. Astrophys., 22, 425

Hillas, A. M. 2005, J. of Phys. G Nucl. Phys., 31, 95

Hillas, A. M. 2006, ArXiv eprints: 0607109

Hoffman, R. D., Woosley, S. E., & Qian, Y.-Z. 1997, ApJ, 482, 951

Hooper, D., Blasi, P., & Dario Serpico, P. 2009, JCAP, 1, 25

Hooper, D., Taylor, A., & Sarkar, S. 2005, Astropart. Phys., 23, 11

Horiuchi, S., Murase, K., Ioka, K., & Mészáros, P. 2012, ApJ, 753, 69

Hoshino, M., Arons, J., Gallant, Y. A., & Langdon, A. B. 1992, ApJ, 390, 454

Huang, H. H. & Becker, W. 2007, A&A, 463, L5

Hümmer, S., Baerwald, P., & Winter, W. 2012, Physical Review Letters, 108, 231101

IceCube Collaboration. 2013, Science, 342

IceCube Collaboration, Abbasi, R., Abdou, Y., et al. 2013, Astroparticle Physics, 42, 15

Inoue, S., Sigl, G., Miniati, F., & Armengaud, E. 2007, ArXiv e-prints

Jones, F. C. & Ellison, D. C. 1991, Space Science Reviews, 58, 259

Jui, C. C. 2011

Jun, B.-I. 1998, ApJ, 499, 282

Kachelrieß, M., Ostapchenko, S., & Tomàs, R. 2008, Phys. Rev. D, 77, 023007

Kalapotharakos, C. & Contopoulos, I. 2009, A&A, 496, 495

Kalli, S., Lemoine, M., & Kotera, K. 2011a, ArXiv e-prints

Kalli, S., Lemoine, M., & Kotera, K. 2011b, A&A, 528, A109+

Kalmykov, N., Ostapchenko, S., & Pavlov, A. 1997, Nucl.Phys.Proc.Suppl., 52B, 17

Kamae, T., Karlsson, N., Mizuno, T., Abe, T., & Koi, T. 2006, ApJ, 647, 692

Kamae, T., Karlsson, N., Mizuno, T., Abe, T., & Koi, T. 2007, Astrophys. J., 662, 779

Kampert, K.-H. & Unger, M. 2012, Astropart.Phys., 35, 660

Kampert, K.-H. et al. 2004, Nuclear Physics B Proceedings Supplements, 136, 273

Karakula, S., Osborne, J. L., & Wdowczyk, J. 1974, Journal of Physics A Mathematical General, 7, 437

Kasen, D. & Bildsten, L. 2010, ApJ, 717, 245

Kasen, D. & Woosley, S. E. 2009, ApJ, 703, 2205

Kashti, T. & Waxman, E. 2008, Journal of Cosmology and Astro-Particle Physics, 5, 6

Katz, B., Blum, K., Morag, J., & Waxman, E. 2009, Mon. Not. R. Astron. Soc., 16

Katz, B., Budnik, R., & Waxman, E. 2009, Journal of Cosmology and Astro-Particle Physics, 3, 20

Katz, B., Sapir, N., & Waxman, E. 2011, ArXiv e-prints

Kennel, C. F. & Coroniti, F. V. 1984a, ApJ, 283, 694

Kennel, C. F. & Coroniti, F. V. 1984b, ApJ, 283, 694

Kennel, C. F. & Coroniti, F. V. 1984c, ApJ, 283, 710

Kifune, T., Hara, T., Hatano, Y., et al. 1986, J.Phys., G12, 129

Kirk, J. G. 2004, Physical Review Letters, 92, 181101

Kirk, J. G., Lyubarsky, Y., & Petri, J. 2009, in Astrophysics and Space Science Library, Vol. 357, Astrophysics and Space Science Library, ed. W. Becker, 421

Klages, H. & Pierre Auger Collaboration. 2012, Journal of Physics Conference Series, 375, 052006

Kniffen, D. A., Hartman, R. C., Thompson, D. J., Bignami, G. F., & Fichtel, C. E. 1974, Nature, 251, 397

Knurenko, S. & Sabourov, A. 2010

Knurenko, S. P. & Sabourov, A. 2011, Nucl.Phys.Proc.Suppl., 212-213, 241

Komissarov, S. & Lyubarsky, Y. 2004, Ap & SS, 293, 107

Kotera, K. 2011, Phys. Rev. D, 84, 023002

Kotera, K., Allard, D., & Lemoine, M. 2010a, ArXiv e-prints

Kotera, K., Allard, D., & Lemoine, M. 2011, A&A, 527, A54+

Kotera, K., Allard, D., Murase, K., et al. 2009, ApJ, 707, 370

Kotera, K., Allard, D., & Olinto, A. V. 2010b, J. Cos. and Astro. Phys., 10, 13

Kotera, K. & Lemoine, M. 2008a, Phys. Rev. D, 77, 023005

Kotera, K. & Lemoine, M. 2008b, Phys. Rev. D, 77, 123003

Kotera, K. & Olinto, A. V. 2011, Ann. Rev. Astron. Astrophys., 49, 119

Kotera, K. & Olinto, A. V. 2014, American Journal of Physics, 82

Kotera, K., Phinney, E. S., & Olinto, A. V. 2013, MNRAS, 432, 3228

Kouveliotou, C., Dieters, S., Strohmayer, T., et al. 1998, Nature, 393, 235

Kouveliotou, C., Strohmayer, T., Hurley, K., et al. 1999, ApJ Letters, 510, L115

Lagage, P. O. & Cesarsky, C. J. 1983, Astron. Astrophys., 125, 249

Large, M. I., Vaughan, A. E., & Mills, B. Y. 1968, Nature, 220, 340

Lee, S. 1998, Phys. Rev. D, 58, 043004

Lemoine, M. 2002, A&A, 390, L31

Lemoine, M. 2005, Phys. Rev. D, 71, 083007

Lemoine, M., Kotera, K., & Petri, J. in prep.

Lemoine, M. & Waxman, E. 2009, JCAP, 0911, 009

Letessier-Selvon, A. & Stanev, T. 2011, Rev. Mod. Phys., 83, 907

Li, Z. 2012, Phys. Rev. D, 85, 027301

Linden, T., Hooper, D., & Yusef-Zadeh, F. 2011, Astrophys. J., 741, 95

Linden, T. & Profumo, S. 2013, ApJ, 772, 18

Loeb, A. & Waxman, E. 2006, J. Cos. and Astro. Phys., 5, 3

Lorimer, D. R. 2004, Young Neutron Stars Their Environ.

Lorimer, D. R. 2008a, Living Rev. Relativ., 11

Lorimer, D. R. 2008b, Living Reviews in Relativity, 11

Lunardini, C., Razzaque, S., Theodoseau, K. T., & Yang, L. 2013, ArXiv e-prints

Lyne, A. G. & Graham-Smith, F. 2006, Pulsar Astronomy

Lyubarsky, Y. E. 2003, MNRAS, 345, 153

Madsen, J. 2000, Physical Review Letters, 85, 4687

Madsen, J. 2001, Physical Review Letters, 87, 172003

Madsen, J. 2005a, Journal of Physics G Nuclear Physics, 31, 833

Madsen, J. 2005b, Phys. Rev. D, 71, 014026

Madsen, J. 2006a, in 29th Johns Hopkins Workshop on Current Problems in Particle Theory: Strong Matter in the Heavens

Madsen, J. 2006b, ArXiv Astrophysics e-prints

Malkov, M. A. & O'C Drury, L. 2001, Reports on Progress in Physics, 64, 429

Manchester, R. N., Hobbs, G. B., Teoh, A., & Hobbs, M. 2005, Astron. J., 129, 1993

Mannheim, K., Protheroe, R. J., & Rachen, J. P. 2001, Phys. Rev. D, 63, 023003

Mao, S. A., McClure-Griffiths, N. M., Gaensler, B. M., et al. 2012, ArXiv e-prints

Martineau-Huynh, O. 2012, ArXiv e-prints: 1204.1599

Matzner, C. D. & McKee, C. F. 1999, ApJ, 510, 379

Maurin, D., Donato, F., Taillet, R., & Salati, P. 2001, Astrophys. J., 555, 19

McCray, R., Shull, J. M., & Sutherland, P. 1987, ApJ Letters, 317, L73

Meltzer, D. W. & Thorne, K. S. 1966, ApJ, 145, 514

Mereghetti, S. 2008, The Astronomy and Astrophysics Review, 15, 225

Metzger, B. D., Giannios, D., & Horiuchi, S. 2011a, MNRAS, 415, 2495

Metzger, B. D., Giannios, D., Thompson, T. A., Bucciantini, N., & Quataert, E. 2011b, MNRAS, 445

Michel, F. C. 1991, Theory of neutron star magnetospheres (Chicago, IL, University of Chicago Press, 1991, 533 p.)

Mori, K. & Hailey, C. J. 2003, Astrophys.J.

Mücke, A. et al. 1999, Publications of the Astronomical Society of Australia, 16, 160

Mücke, A. et al. 2000, Computer Physics Communications, 124, 290

Murase, K. & Beacom, J. F. 2010, Phys.Rev., D81, 123001

Murase, K. & Beacom, J. F. 2010, Phys. Rev. D, 81, 123001

Murase, K., Beacom, J. F., & Takami, H. 2012, JCAP, 8, 30

Murase, K., Dermer, C. D., Takami, H., & Migliori, G. 2011, ArXiv e-prints

Murase, K., Dermer, C. D., Takami, H., & Migliori, G. 2012, Astrophys.J., 749, 63

Murase, K., Inoue, S., & Nagataki, S. 2008a, ApJ Lett., 689, L105

Murase, K. & Ioka, K. 2008, ApJ, 676, 1123

Murase, K., Ioka, K., Nagataki, S., & Nakamura, T. 2006, ApJl, 651, L5

Murase, K., Ioka, K., Nagataki, S., & Nakamura, T. 2008b, Phys. Rev. D, 78, 023005

Murase, K., Mészáros, P., & Zhang, B. 2009, Phys. Rev. D, 79, 103001

Murase, K. & Takami, H. 2009, ApJ Letters, 690, L14

Murphy, D. C. & May, J. 1991, A&A, 247, 202

Narayanan, G., Heyer, M. H., Brunt, C., et al. 2008, ApJ Supplements, 177, 341

Neronov, A., Semikoz, D., & Tchernin, C. 2014, Phys. Rev. D, 89, 103002

Neronov, A. & Semikoz, D. V. 2009, Phys. Rev. D, 80, 123012

O'C. Drury, L. 2013, ArXiv e-prints: 1305.6752

O'C. Drury, L. & Aharonian, F. A. 2008, Astropart. Phys., 29, 420

Oechslin, R., Uryū, K., Poghosyan, G., & Thielemann, F. K. 2004, MNRAS, 349, 1469

Oikonomou, F., Connolly, A., Abdalla, F. B., et al. 2013, J. Cos. and Astro. Phys., 5, 15

Oikonomou, F., Kotera, K., & Abdalla, F. B. in prep., J. Cos. and Astro. Phys.

Oikonomou, F., Murase, K., & Kotera, K. 2014, accepted in A&A, ArXiv e-prints: 1406.6075

Oppenheimer, J. R. & Volkoff, G. M. 1939, Physical Review, 55, 374

Ostapchenko, S. 2008, Nucl.Phys.Proc.Suppl., 175-176, 73

Ostriker, J. P. & Gunn, J. E. 1969, ApJ, 157, 1395

Otsuka, M., Meixner, M., Panagia, N., et al. 2012, ApJ, 744, 26

Pacini, F. & Salvati, M. 1973, ApJ, 186, 249

Padovani, M., Galli, D., & Glassgold, A. E. 2009, A&A, 501, 619

Panei, J. A., Althaus, L. G., Chen, X., & Han, Z. 2007, MNRAS, 382, 779

Panov, A. D., Zatsepin, V. I., Sokolskaya, N. V., et al. 2011, Astrophysics and Space Sciences Transactions, 7, 119

Perez-Garcia, M. A., Daigne, F., & Silk, J. 2012, arXiv: 1211.7018

Perez-Garcia, M. A. & Silk, J. 2011, ArXiv e-prints

Perez-Garcia, M. A., Silk, J., & Stone, J. R. 2010, Physical Review Letters, 105, 141101

Pétri, J. & Lyubarsky, Y. 2007, A&A, 473, 683

Phinney, E. S., Evans, C. R., Blandford, R. D., & Kulkarni, S. R. 1988, Nature, 333, 832

Pierog, T. 2013, 10

Pierog, T. & Werner, K. 2008, Phys.Rev.Lett., 101, 171101

Pierre Auger Collaboration, Abreu, P., Aglietta, M., et al. 2012, ApJ Lett., 755, L4

Piran, T. 2004, Reviews of Modern Physics, 76, 1143

Pohl, M. & Eichler, D. 2012, ArXiv e-prints: 1208.5338

Protheroe, R. J. 1986, MNRAS, 221, 769

Protheroe, R. J. & Stanev, T. 1993, Month. Not. Roy. Astron. Soc., 264, 191

Pruet, J., Guiles, S., & Fuller, G. M. 2002, ApJ, 580, 368

Ptuskin, V., Zirakashvili, V., & Seo, E.-S. 2010, ApJ, 718, 31

Ptuskin, V. S., Jones, F. C., Seo, E. S., & Sina, R. 2006, Advances in Space Research, 37, 1909

Quimby, R. M. 2012, in IAU Symposium, Vol. 279, IAU Symposium, 22–28

Rachen, J. P. & Mészáros, P. 1998, Phys. Rev. D, 58, 123005

Rees, M. J. & Gunn, J. E. 1974, MNRAS, 167, 1

Regimbau, T. 2011, ArXiv e-prints

Regimbau, T. & Mandic, V. 2008, Classical and Quantum Gravity, 25, 184018

Rest, A., Foley, R. J., Gezari, S., et al. 2011, ApJ, 729, 88

Reynolds, M. T., Callanan, P. J., Fruchter, A. S., et al. 2007, MNRAS, 379, 1117

Reynolds, S. P. & Chevalier, R. A. 1984, ApJ, 278, 630

Reynolds, S. P., Gaensler, B. M., & Bocchino, F. 2012, Space Science Reviews, 166, 231

Rohrmann, R. D., Serenelli, A. M., Althaus, L. G., & Benvenuto, O. G. 2002, MNRAS, 335, 499

Rordorf, C., Grasso, D., & Dolag, K. 2004, Astroparticle Physics, 22, 167

Ruderman, M. A. & Sutherland, P. G. 1975, ApJ, 196, 51

Rybicki, G. B. & Lightman, A. P. 1985, Radiative processes in astrophysics.

Ryu, D., Kang, H., & Biermann, P. L. 1998, A&A, 335, 19

Salvati, M. & Sacco, B. 2008, Astron. Astrophys., 485, 527

Sanwal, D., Pavlov, G. G., Zavlin, V. E., & Teter, M. A. 2002, ApJL, 574, L61

Schure, K. M., Bell, A. R., O'C Drury, L., & Bykov, A. M. 2012, Space Science Reviews, 173, 491

Schuster, D. & Wiencke, L. 2012, in APS April Meeting Abstracts, 7007

Seckel, D. & Stanev, T. 2005, Physical Review Letters, 95, 141101

Shapiro, S. L. & Teukolsky, S. A. 1983, Black holes, white dwarfs, and neutron stars: The physics of compact objects (John Wiley and Son. Inc.)

Sigl, G., Miniati, F., & Enßlin, T. A. 2004, Phys. Rev. D, 70, 043007

Sironi, L. & Spitkovsky, A. 2009, ApJ Letters, 707, L92

Sironi, L. & Spitkovsky, A. 2011, ApJ, 741, 39

Spitkovsky, A. 2006, ApJ Letters, 648, L51

Spitkovsky, A. 2008, ApJ Lett., 682, L5

Srinivasan, G., Dwarakanath, K. S., & Bhattacharya, D. 1984, Journal of Astrophysics and Astronomy, 5, 403

Staelin, D. H. & Reifenstein, III, E. C. 1968, Science, 162, 1481

Stanev, T., de Marco, D., Malkan, M. A., & Stecker, F. W. 2006, Phys. Rev. D, 73, 043003

Stappers, B. W., Bessell, M. S., & Bailes, M. 1996, ApJ Letters, 473, L119+

Stappers, B. W., van Kerkwijk, M. H., Lane, B., & Kulkarni, S. R. 1999, ApJ Letters, 510, L45

Stecker, F. W. & Salamon, M. H. 1999, ApJ, 512, 521

Strong, A. W., Moskalenko, I. V., & Ptuskin, V. S. 2007, Ann. Rev. Nucl. Part. Sci., 57, 285

Sturrock, P. A. 1971, ApJ, 164, 529

Su, M., Slatyer, T. R., & Finkbeiner, D. P. 2010, ApJ, 724, 1044

Svirski, G., Nakar, E., & Sari, R. 2012, ApJ, 759, 108

Szabo, A. P. & Protheroe, R. J. 1994, Astroparticle Physics, 2, 375

Takami, H., Murase, K., & Dermer, C. D. 2013, Astrophys.J., 771, L32

Takami, H., Murase, K., Nagataki, S., & Sato, K. 2009, Astroparticle Physics, 31, 201

Takami, H. & Sato, K. 2008, ApJ, 681, 1279

Takeda, M. et al. 1998, Physical Review Letters, 81, 1163

Tamborra, I., Ando, S., & Murase, K. 2014, ArXiv: 1404.1189

Tameda, Y. et al. 2011, 32nd International Cosmic Ray Conference, Beijing, China, August 2011

Tanaka, S. J. & Takahara, F. 2011, ApJ, 741, 40

Tavani, M., Giuliani, A., Chen, A. W., et al. 2010, ApJ Lett., 710, L151

Tavecchio, F. 2014, MNRAS, 438, 3255

Taylor, A. M., Gabici, S., & Aharonian, F. 2014, Phys. Rev. D, 89, 103003

Taylor, A. M., Hinton, J. A., Blasi, P., & Ave, M. 2009, Phys. Rev. Lett., 103, 051102

Telescope Array, T., Pierre Auger Collaborations, :, et al. 2013, ArXiv e-prints

The Pierre Auger Collaboration, Aab, A., Abreu, P., et al. 2013, ArXiv e-prints: 1307.5059

The Pierre Auger Collaboration: J. Abraham, Abreu, P., Aglietta, M., et al. 2009, ArXiv e-prints: 0906.2354

Thompson, D. J. 1975, ApJ Lett., 201, L117

Thorstensen, J. R. & Armstrong, E. 2005, Astron.J., 130, 759

Turner, M. S. 1997, Phys. Rev. D, 55, 435

Usov, V. V. 1992, Nature, 357, 472

Utrobin, V. P. & Chugai, N. N. 2008, A&A, 491, 507

van den Bergh, S. & Tammann, G. A. 1991, Ann.Rev.Astron.Astrophys., 29, 363

van der Swaluw, E., Downes, T. P., & Keegan, R. 2004, A&A, 420, 937

van Kerkwijk, M. H., Breton, R. P., & Kulkarni, S. R. 2011, ApJ, 728, 95

Venkatesan, A., Miller, M. C., & Olinto, A. V. 1997, ApJ, 484, 323

Vernetto, S., Guglielmotto, Z., Zhang, J. L., & for the ARGO-YBJ Collaboration. 2009, ArXiv: 0907.4615

Wall, J. V., Jackson, C. A., Shaver, P. A., Hook, I. M., & Kellermann, K. I. 2005, A&A, 434, 133

Wang, X.-Y., Razzaque, S., & Mészáros, P. 2008, ApJ, 677, 432

Waxman, E. & Bahcall, J. 1999, Phys. Rev. D, 59, 023002

Waxman, E. & Bahcall, J. N. 2000, ApJ, 541, 707

Wdowczyk, J., Tkaczyk, W., & Wolfendale, A. W. 1972, J. Phys. A Math. Gen., 5, 1419

Weiler, K. W. & Panagia, N. 1980, A&A, 90, 269

Werner, K., Liu, F.-M., & Pierog, T. 2006, Physical Review C, 74, 044902

Wibig, T. & Wolfendale, A. W. 2004, ArXiv Astrophysics e-prints

Wilk, G. & Wlodarczyk, Z. 1996, Journal of Physics G Nuclear Physics, 22, L105

Witten, E. 1984, Phys. Rev. D, 30, 272

Wolfe, B., Melia, F., Crocker, R. M., & Volkas, R. R. 2008, ApJ, 687, 193

Woods, P. M. & Thompson, C. 2006, Soft gamma repeaters and anomalous X-ray pulsars: magnetar candidates (In: Compact stellar X-ray sources. Edited by Walter Lewin & Michiel van der Klis. Cambridge Astrophysics Series, No. 39. Cambridge, UK: Cambridge University Press, ISBN 978-0-521-82659-4), 547–586

Woosley, S. E., Heger, A., & Weaver, T. A. 2002, Reviews of Modern Physics, 74, 1015

Woosley, S. E. & Weaver, T. A. 1995, ApJ Supplements, 101, 181

Xu, Y., Sutherland, P., McCray, R., & Ross, R. R. 1988, ApJ, 327, 197

Yoshida, K., Torii, S., Yamagami, T., et al. 2008, Advances in Space Research, 42, 1670

Zatsepin, G. & Kuzmin, V. 1966, J. Exp. Theor. Phys. Lett., 4, 78

Zech, A. & Cerruti, M. 2013, in Contributions to ICRC 2013

Zhang, W., Woosley, S. E., & MacFadyen, A. I. 2003, ApJ, 586, 356